DYNAMIC PATTERN RECOGNITION AND DATA STORAGE USING LOCALIZED HOLOGRAPHIC RECORDING

A Dissertation
Presented to
The Academic Faculty

by

Arash Karbaschi

In Partial Fulfillment
of the Requirements for the Degree
Doctor of Philosophy in the
School of Electrical and Computer Engineering

Georgia Institute of Technology

August 2008

DYNAMIC PATTERN RECOGNITION AND DATA STORAGE USING LOCALIZED HOLOGRAPHIC RECORDING

Approved by:

Dr. Ali Adibi, Advisor
School of Electrical and Computer Engineering
Georgia Institute of Technology

Dr. Yucel Altunbasak
School of Electrical and Computer Engineering
Georgia Institute of Technology

Dr. William R Callen Jr
School of Electrical and Computer Engineering
Georgia Institute of Technology

Dr. Thomas K Gaylord
School of Electrical and Computer Engineering
Georgia Institute of Technology

Dr. Steven W McLaughlin
School of Electrical and Computer Engineering
Georgia Institute of Technology

Dr. Rick Trebino
School of Physics
Georgia Institute of Technology

Date Approved: April 25, 2008

In the loving memory of my grandmother,

to my dearest, Sara,

and to my parents

ACKNOWLEDGEMENTS

I would like to express my heartfelt gratitude to Prof. Ali Adibi, my PhD advisor, for providing me this opportunity to pursue my doctorate under his supervision. Knowing Prof. Adibi and working with him has been one of the most delightful and encouraging experiences in my life. I admire his commitment to excellence, his courage, his patience, and his high character. I hope our connection continues evermore.

My special thanks go to my research group members, who sincerely supported me during the course of my PhD. Dr. Omid Momtahan, my dear friend whom I have known since 1991, has been always there for me in all types of situations throughout my research and my life. I have constantly benefited from his wisdom and thoughtful advice, which I will remember forever, and forever be appreciative. We have had very productive research discussions, which have led to clever solutions to the research problems. I would like to name Dr. Chaoray Hsieh (Jerry) and Mr. Fengtao Wang as my close colleagues and collaborators. I have gained much from their vast experience in optics experiments, which they have generously shared with me. I am thankful to Mr. Ali Asghar Eftekhar (Reza) and Dr. Babak Momeni for the fruitful research conversations, which always led to more clear thinking and creativity. I wish to thank all of the members of the Photonics Research Group, with whom I have experienced a pleasant and progressive work environment. I am also grateful to Dr. Shayan G. Srinivasa and Miss Jiaxi Xiao from Prof. McLaughlin's research group for the rewarding collaborations.

I would like to acknowledge my other friends, above all Dr. Reza Abdolvand and Dr. Nazanin Rahnavard, a lovable couple, and Ali Mansouri (Mehrshad). Living with

Reza as my roommate has been an exceptional gift and a turning point in my life, which I will appreciate forever. With Mehrshad, we had so much fun during our education in Sharif University and after that during our partnership, for which I am grateful. I am also thankful to the great Iranian community of Atlanta for all their friendship, kindness, and support.

I feel indebted to my school teachers, who stimulated my interest in science. In particular, I would like to name Mr. Shiri, my science teacher in middle school, and Mr. Takhtkouseh, my physics teacher in high school. I am thankful for their great motivational effort on my behalf.

I wish to commemorate Mr. Iraj Kassaian of blessed memories, the former CEO of Darakar Inc., the company for which I formerly worked. Mr. Kasssian was my mentor and always supported me and my activities. I have learned from him everything I know about professional conduct and business ethics.

I would like to thank my parents, to whom I owe the most, for their love and support throughout my life. My mother, Mrs. Mahin Havaei, took the best care for my education, as she is a great teacher herself. My father, Mr. Hassan Karbaschi, has been always a knowledgeable guide and a considerate help for me.

Finally, I dedicate my warmest thanks to my wife, Mrs. Sara Saatchi. Our marriage occurred in the middle of my PhD, and I believe that has been by far my best achievement during my PhD and even my entire life. She brings so much love and passion to our life and has been a patient and thoughtful advisor and a supportive friend.

TABLE OF CONTENTS

LIST OF TABLES

LIST OF FIGURES

LIST OF ABBREVIATIONS

APSF	Amplitude Point Spread Function
AR	Anti Reflection
ATF	Amplitude Transfer Function
BER	Bit Error Rate
CW	Continuous Wave
EM	Electromagnetic
FT	Fourier Transform
FWHM	Full Width at Half Maximum
HEPA	High Efficiency Particulate Air
LCD	Liquid Crystal Display
LH	Localized Holographic
LHC	Localized Holographic Correlator
LHM	Localized Holographic Memory
NA	Numerical Aperture
NSR	Noise to Signal Ratio
SLM	Spatial Light Modulator
SNR	Signal to Noise Ratio
WORM	Write Once Read Many

SUMMARY

In this research, a new technique for optical pattern recognition with two-center recording of persistent holograms in doubly doped $LiNbO_3$:Fe:Mn crystal is presented, by which the holograms are localized in separate slices along the recording medium. The localized recording method has the distinctive advantage of selective recording and erasure of the individual holograms without affecting the entire holographic recording medium. This capability enables dynamic content modification of the optical pattern recognition systems. Also, the diffraction efficiency of localized holograms is much larger than that of the normal volume multiplexed holograms. It is theoretically shown that the localized holographic correlator (LHC) outperforms the conventional volume holographic correlators in terms of crosstalk, shift invariance, and capacity. The LHC is experimentally demonstrated. Several persistent holograms are localized within separate slices as close as 33 μm apart along the crystal. The excessive diffraction efficiency of the localized holograms is employed to enhance the LHC robustness through multiplexing several holograms per pattern within individual slices of the recording medium.

A holographic data storage system based on two-center holographic recording in a doubly doped $LiNbO_3$:Fe:Mn crystal is developed with angular multiplexing capability. The associated imaging system has been optimized for the pixel matching of pixelated bit patterns generated by a spatial light modulator (SLM) through the recording medium onto a camera. The utilized bit patterns have the largest resolution and finest pixel size among the holographic memories with two-center recording. The initial multiplexed holograms

show promising contrast of dark and bright pixels. With the optimized imaging system of the developed holographic memory, the implementation of a dynamic read/write data storage system with localized recording is envisioned. The large diffraction efficiency of the localized holograms enables multilevel (M-ary) data coding to improve the storage density of the system.

CHAPTER 1

INTRODUCTION

1.1 Brief History and Motivation

In 1948, Gabor demonstrated recording of the interference pattern of a diffracted wavefront with a coherent background [1], and named the process, holography. He theoretically and experimentally showed the ability of the recorded interference pattern, called hologram, to reconstruct the diffracted wavefront with only the coherent background illuminating it. He deduced that the data of a 3D object could be stored in one hologram by this method. After the invention of the laser in early 1960s, the two coherent recording beams did not have to be in-line and having desired angles between them was made possible. The two interfering beams were named signal and reference beams corresponding to the beam carrying the information of the recorded image or 3D object and the other plain beam with which the hologram was recorded and later read, respectively.

It was van Heerden who developed the concept of information storage by volume holography in 1963 [2]. He studied the phase mismatch effect caused by reading the thick holograms with mismatch reference beams. He then discussed the capability of the thick holographic media for recording multiple holograms in them using both the angle and the wavelength multiplexing. In the angle multiplexing method as shown in Figure 1(a), after recording each hologram the reference beam is rotated for some angle until the complete reading phase mismatch occurs meaning the rotated reference no longer reads the previously recorded hologram(s). With the new angle of the reference beam, another

hologram can be recorded. The result is each recorded hologram has a specific corresponding reference angle, meaning if the reference beam is illuminated at that angle to the recording medium, it only reads the corresponding hologram with reasonably low crosstalk from other multiplexed holograms. In other words, the reference angle acts as an addressing tool for retrieving the data of each multiplexed hologram. The same concept is utilized for the wavelength multiplexing except that instead of the angle of the reference beam, the wavelength of the two recording beams is changed for each multiplexed hologram [Figure 1(b)]. Therefore, the corresponding wavelengths will be the addresses of the multiplexed holograms.

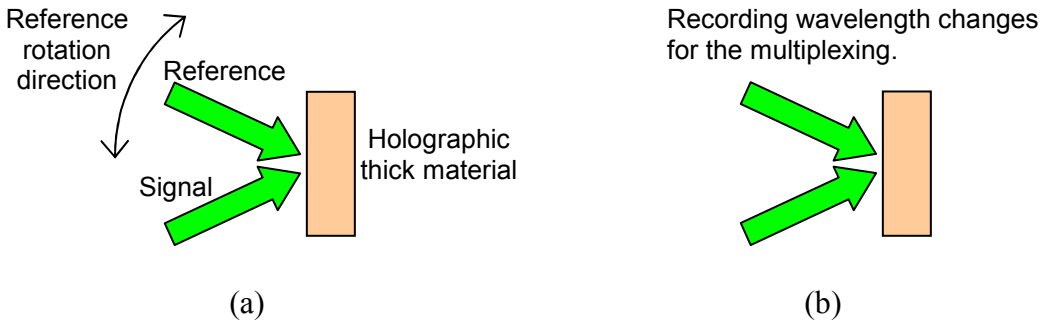

Figure 1. Two basic multiplexing methods: (a) Angle multiplexing. (b) Wavelength multiplexing.

By the introduction of the multiplexing concept, the holographic data storage was sought to be a practical solution and a highly competitive alternative versus magnetic recording for data storage applications. The holographic data storage was elaborately researched and many types of system configurations and multiplexing methods were implemented in the laboratories. However, most of the key elements of a realistic holographic memory system were not available yet in the 60s and 70s. The high

resolution, fast spatial light modulators (SLMs) and sensor arrays (CCD and CMOS cameras) were not invented. The SLM, acting as a dynamic mask, modulates one of the recording beams (signal) with a 2D page of bits. More importantly, recording materials with acceptable sensitivity, dynamic range, persistence, and fidelity of recording were not developed. These shortages kept the holographic storage systems in the scientific laboratories until mid 1990s [3]. At that time, higher quality SLMs and sensor arrays were emerging and more reliable inorganic and organic recording materials with much better recording performances were being developed and holographic memory received more serious attention both in academia and industry [4].

Among the holographic materials of interest, the inorganic photorefractive crystals (e.g., $LiNbO_3$ crystals doped with iron) have attracted many researchers and system developers because of very low scattering, high recording fidelity, and the ability to erase and re-record holograms in them [5]. On the other hand, the organic holographic materials including photopolymers have been desirable for their high sensitivity, high dynamic range, durability of the holograms, and low cost [6,7]. Inphase Technologies, Inc. is a company that has developed a holographic data storage system based on holographic recording in photopolymers [8]. Their recording medium is of Write Once Read Many (WORM) format.

1.2 Holographic Correlators

During the recess in the development of holographic memories in the 60s and 70s, the new concept of optical signal processing was developed based on the findings in holography. Optical signal processing and pattern recognition have been appreciated since the complex spatial filtering work by VanderLugt in 1964 [9] and demonstration of

the joint transform correlator by Weaver and Goodman in 1966 [10]. These methods of optical correlation in fact were invented to provide a tool for two-dimensional spatial filtering. The correlation functionality is obtained by reading a hologram with the signal beam and retrieving the reference beam rather than reading it with the reference beam and retrieving the signal beam as in the data storage application. During the readout, if the signal beam matches the signal beam with which the hologram has been recorded, the reference beam is reconstructed and diffracted from the hologram, indicating the matching of the two signals.

In both VanderLugt's filter and Goodman's joint correlator, only one stored pattern was correlated with the incoming patterns. The advantage of multiplexing several patterns in a volume hologram [2] made optical correlation a significant method to be utilized in optical pattern recognition. In this way the incoming pattern is correlated with all of the stored patterns each recorded as a volume hologram. As a result, holographic information processors have massive parallelism and high speed [3]. The applications of the optical correlators have been extended to 3D object recognition as well [11,12].

Much research has been performed in volume holographic correlation, extending its outstanding capabilities to a variety of applications. Some examples are the implementation of optical neural networks [13], real-time vehicle navigation [14], content-addressable data storage [15] and fingerprint recognition [16]. In all these applications, the optical correlation is performed using multiplexed volume holograms, and all of the stored holograms in the system use the entire volume of the recording medium. Since all the stored patterns (or holograms) overlap in the same volume of the recording medium, the multiplexing is performed once all of the patterns are available.

Adding extra patterns to or erasing select patterns from the system after the recording phase is complicated because all of the stored patterns in the recording medium are affected by the optical beams required for recording or erasing some holograms. Thus, the conventional techniques can not be used for dynamic pattern recording and erasure.

The multiplexed holograms share the same volume of the recording medium. Therefore, recording of each hologram results in partial erasure of the previously recorded holograms. This erasure greatly limits the capacity of the holographic storage systems because each hologram has to have a minimum of diffraction efficiency to maintain the acceptable performance of the correlator. In the best case scenario, when the holograms have the same eventual diffraction efficiency, the diffraction efficiency of each hologram degrades inversely proportional to the square of the number of holograms ($\eta \propto 1/M^2$; η: diffraction efficiency, M: number of multiplexed holograms) [13]. Moreover, the entire volume of the recording medium is sensitive to the recording light beams while recording, which implies that the recording photons are absorbed as they penetrate the recording medium and the beams are attenuated. Thus, there exists an optimum effective thickness for the recording medium, beyond which the capacity of the system decreases, despite the expectation that the capacity should increase as the recording medium becomes thicker [3].

1.3 Photorefractive Process in $LiNbO_3$:Fe

The recording mechanism involved with doped $LiNbO_3$ crystals is the photorefractive process [17,18], which accounts for the refractive index variations induced by a light pattern. When the light pattern of the interference between the reference and signal beams (which is a 3D fringe pattern) is formed within the volume of the crystal, the

photorefractive process conducts the migration of the electrons as the charge carriers, according to the light pattern. Build-up of the local gradients of charge concentration produces a 3D distribution of electric field over the crystal volume. The local electric fields in turn form a pattern of refractive index variation through the electro-optic effect dominated by the linear electro-optic effect (Pockels effect) [19,20]. This index variation pattern is the intended volume phase grating recorded inside the crystal.

In doped $LiNbO_3$ crystals, the migration of the electrons is initiated by exciting them from the impurity ion valence states (defect traps) with energy levels within the crystal energy bandgap, to the conduction band. Figure 4 illustrates the band diagram of the singly doped $LiNbO_3$:Fe crystal showing how the electrons are excited and captured. Iron has been the most generally used dopant for $LiNbO_3$ primarily because of the better recording sensitivity of $LiNbO_3$:Fe [21]. The excitation occurs when the incident photons with adequate energy are absorbed by the electrons in the filled impurity centers (Fe^{+2} centers), hence creating an excess of electron concentration in the conduction band in the bright regions of the recording interference pattern. While in the conduction band, the electrons are mostly influenced by the photovoltaic effect and tend to move preferably in the direction of the optical axis of the crystal [17]. Because of the limited lifetime of the electrons in the conduction band [22], they are captured at the empty centers (Fe^{+3} centers) after traveling a short distance in the conduction band. The captured electrons are hit by the incident photons and are excited to the conduction band over again until they reach the dark regions of the light interference pattern and are captured at the empty centers there. The space charge pattern is eventually built up as the migration of the

electrons reaches equilibrium due to the increase of the electric field that is against the movement of the electrons.

The readout of holograms is normally carried out with one of the signal or reference beams, depending on the application, with the exact same wavelength to obtain a perfect Bragg matching. Therefore, the electrons in the iron centers creating the space charge pattern can absorb the photons in the reading beam as they did during the recording. Because the illumination of one beam is rather uniform than spatially oscillatory in case of the interference of two beams, the excited electrons will be uniformly redistributed over time. As a result, the recorded holograms being read frequently are completely erased. The erasure issue is the main limitation of the singly doped $LiNbO_3$ for being used in the holographic data storage systems and optical

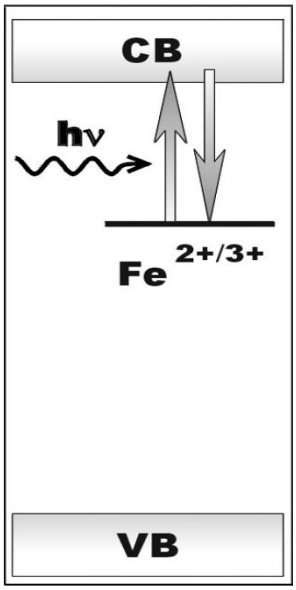

Figure 2. Energy band diagram of singly doped $LiNbO_3$:Fe. Electrons are excited into the conduction band from electron filled Fe^{2+} levels by the recording beams. Conduction band electrons recombine with Fe^{3+}. CB and VB stand for conduction band and valence band, respectively (Figure courtesy of K. Buse, *et al*., Nature, v. 393, p. 665, 1998).

correlators. In the following section, gated holography methods used to resolve this problem are discussed.

1.4 Gated Holography in $LiNbO_3$

Gated holography is an all optical technique for recording persistent holograms in photorefractive crystals [23]. In this method, two sets of defect traps having different energy levels are involved in the photorefractive process. The idea is based on forming the space charge pattern with the electrons in the shallower traps that can be excited by the recording beams and eventually storing the space chare pattern in the deeper traps. The photon energy of the recording beams is not sufficient to excite the electrons from the deeper traps, hence persistence of the imprinted space-charge pattern in the deeper traps against further readout. However, usually at the beginning of the recording, the shallower traps are empty of electrons, while the deeper traps are partially filled. A third beam, called the gate or sensitizing beam, populates the shallower traps with the electrons from the deeper traps. In other words, the gate beam sensitizes the illuminated area for the recording. The gate beam has higher photon energy than the recording beams, which suffices the excitation of the electrons in the deeper traps. The electrons are then transferred to the shallower traps directly or indirectly through the conduction band, depending on the nature of the point defects and their concentrations. One can deduce that recording and erasure of the stored space charge pattern in the deeper traps occurs effectively in the presence of the gate beam (i.e., in the sensitized regions). Two-step and two-center recording methods are the two gated holography techniques in photorefractive crystals, which are explained in the following subsections.

1.4.1 Two-Step Recording

In two-step recording, the polarons and bipolarons produced by the intrinsic point defects of the $LiNbO_3$ are used as the shallow and deep traps, respectively [23,24]. Figure 3 shows the possible electron transitions in the two-step recording process. The direct and indirect transitions of the electrons from deep to shallow states (transitions 1 and 2 in Figure 3, respectively) occur by the sensitizing beam. The electrons in the polaron states can be thermally excited to the conduction band (transition 5) even at the room temperature [25], resulting in depopulation of the shallow traps in dark. The forward and backward direct transitions (transitions 1 and 6 in Figure 3, respectively) only take place in high concentrations of the point defects in the congruent crystals [23]. The backward

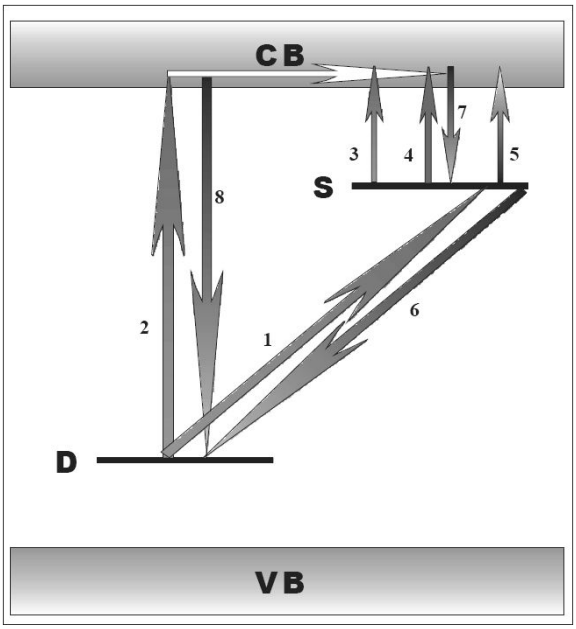

Figure 3. Energy band diagram and possible electron transitions for two-step gated holographic recording. Transitions 1, 2, and 3 are initiated by the sensitizing beam, and transition 4 by the recording beams. Transition 5 is driven by thermal excitation, and all other transitions occur in dark. VB, CB, D, and S stand for valence band, conduction band, deep trap (bipolaron), and shallow trap (polaron), respectively.

direct transition, also occurring in dark, depopulates the shallow traps as well. The undesired depopulation transitions necessitate a high intensity sensitizing beam to maintain the electron population in the shallow traps.

The issue of backward direction transition is addressed by using near-stoichiometric crystals with much smaller defect concentrations [26]. Nonetheless, the dark depopulation by thermal excitation still exists that makes the two-step process less sensitive. Also, the small concentration of the defects greatly lowers the maximum diffraction efficiency of the holograms. Finally, the intrinsic parameters of the crystal cannot be optimized in practice for the best recording performance.

1.4.2 Two-Center Recording

The gated holography technique used in this research is two-center recording. The desired shallow and deep traps in two-center recording are created by doping the photorefractive crystal with two different ions that produce two completely distinct valence states within the energy bandgap of the crystal. The first demonstration of efficient two-center recording was performed with a $LiNbO_3$ crystal doped with iron and manganese [27]. The very first experiments resulted in superior performance over the two-step recording in a variety of aspects such as sensitivity, diffraction efficiency, and dark storage time.

Figure 4 shows the energy band diagram of the doubly doped $LiNbO_3$:Fe:Mn crystal. In an optimally oxidized crystal, the Mn traps are about 90% full and the Fe traps are completely empty at the beginning of the recording [28]. The electrons are excited from Mn traps to the conduction band using near UV illumination with a wavelength of about 405 nm or shorter. This UV beam is referred to as the gate beam or the sensitizing

beam. A portion of the excited electrons are recombined with the empty Fe traps, hence providing electrons for the recording in the shallow traps. The two coherent beams at larger wavelengths (green 532 nm, red 633 nm or other available laser lines in or about this wavelength range) are used to record the holograms. The recording beams can excite electrons from the shallower traps only. The space charge pattern builds up in both Fe and Mn traps. The UV beam continuously illuminates the recording area to maintain the electron population in the Fe traps until the desired hologram strength is obtained. Then the UV beam is turned off and the hologram is illuminated by a uniform beam with the same photon energy as the recording beams. This erases the space charge pattern in the

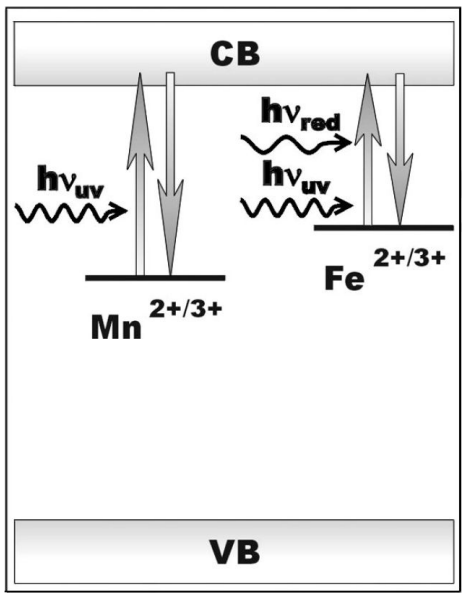

Figure 4. Energy band diagram of doubly doped $LiNbO_3$:Fe:Mn. Both Fe and Mn impurity states occur in two different energy levels. Electrons are excited into the conduction band from electron filled Fe^{+2} levels either by recording beams or by the sensitizing beam, or from Mn^{2+} by the sensitizing beam only. Conduction band electrons can recombine with Fe^{3+} or with Mn^{3+}. CB and VB stand for conduction band and valence band, respectively (Figure courtesy of K. Buse, *et al*., Nature, v. 393, p. 665, 1998).

Fe traps and the eventual imprinted space charge pattern in the Mn traps will be persistent against further readout, since the reading beam cannot excite electrons from the Mn traps.

Impurity ions such as iron and manganese are advantageous over the intrinsic defects of the crystal (e.g., in two-step recording) in a variety of aspects for creating the shallow and deep traps [23]. The energy level of the iron traps is deeper than that of the polarons in the crystal energy bandgap, eliminating the thermal excitation of the electrons in the shallow traps at the room temperature. As a result, the shallow traps are not depopulated in dark, which increases the recording sensitivity. Moreover, the concentrations of the dopants can be arbitrarily selected over a wide range. This introduces a great opportunity to optimize the recording performance of doubly doped crystals. The dopant concentrations can be small yet yielding decent diffraction efficiency. Because of the low concentrations of the defect levels, the direct transitions which are present in two-step recording in congruent crystals (transitions 1 and 6 in Figure 3), are negligible in two-center recording. Also, the backward direct transition (transition 6 in Figure 3) that greatly limits the recording sensitivity in two-step recording is insignificant. In addition, the smaller electron mobility in the conduction band in two-center recording improves the dark storage time [23].

Much research has been carried out on doubly doped $LiNbO_3$:Fe:Mn crystal to optimize the crystal parameters such as the dopant concentrations and oxidation/reduction state together with the recording parameters such as the recording and sensitizing intensities and intensity ratios [29,30]. O. Momtahan *et al.* optimized the recording and crystal parameters of $LiNbO_3$:Fe:Mn simultaneously for the highest diffraction efficiency together with the highest recording sensitivity. With the optimized crystal they grew, they

could show significant improvements compared to the results obtained with the first doubly doped crystal in terms of recording sensitivity and ultimate diffraction efficiency [31]. The crystal used in most of the experiments of this research is cut from the same crystal boule grown for the optimization experiments. Other dopants also have been investigated for creating the shallow and deep traps and have shown promising recording characteristics and persistence [32,33].

1.5 Localized Holographic Recording

In this research, the unique features of localized holographic (LH) recording [34] have been utilized to develop a new class of dynamically controlled systems for 2D pattern recognition. Also, the potentials of LH recording for 3D object recognition and data storage with full functionality (read, write, and selective erase/rewrite) have been investigated. Localized recording is a direct application of the gated holographic recording, in which the holograms are recorded in separate thin slices along the recording medium. Figure 5 schematically illustrates the LH recording configuration. The sensitizing UV beam, shaped as a thin film of light, sensitizes the slices of the crystal within which the holograms are recorded. In other words, the recording slices are defined by the gate beam. The reference beam copropagates with the UV beam through the defined slices and interferes with the signal beam, which is propagating throughout the length of the crystal. The interference pattern is recorded within the defined slice of the crystal, hence creating a localized hologram.

By use of LH recording, the holograms do not overlap in the volume of the recording medium. The separate slices, within which the holograms are recorded, are individually accessible by the reference and the gate beams. Therefore, every hologram

within a slice can be independently recorded, erased, and re-recorded with no significant effect on the other holograms recorded in the other slices. This enables the dynamic recording and erasing of the holograms. Whereas in the conventional volume holography methods, all of the recorded holograms have to be recorded and erased together and there is no selective access to every desired hologram for erasing and re-recording.

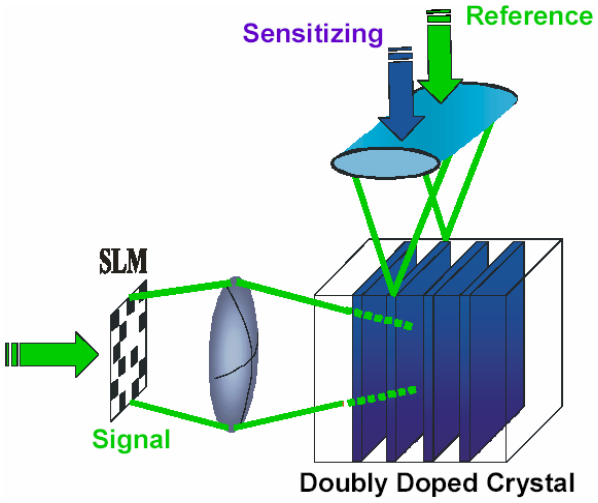

Figure 5. Schematic illustration of LH recording configuration. The sensitizing UV beam, shaped as a thin film of light, sensitizes the slices of the crystal within which the holograms are recorded. The reference beam copropagates with the UV beam through the defined slices and interferes with the signal beam, which is propagating throughout the length of the crystal. The interference pattern is recorded within the defined slice of the crystal.

Because the holograms are recorded in separate localized slices along the recording medium, recording each hologram does not affect the other recorded holograms. As a result, the partial erasure present in the volume multiplexing methods that degrades the diffraction efficiencies of the holograms is not of concern in localized recording. It is shown that the diffraction efficiency of the holograms in localized recording is inversely proportional to the number of the recorded holograms ($\eta \propto 1/M$)

[35] rather than to the square of that number as in volume holography ($\eta \propto 1/M^2$). Therefore, the diffraction efficiency of each hologram can be much larger and is no longer a limiting factor for the capacity. The capacity (i.e., the number of stored holograms) is rather determined by how thin the slices can be formed and the length of the crystal. The excess of the diffraction efficiency per each slice can be utilized to further multiplex more than one hologram within each slice [36]. In the optical correlators, this is valuable to record different versions of each pattern or object (e.g., shifted or rotated versions) in the corresponding slice and therefore, enhances the robustness of the recognition versus shift or rotation of the examined pattern or object.

The recording medium is sensitized only at individual thin slices along the medium and therefore, is not sensitive at all other locations of it. This implies that the recording photons are only absorbed at the sensitized slices and the recording beams are not attenuated as they travel along the crystal. As a result, the length of the crystal can be arbitrarily selected with no concern about the beams losing energy and that way the capacity of the system can be increased by choosing longer crystals.

1.6 Thesis Outline

In Chapters 2-4, the localized holographic correlator (LHC) for recognition of 2D patterns is demonstrated. A general analysis method is developed and introduced for LHC that is the basis of the theoretical study of the pattern recognition in such systems. The performances of the LHCs and the conventional correlators using normal volume holography (angular multiplexing) are compared by simulation and the results are presented in Chapter 2. Crosstalk, shift-invariance, and capacity of the LHC and those of the conventional method are examined as the performance measures of the optical

correlation system. It is shown that the LHC has better performance and distinctive advantages over the conventional method. These advantages include selective recording and erasure for dynamic content modification, extendable capacity, and compactness.

Theoretical results for the performance measures are verified by experimental data, which are presented in Chapter 3. For this purpose a complete recording and measurement correlator setup is designed and implemented based on localized recording. Several persistent holograms are recorded in localized slices 33 μm apart from each other. To the best of the author's knowledge, the 33 μm distance between the adjacent slices is the smallest reported to date for localized holography. The crosstalk from the other holograms recorded in the medium at the place of a blank slice is -20 dB. The dynamic recording and erasure capability of the system is shown by recording and erasing select holograms without affecting other holograms recorded inside the crystal. The objects under study at this stage are 2D random pixelated patterns made by individual masks.

The robustness of the LHC for 2D patterns is enhanced in terms of shift invariance and rotation invariance and the results are presented in Chapter 4. All the optical correlators are most selective for the shift of the examined pattern in the plane of the reference and signal beams (i.e., in-plane shift). This is true for the LHC as well. The excess of the diffraction efficiency of the localized holograms, as will be shown in Chapter 2, enables multiplexing several holograms within the volume of each slice. To increase the range of the shift invariance, 20 holograms per one pattern have been multiplexed in the corresponding slice of that pattern, using the excess of the diffraction efficiency of each slice [36]. The holograms have been originated from 20 shifted

versions of the pattern. The shift invariance has been improved by a factor of 9. This process has been repeated for the rotation invariance expansion and an 8 times rotation invariance improvement has been achieved by multiplexing 12 holograms within one slice of the recording medium. A suitable recording schedule has been employed to attain the same strength of all of the multiplexed holograms. In the end of Chapter 4, the extension of the LHC to recognize 3D objects is discussed. The motivation for 3D object recognition by holography comes from the fact that a hologram records and reproduces both the amplitude and the phase of a wavefront. Thus, it is possible to distinguish between two objects with their features located at different depths, although their 2D perspectives may look alike when viewed at certain angles. Moreover, using the same method for the robustness enhancement of the LHC for 2D patterns, it is feasible to improve the robustness of the 3D LHC as well by multiplexing the holograms originated from different aspects of the 3D objects. The potentials of the LHC for the 3D object recognition and the existing limitations and trade-offs are discussed.

In Chapter 5, a holographic data storage system with two-center recording in doubly doped $LiNbO_3$:Fe:Mn crystal is presented. The angular multiplexing in 90-degree geometry has been used for hologram multiplexing. The recorded data pages have the finest pixel size (28 μm) and the largest resolution (512 × 384) among the developed holographic data storage systems based on two-center recording, to the best of the author's knowledge. The pixel matched image of the SLM at the camera is obtained through a 4-f imaging system with the crystal present. A new normalization method has been developed with which the bit pattern images are significantly enhanced with the elimination of the fringes and speckles involved with coherent imaging. A simple yet

accurate pixel matching method has been utilized, whereby the imperfections of the imaging system have been alleviated. The histogram of the pixel matched bit pattern image shows very small overlap of the dark and bright intensity distributions. The estimated SNR of the imaging is 7.4, which is the largest reported for a holographic data storage system based on two-center recording. 10 holograms have been multiplexed using the developed holographic data storage system. The retrieved bit pattern images from the multiplexed holograms show promising contrast. The adoption of the localized recording technique to develop a dynamic read/write holographic data storage module has been investigated with the optimized imaging configuration of the developed storage system. The feasibility of the storage density improvement with multilevel (M-ary) data coding in localized holographic data storage has been discussed, which is enabled by the large diffraction efficiency of the localized holograms.

In Chapter 6, a summary of the research is presented and the achievements and main contributions are briefly explained. Furthermore, the future directions of this research have been outlined as a number of tasks to improve the results of this research along with some suggestions for the realization of practical products based on the findings of this research.

CHAPTER 2
LOCALIZED HOLOGRAPHIC CORRELATORS

2.1 Introduction

In this Chapter, the localized holographic correlators (LHCs) are introduced and the results of the theoretical analyses and simulations are presented. An LHC uses the localized holographic recording technique [34], enabled by gated holographic recording in photorefractive crystals [23]. Using this method, every pattern in the system can be recorded and erased at any arbitrary time without affecting other holograms, making LHCs excellent candidates for the implementation of dynamic optical correlators. By simulation, it is shown that the performance of the LHC measured by crosstalk, shift invariance, and capacity is better than that of the conventional angle-multiplexed optical correlators. Moreover, the capacity of the LHC is extendable by using longer recording medium**,** and the complete correlation system is more compact than a conventional volume holographic correlator.

2.2 Basic Idea of LHCs

The basic idea for an LHC [36] is shown in Figure 1. Figure 1(a) shows the general recording setup for localized holographic recording in 90-degree geometry [37]. Each hologram is recorded by the simultaneous overlap of a sensitizing (or gating) beam and two coherent recording beams (i.e., reference beam and signal beam) in a thin slice of the recording medium. It should be noted that different holograms are recorded in different slices and will not overlap with each other. In the recognition phase, the signal beam

corresponding to the unknown pattern is correlated with all the stored patterns, as depicted in Figure 1(b). The unknown pattern will read all the holograms, resulting in diffraction of their corresponding reference beams, if Bragg matching occurs (i.e., if any of the holograms are read with an optical beam with the same spatial profile used for their recording). The diffracted signals are detected by a detector array adjacent to the recording medium as shown in Figure 1(b). If the reading pattern is similar to one of the recorded patterns, a strong diffracted signal is obtained at the detector corresponding to that pattern. Otherwise, all detected signals are weak confirming negligible correlation between the reading pattern and all recorded patterns.

As mentioned in Section 1.4 in Chapter 1, the implementation of localized holographic recording is made possible by advances in gated holography techniques:

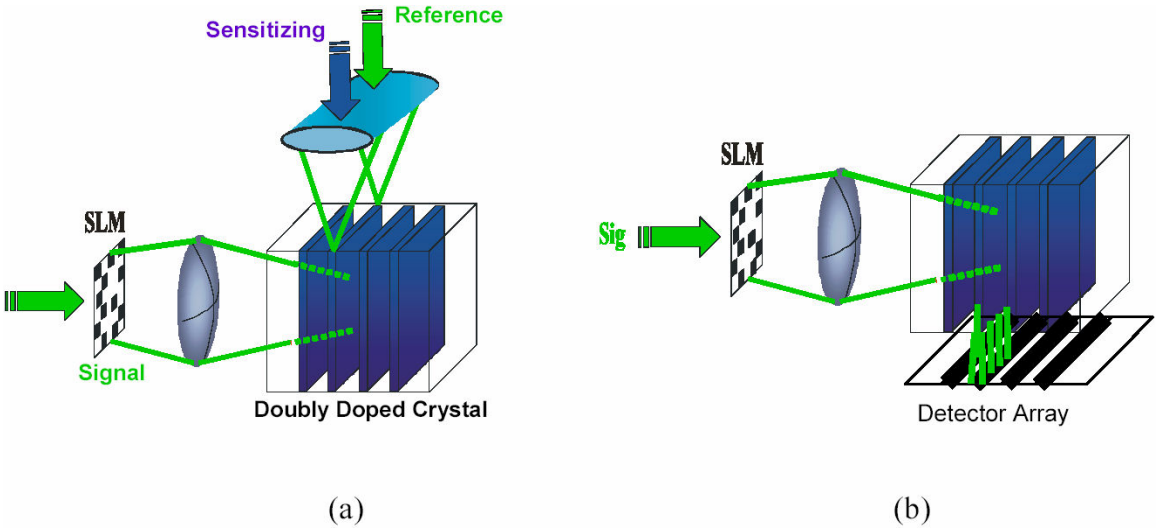

Figure 6. Localized holographic correlation steps: (a) recording (b) correlating. During recording, each pattern is recorded as a volume hologram in a thin slice of the recording medium that is sensitized by the sensitizing beam. Reading of a hologram by its corresponding reading beam (or pattern) results in a strong diffracted beam from a thin slice of the recording medium.

two-step recording [24] and two-center recording [27]. The latter method, however, has major advantages in a variety of aspects such as sensitivity, dynamic range, and dark storage time [23,29]. By using gated holography, the recording and erasure of the holograms is only possible in the presence of a third sensitizing beam, which acts as a gate. The regions of the recording medium illuminated by the sensitizing (or gating) beam get sensitized so that the two recording beams can record a hologram in those regions. Therefore, by shaping the sensitizing beam to form a thin slice within the recording medium [as shown in Figure 6(a)], the hologram is localized within the volume of that slice.

Since the recording beams affect only the sensitized slice, recording at one slice does not erase the holograms previously stored at other slices. As a result, individual patterns can be dynamically inserted into and/or removed from the optical pattern recognition system without affecting the already recorded patterns. Moreover, reading the holograms with the signal beams, in the absence of the sensitizing beam, does not erase the recorded holograms as it does in the conventional (not-gated) holography. This gives persistence to the recorded patterns (unless they are erased deliberately by light at sensitizing wavelength) and prevents the reading beam from getting absorbed by the crystal. As a result, the absorption of the reading beam by the holographic medium is negligible and the recording medium can be made long enough to include all the desired patterns.

2.3 Theoretical Analysis of LHCs

In Figure 7, the correlation system is illustrated with more details that are used in the analysis. The recording and reading patterns are applied to an SLM, which is put in the

front focal plane of a lens with focal length F. The SLM is illuminated by a monochromatic plane wave light source at recording wavelength λ. The electromagnetic (EM) field pattern at (u,v,z) within the recording slice, represented by $F_1(u,v,z)$, caused by the recording pattern $f_1(\xi_1,\eta_1)$ at the SLM can be calculated using Fresnel diffraction approximation (refer to Appendix A) as

$$F_1(u,v,z) \propto \iint_{SLM} f_1(\xi_1,\eta_1)\exp\left[-j\frac{\pi z}{n\lambda F^2}\left(\xi_1^2+\eta_1^2\right)\right]\exp\left(j\frac{2\pi nz}{\lambda}\right)\exp\left[-j\frac{2\pi}{\lambda F}\left(u\xi_1+v\eta_1\right)\right]d\xi_1\,d\eta_1 \quad (1)$$

Here, $F_1(u,v,z)$ can represent electric or magnetic field depending on the polarization of the signal beam. All parameters in Equation (1) are defined in the captions of Figure 7. The reference beam within the sensitized slice of the recording medium can be approximately represented as a plane wave, i.e., $\exp(jk_u u)$ where $k_u = 2n\pi/\lambda$ with n being the refractive index of the recording material. Therefore the permittivity modulation due

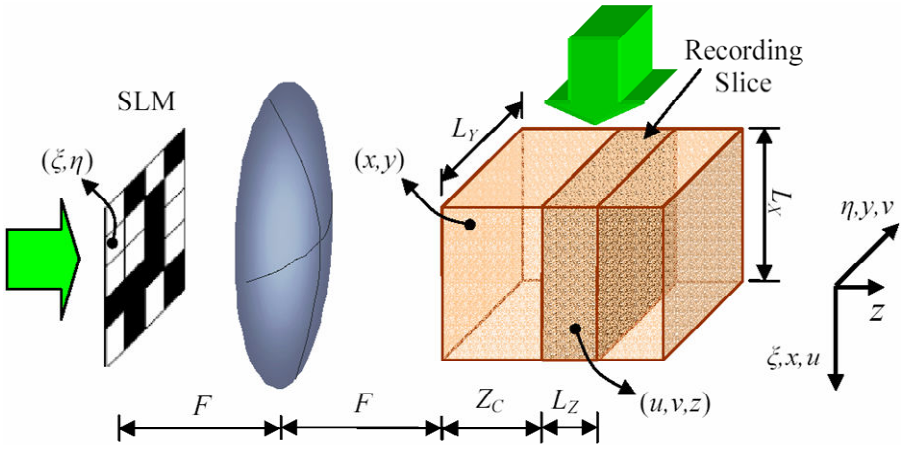

Figure 7. Schematic diagram of an LHC. The recorded slice has dimensions L_X, L_Y, and L_Z in x, y, z directions, respectively. The coordinates of the points in the SLM plane, back focal plane of the lens, and the slice volume are represented by (ξ,η), (x,y), and (u,v,z), respectively. The recorded slice is located at distance Z_C from the back focal plane of the lens (z = 0) with focal length F.

to the interference of the signal beam and the reference beam can be represented as

$$\Delta\varepsilon \propto \left|\exp\left(jk_u u\right) + \mathrm{F}_1(u,v,z)\right|^2 . \tag{2}$$

It is notable that the proportionality constant in Equation (2) depends on the electro-optic properties and the dynamics of the photorefractive effect of the two-center recording material [29] and is not included here for simplicity. Expanding Equation (2), the only component that can produce a Bragg matched diffracted beam during reading by the same pattern at the SLM [i.e., $\mathrm{f}_1(\xi,\eta)$] is

$$\Delta\varepsilon_1 \propto \mathrm{F}_1^*(u,v,z)\exp\left(jk_u u\right). \tag{3}$$

The hologram is then read by another pattern, $\mathrm{f}_2(\xi_2,\eta_2)$ at the SLM plane. The reading field pattern at the recorded slice is calculated similar to the recording field pattern [i.e., Equation (1)] to be

$$\mathrm{F}_2(u,v,z) \propto \iint_{\mathrm{SLM}} \mathrm{f}_2(\xi_2,\eta_2)\exp\left[-j\frac{\pi z}{n\lambda F^2}\left(\xi_2^2+\eta_2^2\right)\right]\exp\left(j\frac{2\pi n z}{\lambda}\right)\exp\left[-j\frac{2\pi}{\lambda F}\left(u\xi_2+v\eta_2\right)\right]\mathrm{d}\xi_2\,\mathrm{d}\eta_2 . \tag{4}$$

The diffracted field in wave-vector space [represented by $\mathrm{A}_\mathrm{d}(\mathbf{k}_\mathrm{d})$] is calculated by using Eqs. (2), (3), (4) and Born approximation [5]

$$\mathrm{A}_\mathrm{d}\left(\mathbf{k}_\mathrm{d}\right) \propto \frac{\iiint_{\mathrm{Volume}} \mathrm{F}_1^*(u,v,z)\exp\left(jk_u u\right)\mathrm{F}_2(u,v,z)\exp\left(-j\mathbf{k}_\mathrm{d}\cdot\mathbf{r}\right)\mathrm{d}u\,\mathrm{d}v\,\mathrm{d}z}{\left[\left(\frac{2n\pi}{\lambda}\right)^2 - k_{dy}^2 - k_{dz}^2\right]^{1/2}}, \tag{5}$$

where $\mathbf{r} = u\mathbf{a}_x + v\mathbf{a}_y + z\mathbf{a}_z$ (with $\mathbf{a}_x$, $\mathbf{a}_y$, and $\mathbf{a}_z$ being unit vectors in x, y (or u, v), and z directions, respectively) and $\mathbf{k}_\mathrm{d}$ represents the diffracted wavevector with magnitude $\left|\mathbf{k}_\mathrm{d}\right| = \left|k_{dx}\mathbf{a}_x + k_{dy}\mathbf{a}_y + k_{dz}\mathbf{a}_z\right| = 2n\pi/\lambda$. It should be noted that the integral in Equation (5)

is performed over the volume of the recording slice. Assuming $A_d(\mathbf{k}_d)$ to be significant only for k_{dy} , $k_{dz} << 2n\pi/\lambda$ (i.e., paraxial approximation for a plane wave in $\mathbf{a}_x$ direction), k_{dy} and k_{dz} are neglected in the denominator of Equation (5) to obtain

$$A_d(\mathbf{k}_d) \propto \iint_{SLM} f_1^*(\xi_1,\eta_1)\,d\xi_1\,d\eta_1 \iint_{SLM} f_2(\xi_2,\eta_2)\,d\xi_2\,d\eta_2$$

$$\times \iiint_{Volume} \exp\left\{ j\left[\frac{2\pi}{\lambda F}(\xi_1 - \xi_2) + \frac{2\pi n}{\lambda} - k_{dx}\right]u\right\} \exp\left\{ j\left[\frac{2\pi}{\lambda F}(\eta_1 - \eta_2) - k_{dy}\right]v\right\}$$

$$\times \exp\left\{ j\left[\frac{2\pi}{n\lambda F^2}(\xi_1^2 + \eta_1^2 - \xi_2^2 - \eta_2^2) - k_{dz}\right]z\right\} d\,u\,d\,v\,d\,z\,. \qquad (6)$$

2.3.1 Symmetric Configuration vs. Shifted Configuration

Figure 8 is a schematic illustration of the position of the Fourier transform of the 2D pattern, created by the Fourier transform lens, at the entrance facet of the recoding medium. In Figure 8(a), it observed that if the spatial frequency bandwidth of the 2D pattern is larger than $L_X/2$, then by positioning the entrance facet of the recording medium symmetrically versus the Fourier transform pattern (symmetric configuration) the larger horizontal spatial frequency components of the 2D pattern will be cut off.

As shown in Figure 8(b), the shifting of the recording medium to the left side of the Fourier transform pattern (shifted configuration) enables the best use of the recording medium dimensions and increases the maximum possible spatial frequency bandwidth of the recorded 2D patterns. Using the shifted configuration as shown in Figure 8(b), only half of the Fourier transform pattern at the left side of the *y*-axis enters the crystal. Because the 2D pattern is illuminated by a plane wave, the 2D signal right behind the 2D pattern is real (i.e., there is no accompanying phase variation over the 2D signal), which

results in a symmetric Fourier transform pattern at the focus of the Fourier transform lens. Therefore, by recording half of the Fourier transform pattern all the information of the 2D pattern is preserved. Whether the symmetric configuration or the shifted configuration is used determines the integration limits over the u dimension in Equation (6). For the shifted configuration, the integration range over the u dimension falls on the left side of the origin.

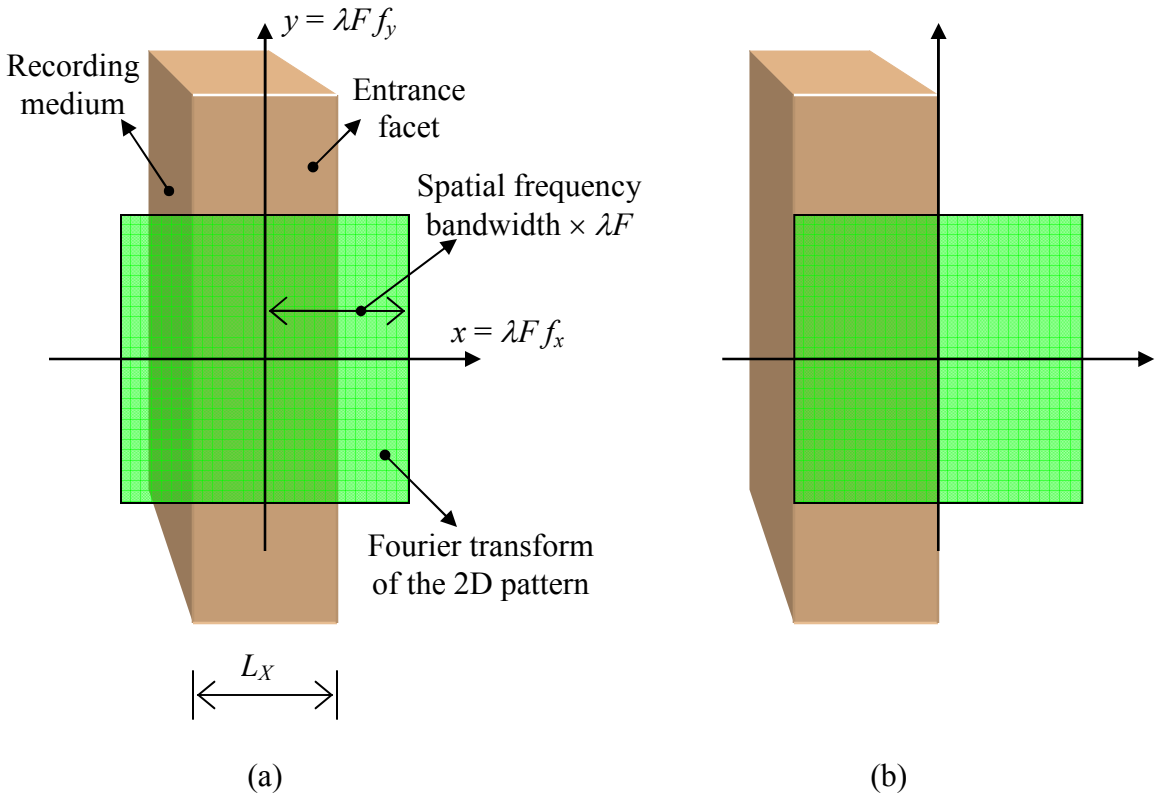

Figure 8. Position of the recording medium entrance facet versus the symmetric Fourier transform of the 2D pattern. (a) The entrance facet is symmetric versus the Fourier transform pattern (symmetric configuration). The larger horizontal spatial frequency components of the 2D pattern are cut off because of the limited L_X. (b) The recording medium is shifted to the left side of the Fourier transform pattern (shifted configuration). Thereby, only the left half of the Fourier transform pattern enters the recording medium and the larger horizontal spatial frequency components of the 2D pattern are preserved.

The integration over the volume of the slice yields

$$\mathrm{A_d}(\mathbf{k_d}) \propto L_X L_Y L_Z \iint_{\mathrm{SLM}} \mathrm{f_1^*}(\xi_1,\eta_1)\mathrm{d}\xi_1\,\mathrm{d}\eta_1 \iint_{\mathrm{SLM}} \mathrm{f_2}(\xi_2,\eta_2)\mathrm{d}\xi_2\,\mathrm{d}\eta_2$$

$$\times \mathrm{sinc}\left\{\frac{L_X}{2\pi}\left[\frac{2\pi}{\lambda F}(\xi_1-\xi_2)+\frac{2\pi n}{\lambda}-k_{dx}\right]\right\}\mathrm{sinc}\left\{\frac{L_Y}{2\pi}\left[\frac{2\pi}{\lambda F}(\eta_1-\eta_2)-k_{dy}\right]\right\}$$

$$\times \mathrm{sinc}\left\{\frac{L_Z}{2\pi}\left[\frac{\pi}{n\lambda F^2}\left(\xi_1^2+\eta_1^2-\xi_2^2-\eta_2^2\right)-k_{dz}\right]\right\}\exp\left\{-\frac{L_X}{2}\left[\frac{2\pi}{\lambda F}(\xi_1-\xi_2)+\frac{2\pi n}{\lambda}-k_{dx}\right]\right\}$$

$$\times \exp\left\{j\left(Z_C+\frac{L_Z}{2}\right)\left[\frac{\pi}{n\lambda F^2}\left(\xi_1^2+\eta_1^2-\xi_2^2-\eta_2^2\right)-k_{dz}\right]\right\}, \tag{7}$$

with $\mathrm{sinc}(x) = \sin(\pi x)/\pi x$. In the following steps, it is assumed that the dimension of the slice in y (or v) direction (i.e., L_Y) is large enough to approximate the second sinc function in Equation (7) as an impulse (or delta) function. Integration over η_2 then yields

$$\mathrm{A_d}(\mathbf{k_d}) \propto L_X L_Z \iint_{\mathrm{SLM}} \mathrm{f_1^*}(\xi_1,\eta_1)\mathrm{d}\xi_1\,\mathrm{d}\eta_1 \int_{\mathrm{SLM}-\xi} \mathrm{f_2}(\xi_2,\eta_1+\Delta\eta)\mathrm{d}\xi_2$$

$$\times \mathrm{sinc}\left(\frac{L_X}{2\pi}\beta\right)\mathrm{sinc}\left(\frac{L_Z}{2\pi}\alpha\right)\exp\left(-\frac{L_X}{2}\beta\right)\exp\left[j\left(Z_C+\frac{L_Z}{2}\right)\alpha\right], \tag{8}$$

where

$$\alpha = \frac{\pi}{n\lambda F^2}\left(\xi_1^2-\xi_2^2-2\eta_1\Delta\eta-\Delta\eta^2\right)-k_{dz}, \tag{9}$$

$$\beta = \frac{2\pi}{\lambda F}(\xi_1-\xi_2)+\frac{2\pi n}{\lambda}-k_{dx} \tag{10}$$

$$\Delta\eta = -\frac{\lambda F}{2\pi}k_{dy}, \tag{11}$$

and SLM-ξ means the ξ-direction (or x-direction) in the SLM plane. For the symmetric configuration, the integration range over the u dimension in Equation (6) is symmetric about the origin. Therefore, in Equation (8) the first exp(.) multiplier does not appear for the symmetric configuration. In the rest of this chapter, the shifted configuration is used.

The detector array is located right below the bottom face of the crystal. The EM field in position space at the detector plane (i.e., $u = 0$ plane) is then calculated as

$$\mathrm{E}(v,z) = \int_{-\infty}^{\infty}\int_{-\infty}^{\infty} \mathrm{A}_{\mathrm{d}}(\mathbf{k}_{\mathrm{d}}) \exp\left[j\left(k_{dy}v + k_{dz}z\right)\right] \mathrm{d}k_{dy}\,\mathrm{d}k_{dz} \,. \tag{12}$$

In these derivations, the x-dimension (or u-dimension) of the recording slice (i.e., L_X) is not assumed to be infinite, because the variation of the height of the recording slice significantly changes the crosstalk and shift-invariance as will be explained in Section 2.4. In fact, it is expected so, because that is the propagation direction of the diffracted beam and if any phase mismatch occurs, it adds up throughout the propagation path of the diffracted beam inside the recording medium.

2.4 Performance Simulations of LHC

To compare the performance of conventional optical correlators with that of the localized holographic correlator (LHC), Three performance measures: shift selectivity, crosstalk, and capacity are considered. These performance measures are calculated using the theoretical derivations of Section 2.3.

In all of the simulations, the recording material is assumed to be a doubly doped $LiNbO_3$ crystal with average ordinary refractive index of 2.3. The crystal height (L_X) is assumed 1.6 mm, which is the height of the actual crystal. The recording and reading

wavelength is 532 nm. The thickness of each recording slice is 16 μm. The width of each detector cell in the detector array is also 16 μm. The images are random pixelated patterns with 28 μm pixel pitch. It is assumed that the average of the field values is removed by DC blocking at the Fourier plane of a 4-f imaging system with a magnification of 1.5 (not shown in Figure 7). Therefore, the pixel pitch of the image pattern is 42 μm. The focal length of the lens after the imaging system (the Fourier transform lens) is 12.5 cm. The reason that this focal length has been chosen is that it has been intended to let half of the Fourier transform of the image (half of the main lobe of the sinc function corresponding to the square pixels of the recorded patterns) enter the crystal to preserve the spatial bandwidth of the correlated patterns. The location of the recording slice, Z_C, is arbitrarily chosen, because according the simulations, it has no effect on the performance measures of the LHC.

2.4.1 Crosstalk

Crosstalk is defined as the detected noise power in the place of a non-existing (or empty) pattern (or hologram) produced by other stored patterns (or holograms). It is usually quantified by crosstalk noise to signal ratio (NSR), which is the ratio of the crosstalk noise power to the signal power diffracted from the hologram corresponding to a desired pattern. As it is usual in crosstalk calculations for optical correlators, the worst case scenario is considered for both conventional correlators and LHCs. In this scenario, it is assumed that all the recorded holograms are recorded with one pattern for all. During correlation, the holograms are read with the same pattern to maximize the unwanted crosstalk [38].

In conventional holographic correlators that use angular multiplexing method, the correlation pattern of the incoming signal beam with the stored patterns is formed at the output plane (i.e., the focal plane of a Fourier transforming lens) [38]. The central peaks of the correlation patterns fall at points corresponding to the reference beam angles with which the stored patterns are recorded. The sidelobes of the correlation patterns, however, may occur at the locations of the peaks of the other correlation patterns and cause crosstalk. In volume holograms, the mentioned sidelobes get suppressed as the thickness of the recording medium increases, which in turn decreases the crosstalk [38]. This suppression occurs because of the angular selectivity of volume holograms [5]. The amount of crosstalk also depends on the examined pattern and the geometry of the correlation system, such as the focal lengths of the lenses, and the angles of the signal and the reference beams.

The reported theoretical values for crosstalk in angle multiplexed correlators in Reference [38] indicate that for a crosstalk NSR of -30 dB in a 5 mm thick medium the number of stored holograms can be as much as 12000, if the material has enough dynamic range. This is obtained when the angle between the reference and the signal beams is 90° inside the crystal (i.e., 90-degree geometry). One can imply that for a 1 cm thick medium this number can be 24000 since the width of the angular selectivity function, which is a sinc function [5], is inversely proportional to medium thickness. The acceptable crosstalk level sets a limit for the maximum number of stored patterns in an optical correlation system. This number is defined as the capacity of the correlation system.

For the LHC, the recording of holograms corresponding to identical patterns at (ξ,η) plane in successive slices of the recording medium is simulated and the crosstalk NSR, produced by reading those holograms with the same pattern placed at (ξ,η) plane is calculated. Crosstalk in LHCs can be reduced by adding spacing (i.e. a buffer region) between the adjacent slices. Figure 9 shows the variation of the crosstalk NSR with this spacing. For a 1.6 mm high medium (i.e., L_X = 1.6 mm in Figure 7), the curve shows that for a NSR equal to -30 dB, the spacing between adjacent slices is 17 μm. Since the thickness of each slice is 16 μm, 16 + 17 = 33 μm of the crystal length is devoted to each slice. Thus, it is possible to have 303 slices per 1 cm of crystal length.

As shown in Figure 9, the crosstalk NSR is increased as the height of the crystal is increased. This in turn decreases the capacity of the system, as the acceptable spacing between the adjacent slices has to increase to maintain the same amount of crosstalk NSR. The reason for this variation of crosstalk NSR with L_X is shown in Figure 10, which depicts the intensity profile along the z-axis. It is clear from Figure 10 that the diffracted beam becomes wider in the z-direction as the height of the crystal increases, which in turn increases the crosstalk NSR. It can be shown that in the limit, where the height of the crystal is infinite, the diffracted beam is a plane wave, no matter how thick the slices are, and it is impossible to separate the diffracted signals coming from different slices.

A quantitative comparison of crosstalk in the two types of correlation (i.e., localized and conventional) depends on the actual design of the two systems. However, as it will be discussed in Section 2.4.3, crosstalk is not a limiting factor in designing conventional angle-multiplexed correlators with maximum capacity. Usually, the dynamic range limitation is the dominant effect and the crosstalk NSR obtained for the

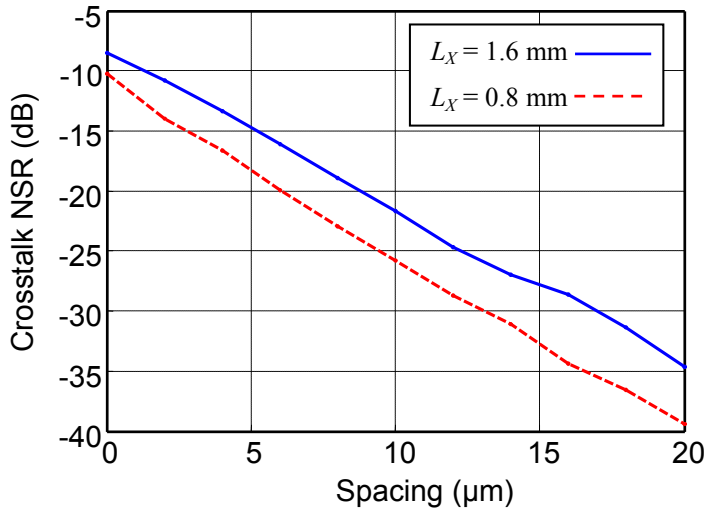

Figure 9. Crosstalk NSR vs. spacing between slices in a LHC with 1.6 mm and 0.8 mm high doubly doped $LiNbO_3$ crystals with 16 μm thick recording slices. λ = 532 nm, and F = 12.5 cm.

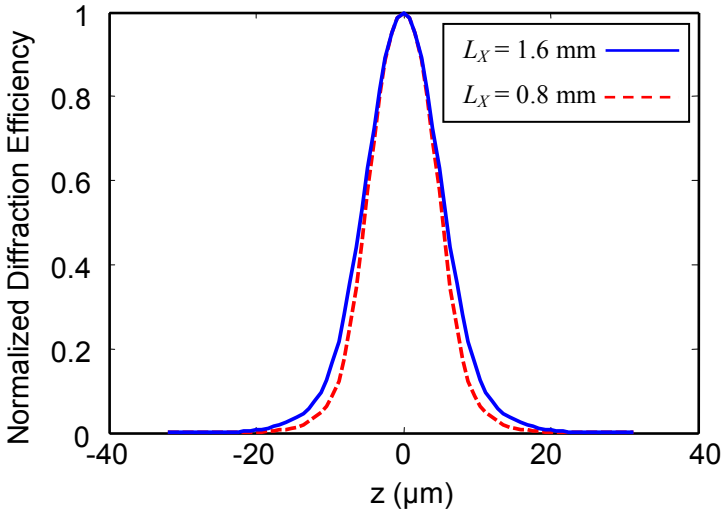

Figure 10. Intensity profile of the diffracted beam from a single hologram in a LHC along the z-axis at the bottom facets of L_X = 1.6 mm and L_X = 0.8 mm high $LiNbO_3$ crystals with 16 μm thick recording slices. λ = 532 nm, and F = 12.5 cm.

maximum capacity correlators in conventional design, is well below the required minimum value (for example -30 dB). On the other hand, crosstalk in LHCs depends on the thickness of the buffer layer, which affects the capacity as well. For practical designs, LHCs can be designed to have crosstalk NSR below the required minimum value by choosing reasonable buffer sizes (17 μm as mentioned above).

2.4.2 Shift-Invariance

In holographic correlators, shifting the reading pattern away from its position during recording reduces the diffraction efficiency because of the Bragg mismatch [5]. The shift-invariance is quantitatively defined as the minimum amount of shift required to reduce the diffraction efficiency to zero. Here, the shift-invariance of angular multiplexed correlators and that of LHCs are compared. Only in-plane shift-invariance (in the *x*-direction in Figure 7) is considered in this comparison, because for both cases the out-of-plane shift-invariance (in the *y*-direction in Figure 7) is more than one order of magnitude larger than the in-plane shift-invariance. This is because of the closeness to the degeneracy direction [39].

The amount of shift invariance depends on the geometry of the system and thickness of the holograms along the diffracted beam. In angular multiplexing, this thickness determines the width of the sinc function explained in Section 2.4.1, which in turn determines the shift invariance [5]. The wider the sinc function, the larger is the shift-invariance. On the other hand, the wider the sinc function, the larger is the crosstalk. This in turn limits the capacity of the correlator. Therefore, a trade-off exists between shift-invariance and capacity. In fact, some methods like defocusing [40] have been exploited to control the shift-invariance in order to increase the capacity of the optical

correlators. Figure 11 shows the shift-invariance for an angular multiplexed correlator, which works in the focused regime. The material is assumed to be a 1 cm thick (measured in the *z* direction in Figure 7) and 1.6 mm high (measured in the *x* direction in Figure 7) $LiNbO_3$:Fe crystal. The signal beam angle with respect to the normal axis is zero and the SLM pixel pitch size is 42 μm. Both transmission and 90-degree recording geometries are considered in Figure 11. It is observed that for the 90-degree geometry, the shift-invariance is fixed at 1 pixel (42 μm).

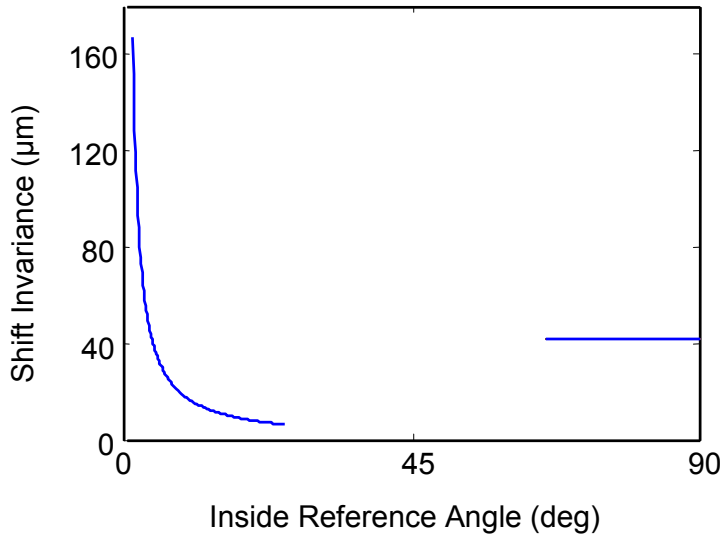

Figure 11. In-plane shift-invariance in an angle-multiplexed correlator with 1 cm thick $LiNbO_3$:Fe crystal with λ = 532 nm, F = 12.5 cm, and pixel pitch size = 42 μm. The two segments of the curve correspond to transmission (left) and 90-degree geometry (right) and the gap in between represents the inside angles for which no incident outside angle from air exist.

Figure 12 shows the simulated variation of the diffraction efficiency with image shift in a LHC. The curve is a little shifted to the right. This is on account of the unsymmetrical configuration of the recording setup because of the reference arm lying on

one side of the signal arm as illustrated in Figure 7, and also because of the slices being thin in the z-direction. The shift-invariance for a LHC with L_X = 1.6 mm and L_Z = 16 μm slice thickness is about 1 pixel (42 μm) and as simulated, it is constant for different locations of slices within the crystal. This is the same as the shift-invariance in conventional correlators, where the holograms are angle multiplexed in 90-degree geometry, as described in the previous paragraph, maintaining the same medium dimensions, pixel size, and focal length.

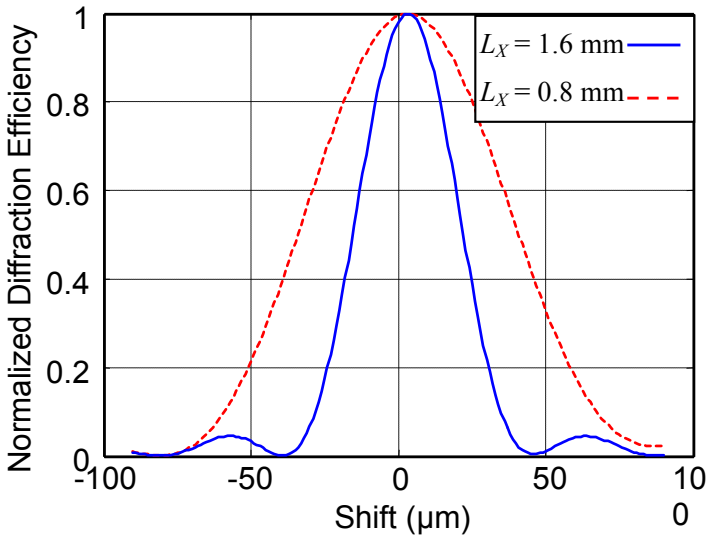

Figure 12. Normalized diffraction efficiency vs. in-plane image shift in LHCs with L_X = 1.6 mm and L_X = 0.8 mm high doubly-doped $LiNbO_3$ crystals, slice thickness = 16 μm, λ = 532 nm, F = 12.5 cm, and pixel pitch size = 42 μm.

As shown in Figure 12, the shift invariance becomes larger as the height of the crystal decreases. The reason is that the diffracted beam in Figure 6(b) propagates in the x-direction, resulting in a smaller phase mismatch along the x-direction for shorter holograms (with smaller L_X) for the same in-plane shift of the reading image. However, it

should be noted that for smaller L_X the maximum allowed spatial frequency of the correlated images decreases and larger pixels have to be used. In that case, the shift invariance will be still 1 pixel.

2.4.3 Capacity

As mentioned previously, the maximum number of stored patterns in an optical correlation system defines its capacity. Here, the effects of the diffraction efficiency η, and the dynamic range, *M*/# [41], on the capacity are studied. For the conventional angle-multiplexed holograms recorded in the same volume, it is shown that the theoretical maximum *M*/# for a 1 cm thick singly doped $LiNbO_3$:Fe crystal is 30 for transmission geometry with recording wavelength λ = 514 nm [42]. This implies that if one chooses the minimum acceptable diffraction efficiency to be $\eta = 10^{-4}$, the maximum number of holograms will be

$$M = \frac{M/\#}{\sqrt{\eta}} = \frac{30}{\sqrt{10^{-4}}} = 3000/\text{cm}. \tag{13}$$

In the 90-degree geometry, the theoretical maximum *M*/# for the same material with the dimensions $L_X = L_Z = 1$ cm, is 16 [42]. Thus, with the same diffraction efficiency the maximum number of holograms is 1600/cm. Comparing this number with 24000, calculated in Section 2.4.1, it is observed that the major limit on the capacity in conventional holographic correlators is *M*/# and not the crosstalk. If the same crystal as the one used for localized recording is considered (L_X = 1.6 mm and L_Z = 1 cm) then the dynamic range reduces to $M/\# = 16 \times (1.6/10)^{1/2} = 6.4$ [43], which results in the capacity of 640/cm.

In localized recording, a doubly doped $LiNbO_3$:Fe:Mn crystal is used in the 90-degree geometry. It is shown that in this case, the maximum *M*/# for sensitization at 404 nm and recording at 532 nm is 0.24 (for each slice) [30], resulting in $\eta = 5.76 \times 10^{-2}$ for each hologram, which is 576 times larger than the minimum acceptable diffraction efficiency chosen in the previous paragraph for conventional correlators. This implies that it is possible to multiplex $(576)^{1/2} = 24$ holograms in a single slice with $\eta = 10^{-4}$ for each hologram. They can be exploited for different versions of a single pattern like shifted or rotated or scaled versions. Since all these holograms correspond to the same object, they are recorded using the same reference beam in one slice. Reading the holograms with each recorded pattern (corresponding to the same object) results in diffraction of the same reference beam, which will be detected at the detector next to the slice. This makes the LHCs much more robust to the variations of the correlated images. In addition, this capability can be exploited to develop practical three-dimensional object recognition systems, which is further discussed in Chapter 4. It is observed that by tuning the slice thickness one can change the number of possible multiplexed holograms per slice (or the diffraction efficiency if multiplexing within individual slices is not desired) and the number of slices.

If the number of multiplexed holograms in a single slice is multiplied by the maximum number of slices per 1 cm length, calculated in Section 2.4.1, the result will be $24 \times 303 = 7272$ holograms stored in a 1 cm length of doubly-doped $LiNbO_3$ crystal (in contrast to 1600 holograms in conventional correlators with 90-degree recording geometry, as described above). The result may seem surprising while the M/# of a singly doped $LiNbO_3$ crystal is usually larger than that of a doubly doped $LiNbO_3$ crystal with

the same dimensions. One should notice, however, that in localized recording the diffraction efficiency of the recorded holograms is proportional to $1/M$ with M being the number of the recorded holograms [35]. The diffraction efficiency in conventional volume holography follows a $1/M^2$ dependence [13], which more severely limits the number of recorded holograms.

2.5 Discussion

The performance characteristics of the conventional correlators and LHCs are summarized in Table 1. From Table 1, one can realize that the LHC has higher capacity while the crosstalk in both methods is comparable and the shift invariance is the same. However, it should be noted that the point of the investigated method is not that the LHCs improve considerably the conventional performance measures. It is rather the whole new possibilities for obtaining practical capabilities that could not be achieved with conventional correlators. A unique property of LHCs is the possibility of erasing and re-recording in each slice without affecting other slices. Therefore, dynamic modification of the pattern database is possible.

Table 1. Performance characteristics of conventional correlator and LHC

Method	Shift Invariance	Crosstalk NSR	Capacity Per cm Thickness	Size	Selective Recoding /Erasure	Elongation Possibility
Conventional (Angular - 90°)	1 pixel	< -30 dB	1600	Large	NO	NO
LHC	1 pixel	< -30 dB	7272 (in 303 groups)	Compact	YES	YES
	The holograms are persistent in LHCs					

Moreover, by using long crystals (L_Z = 5-10 cm in Figure 13) it is possible to considerably increase the capacity as shown in Figure 13. This is not possible in conventional holography because of the absorption of the recording and reading beams through the crystal. Furthermore, the detectors in the detector array contact the bottom Moreover, by using long crystals (L_Z = 5-10 cm in Figure 13) it is possible to considerably increase the capacity as shown in Figure 13. This is not possible in conventional holography because of the absorption of the recording and reading beams through the crystal. Furthermore, the detectors in the detector array contact the bottom surface of the crystal and no lens is required to collect and focus the diffracted correlation beams in LHCs [Figure 1(b)]. This makes the LHC a more compact system. Finally, in LHCs patterns are recorded by gated holographic techniques, which make the holograms persistent against further reading.

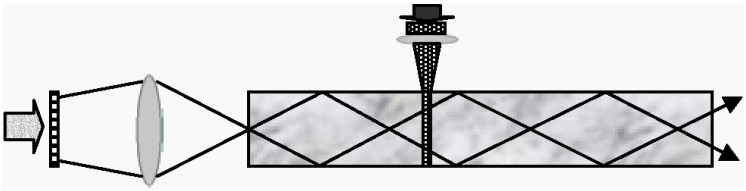

Figure 13. Index waveguiding in localized holographic correlator with long crystals to increase the capacity.

CHAPTER 3

PERFORMANCE MEASUREMENTS OF 2D LHC

3.1 Introduction

In Chapter 2, the theoretical framework of a new class of holographic correlators based on the localized recording technique [34] was introduced, which can be implemented using a gated holographic recording scheme such as two-center recording in doubly doped $LiNbO_3$ crystals [29]. By use of gated holography, the recording and erasure of the holograms are only possible in the presence of a gate beam. In this Chapter, the experimental results are presented showing the correlation capability, crosstalk, shift invariance, and the capability of dynamic content modification of the LHC [44]. Several persistent holograms are recorded within separate slices as close as 33 μm apart along the crystal. To the best of the author's knowledge, this distance between the adjacent slices is the smallest reported for localized holography. Individual holograms are dynamically erased and re-recorded with no need to refresh all other recorded holograms. The results demonstrate unique performance and capabilities for these correlators.

3.2 Experimental Setup

Figure 14 is a schematic illustration of the LHC experimental setup. The 532 nm expanded laser beam from a continuous wave (CW) diode-pumped solid state laser illuminates a mask, which modulates the signal beam with a random pixelated pattern during the recording and correlation phases, respectively. In a practical system, the mask is substituted with an spatial light modulator (SLM) for dynamic pattern modification.

The DC component of the signal beam is then filtered out at the origin of the Fourier plane of a 4-f imaging system comprising two confocal lenses F1 and F2. All of the correlated patterns have the common DC component, which is originated by the pixelated mask being an intensity modulator; therefore, negative values of electromagnetic field (with 180 degree phase shift) cannot be generated. Eliminating this common part of the spatial spectrum of the patterns significantly improves the contrast of the correlation process.

All the diffraction sidelobes due to the square shape of the mask pixels are also blocked at the focal plane of lens F1. The magnification ratio of the 4-f system is 1:1.5. The filtered pattern is then Fourier transformed by lens F3 at the entrance facet of the holographic crystal. The shifted configuration for the position of the crystal versus the Fourier transform pattern is used.[1] The focal lengths are chosen to have half of the Fourier transform pattern fit to the crystal width (L_X in Figure 14), and the crystal is positioned accordingly. As mentioned in Section 2.3.1 in Chapter 2 for the shifted configuration, this doubles the spatial bandwidth of the system while maintaining the same crystal width.

The reference and the UV gate (wavelength 404 nm from a diode laser) beams are coaligned and are focused by the cylindrical lens CL1 inside the crystal at the same location, where they form two overlapping slices of light that define the recording slice. Before merging these two copropagating beams, they are filtered and shaped like 1D Gaussian beams by two separate sets of confocal cylindrical lenses [(CL2,CL3) for the reference and (CL4,CL5) for the UV] and slits. The slits remove the fringes that would appear around the main light slice. This significantly reduces the crosstalk between

[1] Refer to Section 2.3.1 in Chapter 2 for shifted configuration versus symmetric configuration.

adjacent slices. Also, the holograms can be selectively recorded and erased within select slices without affecting neighboring holograms.

The recording medium is a 45-degree-cut congruently grown $LiNbO_3$:Fe:Mn crystal doped with 0.15 wt% Fe_2O_3 and 0.02 wt% MnO. The crystal dopant contents are optimized to acquire high sensitivity and high dynamic range (M/# parameter) at the same time [30]. The crystal is annealed at 1070°C in oxygen atmosphere for 48 hours. All of the parameters of the setup have been selected according to the values mentioned in Chapter 2. The crystal width is L_X = 1.6 mm. The random pixelated pattern on the mask is a checkerboard pattern of 450 × 450 dark and bright square pixels with 28 μm × 28 μm pixel size. Because of the 1:1.5 magnification ratio of the 4-f imaging system, the effective pixel size of the recorded pattern is p = 28 × 1.5 = 42 μm. In all of the

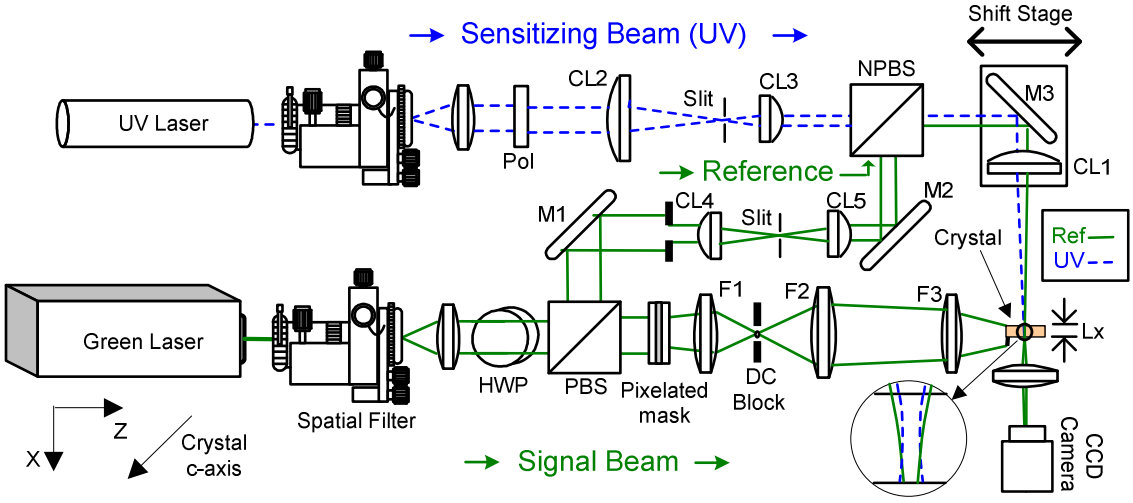

Figure 14. LHC experimental setup. The recording medium is a 45-degree-cut congruently grown $LiNbO_3$:Fe:Mn crystal doped with 0.15 wt% Fe_2O_3 and 0.02 wt% MnO. HWP: half-wave plate, PBS: polarizing beamsplitter, NPBS: non-polarizing beamsplitter, F1, F2, and F3: Fourier transform lens, CL: cylindrical lens, Pol: polarizer, M: mirror. Lens focal lengths: f_1 = 20 cm, f_2 = 30 cm, f_3 = 12.5 cm, f_{CL1} = 5 cm.

experiments presented in this chapter, the intensities of the recording reference and signal beams and that of the UV beam are 300 mW/cm^2, 300 mW/cm^2, and 40 mW/cm^2, respectively.

Figure 15 illustrates the arrangements of the reference and gate beams. The beam waist diameters ($2w_0$) of the reference and UV Gaussian beams are 18 μm, which is equivalent to a 16 μm wide rectangle, in terms of the area under the corresponding field profiles. This is conforming with the 16 μm width used in Chapter 2. The full width of the UV beam within the crystal defines the slice thickness. The waist of the UV beam occurs in the center of the entrance and exit facets of the crystal. The waist of the reference beam is located at the exit facet of the crystal, where the detector array is planned to be attached (or placed in close proximity). The location of the two overlapping beams (i.e., reference and UV) along the crystal is controlled by a precision translation stage, which shifts the focusing cylindrical lens CL1. For simplicity, in all the

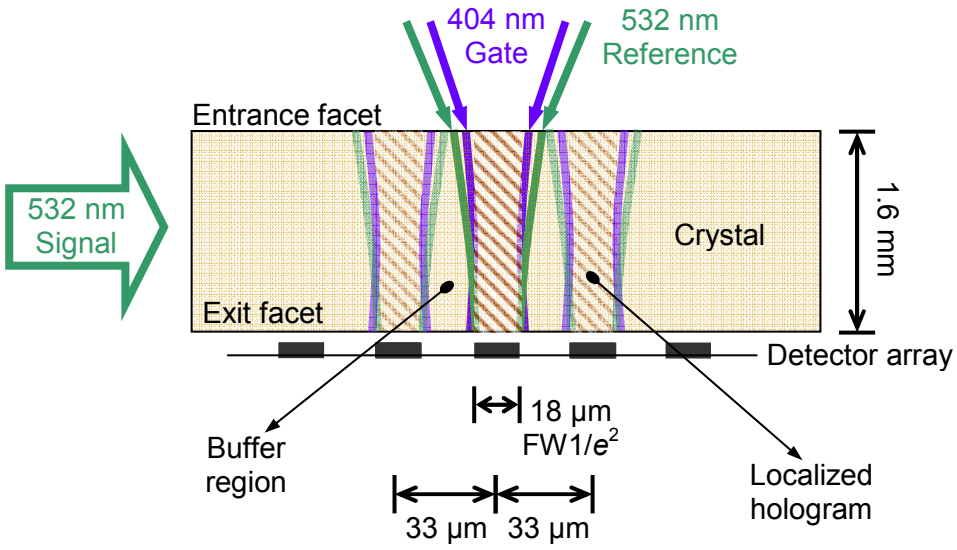

Figure 15. Arrangements of the reference and gate beams

demonstrations of the LHC, the diffracted correlation signal at the exit facet of the crystal is imaged onto a CCD camera by a lens, rather than being collected by a detector array.

The holograms are recorded within the sensitized slices, which are 33 μm apart from each other. Comparing the 33 μm slice distances to the width of the sensitized slices (about 18 μm) it is notable that a buffer space is added between adjacent holograms to reduce crosstalk between adjacent holograms. To the best of the author's knowledge, the 33 μm distance between the adjacent slices is the smallest reported to date for localized holography.

3.3 Crosstalk

To investigate the crosstalk in LHCs, the experimental setup in Figure 14 is used to record localized holograms of random patterns in seven slices. The results of the crosstalk experiment are presented in Figure 16. The holograms were recorded in order from right to left, each for 180 seconds with no pre-sensitizing. The pictures on top of the curves are the images of the diffraction signals at the CCD in Figure 14. In both (a) and (b) curves, the intensity values are normalized to the intensity value at the largest diffraction peak among all holograms in each case.

To study the crosstalk in the worst case scenario, the center slice is left blank (i.e., no hologram recorded) and used the same mask for all other six holograms. The holograms were then read by the same mask used for recording. The diffracted signals at all seven slices are shown in Figure 16(a). Because there is no hologram recorded within the gap at the center slice in Figure 16(a), the power collected at this slice is initiated from the tails of the diffraction profiles of the neighboring holograms and small scatterings, which is defined as crosstalk [36]. Figure 16(a) clearly shows the negligible

crosstalk in LHCs. The crosstalk noise to signal ratio (NSR), which is the ratio of the power at the location of the missing hologram to that at the adjacent peaks, is about -20 dB.

This experiment was repeated with the same mask used for six holograms, but instead of leaving the center slice blank, a different mask with a random pattern totally uncorrelated with the one used for recording the other six holograms was used for recording a hologram there. The holograms were then read by the same mask used for recording the six surrounding holograms. The diffracted signals at all the seven slices are shown in Figure 16(b). The collected power at the middle slice represents the cross-correlation of the reading pattern and that used for recording of the middle hologram plus the crosstalk caused by diffraction from adjacent holograms at the middle slice. Comparing Figure 16(a) and Figure 16(b), it is observed that the amount of power at the location of the unmatched hologram [in the middle slice in Figure 16(b)] is about the same as that at the location of the blank slice [in the middle slice in Figure 16(a)]. One can observe that the system does the cross-correlation well with good discrimination. All the crosstalk is initiated from the tails of the diffraction profiles of the neighboring holograms and small scatterings.

It is notable in Figure 16 that the strength of the six holograms is decreasing from left to right. The explanation for this effect is as follows: The holograms have been recorded in order from right to left. During the recording of each hologram, the signal beam reads previously recorded holograms, which results in partially erasing them. There is a partial loss of persistence while reading the two center recorded holograms with green light [45] that causes the observed partial erasure. This effect does not exist with

red light beams. However, working with green beam with higher photon energy results in much better performance in terms of both the sensitivity and diffraction efficiency. To overcome the erasure problem, instead of equal recording times for all of the holograms, a schedule can be calculated for the recording times based on the recording and erasure time constants, which results in equal strengths of the recorded holograms [46].

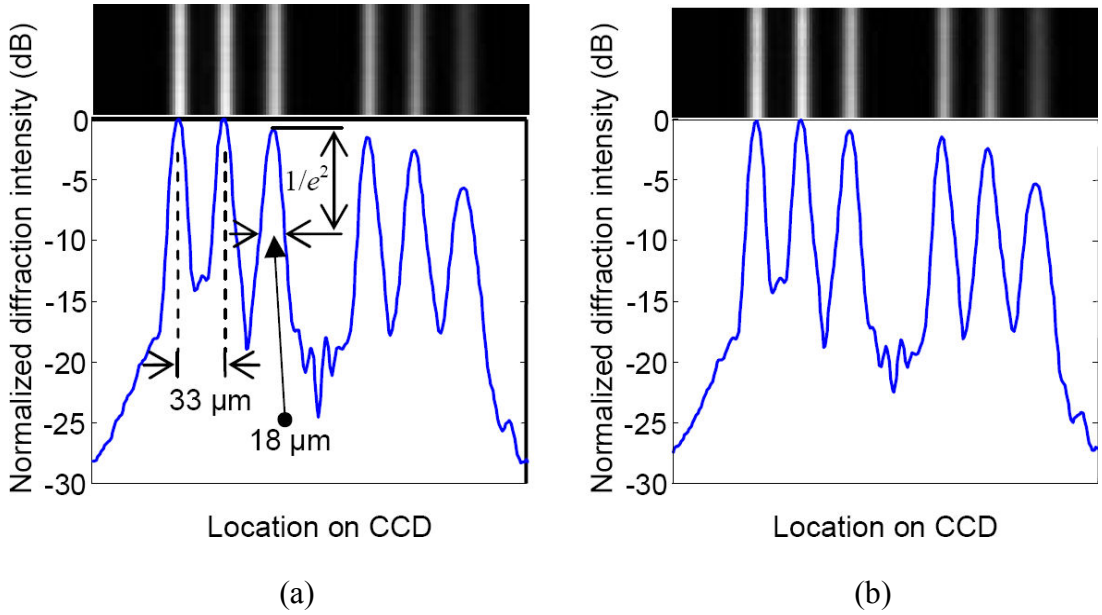

Figure 16. Crosstalk measurement in LHCs. Diffraction signals from six localized holograms are shown that were recorded with the same random pattern as the one reading them. The pictures on top of the curves are the images of the diffraction signals at the CCD in Fig. 2. The holograms were recorded in order from right to left, each for 180 s with no presensitizing. The intensities of the recording reference and signal beams and that of the UV beam are 300, 300, and 40 mW/cm2, respectively. Two cases are demonstrated: (a) no hologram is recorded in the middle slice, and (b) a hologram with a totally uncorrelated random pattern is recorded in the middle slice. In both (a) and (b) curves, the intensity values are normalized to the intensity value at the largest diffraction peak among all holograms in each case.

3.4 Shift Invariance

Another important property of any correlator is shift-invariance, which is defined as the minimum amount of the lateral shift of the matched reading pattern required to reduce the diffraction efficiency to zero [36]. To study the shift-invariance of the LHC, one hologram was recorded in one slice. The hologram was then read by the same mask used for the recording but the mask was shifted by different amounts between the readings. The in-plane shift was applied (i.e., in the *x*-direction in Figure 14). The diffraction efficiency was measured per each shift value. Figure 17 shows the diffraction efficiency, normalized to the diffraction efficiency at no shift, as a function of the in-plane shift in the reading pattern. The shift invariance approximately equals the effective pixel pitch: 42 μm. To examine the validity of this result, the in-plane shift-invariance is calculated with the parameters of the experiment using the formulation in Section 2.3. The

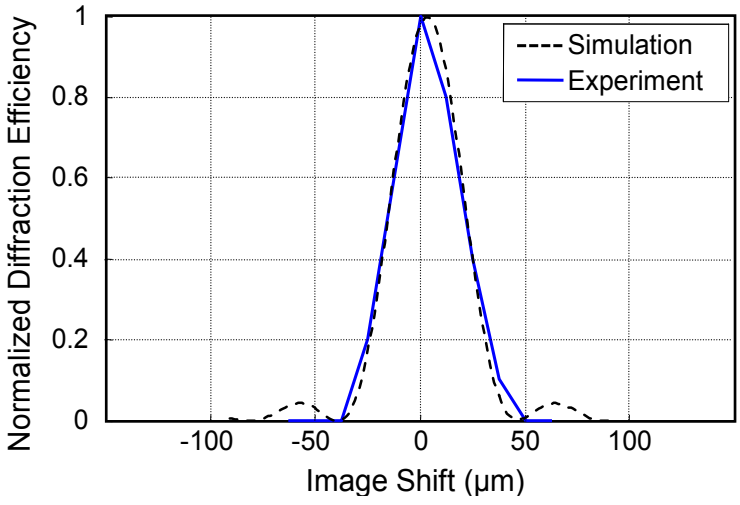

Figure 17. Shift invariance of the LHC, simulation and experiment. The in-plane shift (in the *x*-direction in Figure 14) is applied. The horizontal axis corresponds to the shift of the magnified pattern behind lens F2 in Figure 14. The pixel pitch of the magnified pattern is 42 μm.

theoretical results are also shown in Figure 17. It is observed that the simulation and experimental results agree well. Both the simulation and experimental curves show asymmetry in the response to the in-plane shift, which is because of the asymmetry of the grating vector (directed along the *c*-axis) with respect to the *z*-axis (Figure 14).

3.5 Dynamic Content Modification

A unique advantage of the LHC is the possibility of dynamic modification of the pattern database. Figure 18 shows how it is possible to erase one hologram among 10 surrounding holograms without affecting them. In Figure 18(a) the diffraction intensity profiles from 11 localized recorded holograms are depicted. The holograms have been recorded from right to left. Figure 18(b) shows the intensity profiles after the middle hologram is erased by illuminating it with the UV and the reference beams for 20 minutes. One can observe that the ratios of the intensities of the surrounding holograms are almost unchanged. Figure 18(c) shows this effect more quantitatively. The diffraction from the middle hologram is decayed by 14 dB after 30 minutes of erasure, while the diffraction from the right side hologram is decreased only by 0.3 dB. The left side hologram shows more erasure because it was recorded later than the other two and its fast erasure step was not passed completely before the erasure of the middle hologram [27].

To further investigate the dynamic recording and erasure capability, seven holograms are recorded with the same mask. The holograms were then read by the same mask. The diffracted signals are shown in Figure 19(a). The recording times varied from 15 minutes for the right side hologram (first recorded), exponentially reduced from one slice to another, to 2 minutes for the left side one (last recorded) with no pre-sensitizing

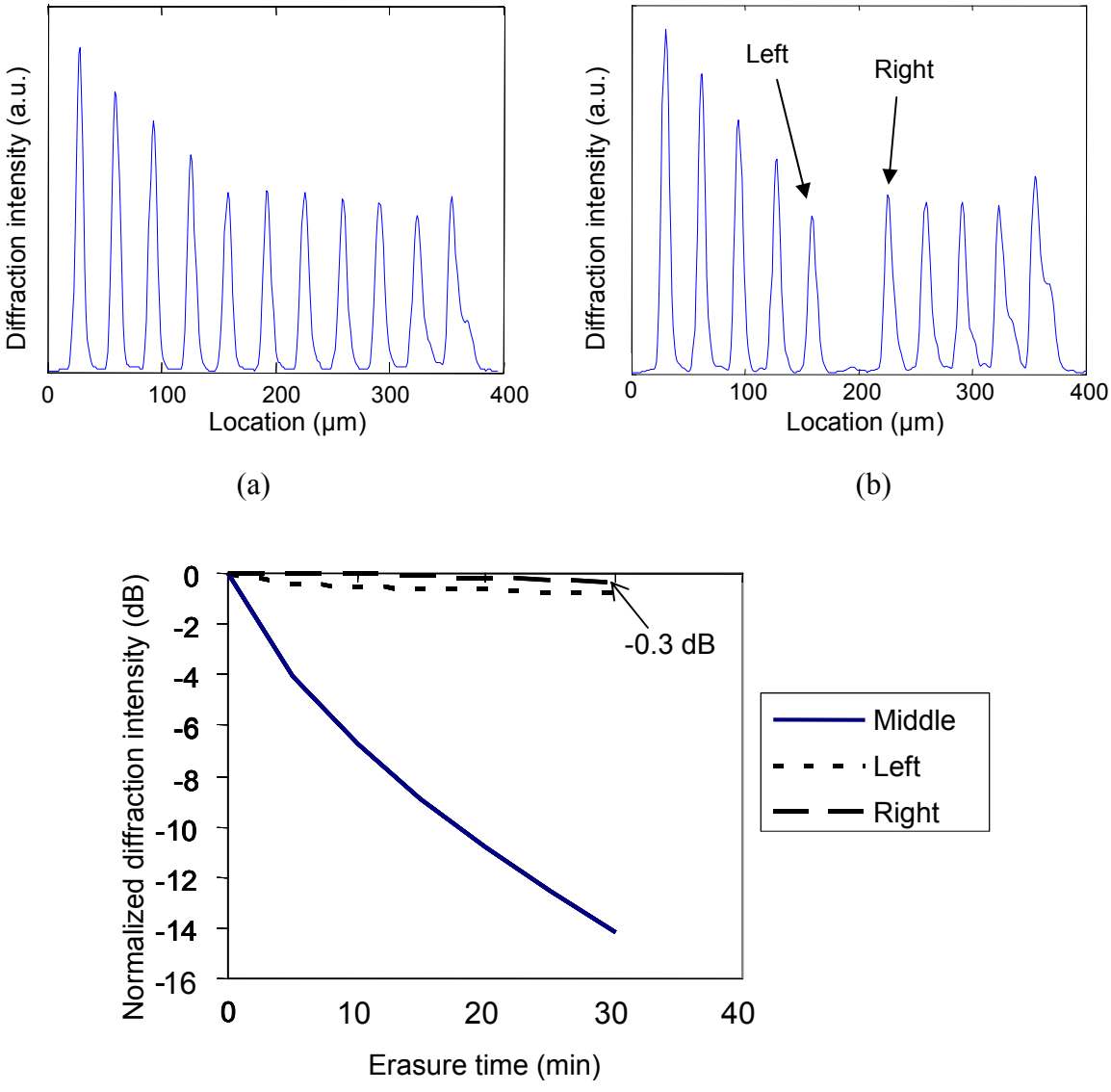

Figure 18. Erasing one hologram with the surrounding holograms unaffected. (a) Diffraction intensity from 11 holograms recorded 33 μm apart from each other. (b) Erasing the middle hologram for 20 minutes. (c) Normalized diffraction intensity from three adjacent holograms while the middle one is being erased. The power for each hologram is normalized to its value at the beginning of the erasure process.

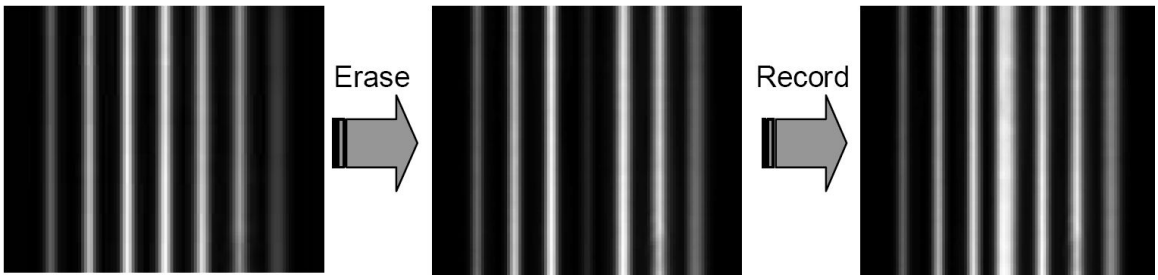

(a) (b) (c)

Figure 19. Dynamic recording/erasure in LHC. (a) Seven holograms are recorded in order from right to left. (b) The hologram at the center is erased by illuminating it with the UV and reference beams, and (c) the hologram at the center is re-recorded for 2 minutes. The intensities of the recording reference and signal beams and that of the UV beam are 300, 300, and 40 mW/cm2, respectively.

phase. Then, the middle hologram was erased by illuminating the middle slice with the UV beam and the reference beam for 20 minutes without changing their intensities.

After erasure, the holograms were read by the recording mask and the diffracted signal is shown in Figure 19(b). The erasure time was selected properly so that the diffraction efficiency of the middle hologram was significantly reduced. The erasure time is larger than the typical recording time because of Bragg-matched erasure. The erased hologram was then re-recorded for 2 minutes. Then, the holograms were read by the recording pattern and the diffracted signals are shown in Figure 19(c). The neighboring holograms remained intact. The results shown in Figure 19 prove that the recorded holograms within the recording medium can be selectively erased and replaced with other desired holograms. Therefore, it is possible to dynamically modify the patterns stored in the LHC with no need to refresh all of the stored patterns.

3.5.1 Broadening of Re-recorded Hologram

It is notable in Figure 19(c) that the diffracted signal from the middle hologram after re-recording appears wider compared to those of the six surrounding holograms. This is caused by the nonuniformity of the refractive index at the location of the middle slice after erasing by the UV and reference beams, which scatters the reference beam in the re-recording step. This effect has been investigated by illuminating the reference beam over a clean area of the recording crystal and over a slice having an erased hologram. The hologram was erased by illuminating the slice with the UV beam and the reference beam for 20 minutes. Figure 20 shows the intensity profile of the reference beam at the exit facet of the crystal indicated in Figure 15. The full width at half maximum (FWHM) of the beam profile at the erased hologram is about twice as much as that of the beam at the clean area, which is caused by the refractive index nonuniformity.

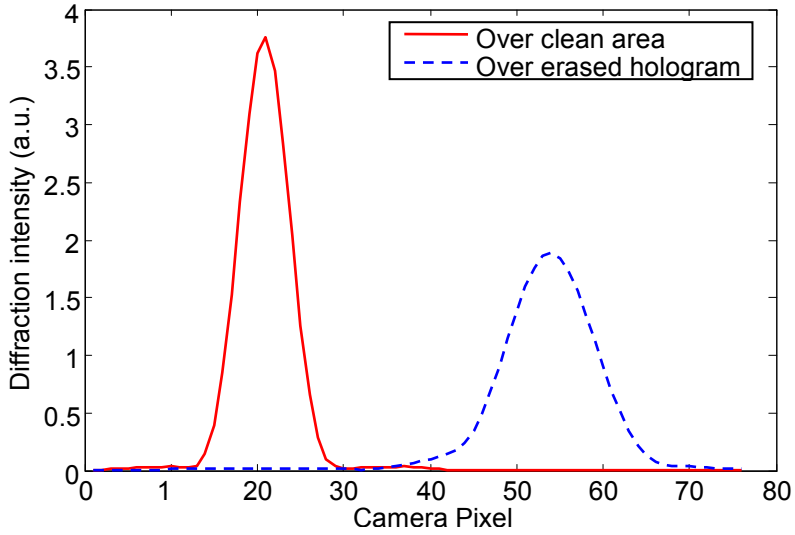

Figure 20. Broadening of the reference beam profile passing through an erased slice. The intensity profile of the reference beam is shown. The reference beam is illuminated over a clean area (solid) and over an erased hologram (dashed).

Figure 21 is an illustrated explanation of how the erasure by the UV and green beams results in the refractive index nonuniformity. This nonuniformity occurs because of the localized sensitizing of the slice with the UV beam having a thin Gaussian-shaped field profile. This gives rise to a nonzero gradient of the electron concentration in the conduction band [Figure 21(a)]. The excess of the electron concentration in the conduction band at the peak of the UV beam is migrated to the surrounding regions. The migration mechanisms are bulk photovoltaic effect [18], the dominant charge migration process in $LiNbO_3$ crystals, and diffusion, which has a small contribution. The migrated electrons are then recombined mostly at the empty Fe centers and at a much smaller rate at the mostly filled Mn centers within the $LiNbO_3$ bandgap [Figure 21(b)]. This charge migration produces a nonuniform charge distribution, thus a nonzero electric field pattern, which in turn results in the refractive index nonuniformity through electro-optic effect [29].

The charge migration continues until the built-up electric field due to the charge migration reaches its saturation value, which results in the equilibrium state of the space charge pattern. As a result of the photovoltaic effect being the dominant charge migration mechanism, the electrons move mostly to the *c*-axis direction. Therefore, the space-charge pattern and the resulting refractive index pattern are asymmetric. Carefully looking at Figure 19(b) one can see the deviation of the diffraction from the re-recorded hologram in the middle of the other holograms, which is a result of the asymmetric refractive index pattern.

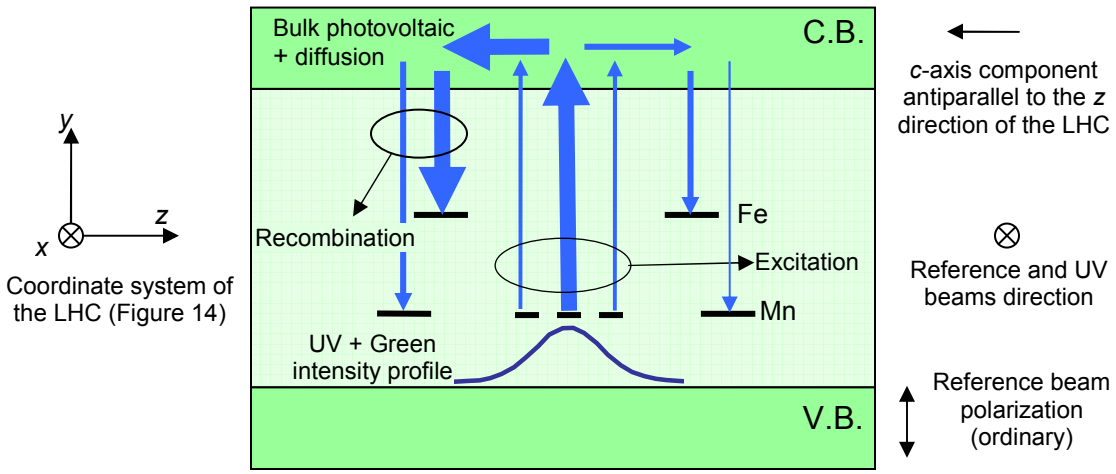

(a)

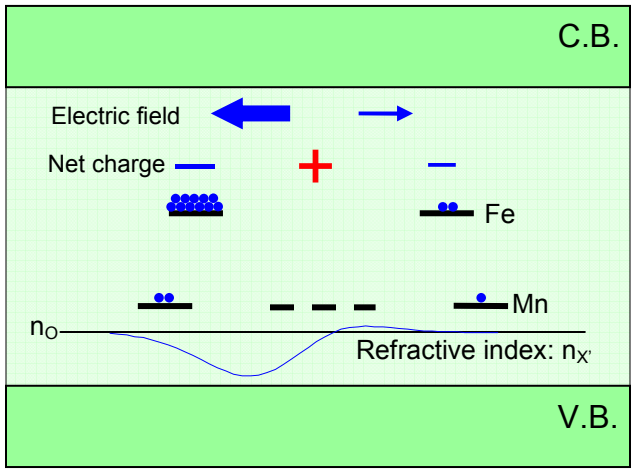

(b)

Figure 21. Explanation of the nonuniformity of the refractive index within an erased slice. The band structure of the $LiNbO_3$:Fe:Mn and the excitation and recombination of the electrons are shown. (a) The UV and reference beams with Gaussian field profiles are illuminated to erase a localized hologram in a slice. (b) The charge migration produces index nonuniformity. C.B.: Conduction band. V.B.: Valence band.

3.5.2 Solution to Broadening Effect

To have a clean area with uniform refractive index for recording another hologram in place of the erased one, it is required to redistribute the migrated charges so that the net charge over the volume of the slice and the surrounding regions is close to zero. Figure 22 shows how this post treatment of the erased slices is performed. A beam with wider field profile is needed that excites the electrons from the Fe centers to the conduction band in the surrounding regions, which trapped the migrated electrons during the erasure. The safe and suitable wavelength to be used for the post treatment can be of a red light, say from a He-Ne laser. The absorption cross section of the Mn centers at the red wavelength is negligible and therefore, the red light cannot affect the neighboring holograms. The UV beam is not suitable for this purpose because a wider UV beam will affect the neighbor slices and the holograms recorded in those slice will be degraded. For the same reason, the green beam is also eliminated as it causes partial erasure of the holograms as well.

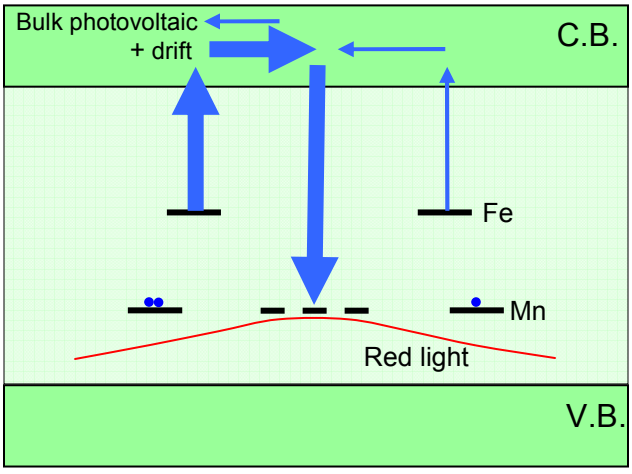

Figure 22. Post treatment of the erased slices by illuminating a red beam and redistribute the migrated charges during the erasure. C.B.: Conduction band. V.B.: Valence band.

When the electrons are excited to the conduction band, they are subject to drift by the locally induced electric filed, bulk photovoltaic effect, and diffusion. It should be noted that diffusion has a negligible contribution to the conduction band electron migration in $LiNbO_3$. Furthermore, a significant advantage of using the red wavelength is it shows a much weaker bulk photovoltaic effect compared to the UV beam. For example, the bulk photovoltaic coefficient for excitation of the electrons from the Fe centers to the conduction band at 404 nm (UV) wavelength is 19 times as that at 633 nm (red) wavelength [29,30]. Therefore, the electrons once excited to the conduction band, start to flow back to vanish the space-charge pattern, and most of them are eventually trapped in the Mn centers, where they had been initially excited. Fading of the local electric filed induced by the space-charge pattern smooths the refractive index distribution that cleans the slice for recording another hologram.

Figure 23 shows the effectiveness of the post treatment by the red beam in alleviating the broadening of the reference beam when passed through an erased slice. After erasing the hologram, the erased slice was illuminated by a red beam from a He-Ne laser emitting at 633 nm wavelength for 5 hours. The read beam was much bigger than the slice (about 1 mm compared to the size of the slice, 18 μm) and therefore, its intensity was practically uniform over the slice. The reason for selecting the red wavelength over the green wavelength is that illuminating with red beam does not results in partial loss of persistence as the green beam does, thus, the recorded holograms do not lose their strength. As shown in Figure 23, the intensity profile of the reference beam when illuminated over the bleached slice is not more than about 10% wider than that when

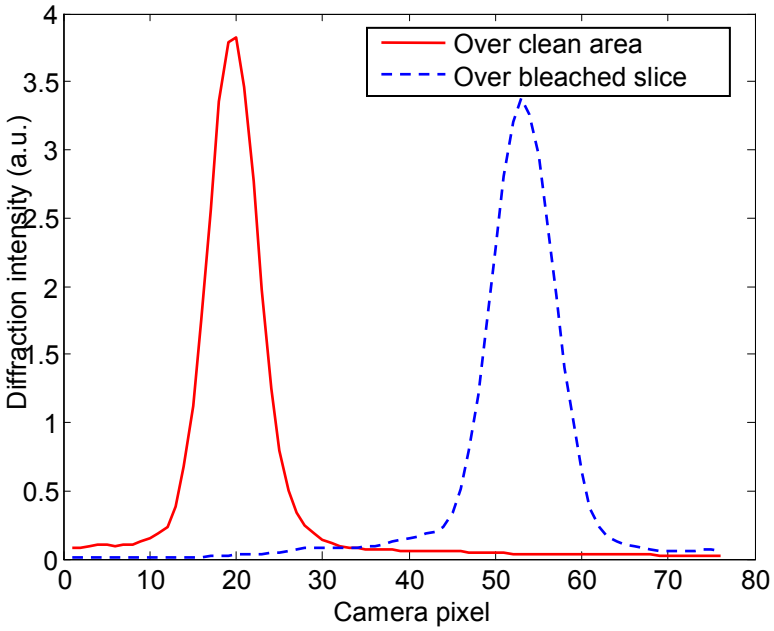

Figure 23. Alleviating the refractive broadening of the reference beam by illuminating a red beam (post treatment). The reference beam is illuminated over a clean area (solid) and over an erased hologram after bleaching the slice (dashed).

illuminated over a clean area. It can be inferred that illuminating the erased hologram with a uniform beam solves the widening problem.

3.6 Discussion

LHCs maintain good correlation performance with low crosstalk and acceptable shift-invariance. The main advantage of the LHCs is the dynamic recording and erasure of the holograms by having access to individual slices of the recording medium for recording and erasure. There are a few potential improvements for the LHC that can make these systems more practical and viable for real pattern recognition applications.

Compactness is another unique feature of the LHCs. The correlation signal, diffracting out of the recording medium, has a small area, which is the cross section of each slice. By attaching a detector array to the exit facet of the crystal the signal can be

collected from each slice and there is no need for a collecting lens and the spaces in front and behind it. This way, the system can be built in a more compact fashion. This capability is not present in the conventional optical correlators that work based on angular multiplexing.

The DC blocking filter in Figure 14 with the corresponding 4-f imaging system has the advantage that the filter at the Fourier plane of the 4-f system can be arbitrarily designed and replaced with the simple DC blocking filter for different applications. However, such a filtering system is quite lengthy, which makes the system large. Therefore, for regular correlation applications, where the DC blocking filter suffices the purpose of edge enhancement, the blocking filter can be simply placed on the front facet of the recording medium, which is designed to be the Fourier plane. Much space can be saved by eliminating the 4-f system. If the filters are made on thin peaces of transparent material, then they can be placed right in front of the recording medium and be replaceable. This requires shifting of the recording medium a little from the Fourier plane. It is shown that this shift has no effect on the correlation performance of the LHC.

The absorption cross section of the Fe centers at red wavelength is small compared to that at the green wavelength. Because of that, the post treatment can take a long time compared to the recording time. Shining the red beam over a large area makes its intensity even smaller, which slows down the process. By merging the red beam with the UV and reference beams and focusing it with the same cylindrical lens (CL1 in Figure 14) it is possible to intensify the red light at the erased slice. Still the red beam profile needs to be wider than the UV and reference beam profiles. That can be obtained by making the red beam in front of the cylindrical lens CL1 a little diverging rather than

perfectly collimated and shifting the focus of the red beam behind the focus of the UV and reference beams.

CHAPTER 4

PERFORMANCE ENHANCEMENT OF LHC

4.1 Introduction

As discussed in Chapter 2, the LH recording is suitable for the applications where less number of holograms and large diffraction efficiency is needed [36]. This provides a variety of opportunities along with some trade-offs to the applications sought for the LH recording. The higher diffraction efficiency property results in a higher signal to noise ratio (SNR) at the detector. However, the high diffraction efficiency provided by the LH recording can be much higher than the requirements for an optical correlator with acceptable false classification error rate. The SNR requirement is determined by the application and the type of the patterns under recognition. The goal of the work presented in this chapter is to utilize this large diffraction efficiency to significantly improve some of the performance measures of the LHC, while marinating acceptable diffraction efficiency of the holograms.

The in-plane shift invariance and the rotation invariance of the LHC are improved by multiplexing several holograms from shifted and rotated versions of one 2D pattern within the corresponding slice of the recording medium to that pattern. Theoretical study of the multiplexing procedure for the in-plane shifted pattern is presented and the trade-off between the enhanced shift invariance and the spatial frequency bandwidth of the correlated 2D patterns is explained. The experimental results of the shift and rotation invariance enhancement are demonstrated. The in-plane shift invariance of the LHC is improved by one order of magnitude. This improvement is carried out by multiplexing 20

holograms originated from 20 shifted versions of the 2D pattern under correlation in one slice of the recording medium. By the same method, the rotation invariance of the LHC is enhanced by one order of magnitude by multiplexing 12 holograms from 12 rotated versions of the same pattern. The trade-off between the final diffraction efficiency and the robustness enhancement is discussed.

In another effort to extend the capabilities of the LHC, the 2D LHC is transformed to a 3D object recognition system. A localized hologram of a 3D object has been recorded. The rotation invariance of the 3D LHC has been measured. The limitations of the LHC for 3D object recognition are investigated and the existing trade-offs are discussed.

4.2 Enhancement Mechanism

The large diffraction efficiency of the localized holograms in the LHC provides enough dynamic range to multiplex more than one hologram within the slices of the recording medium. By careful selection of the number of the multiplexed holograms, the diffraction efficiency of each multiplexed hologram remains above an acceptable level to recognize the examined patterns with adequate accuracy and low false classification rate. Thereby, multiple versions of a pattern can be recorded in the system. As a result, the range within which the correlated pattern can move and still be recognized is expanded, hence an optical correlation system more robust to the pattern deviations. It should be noted that the multiplexed holograms of an individual 2D pattern share the same volume of the recording medium and the same reference beam. However, different signal beams corresponding to different versions of the 2D pattern (i.e., shifted or rotated versions) are used for recording different holograms.

The volume holographic optical correlators are very selective to the linear shift of the examined 2D pattern in the plane of the reference and signal beams [47], referred to as the in-plane shift. This is true for the LHC as well, as shown theoretically and experimentally in Chapters 2 and 3, respectively, for the shift in the *x* direction in Figure 14. In Section 4.6 in this chapter, it will be experimentally shown that the out-of-plane and longitudinal shift invariance quantities (in the *y* and *z* directions in Figure 14, respectively) are more than one order of magnitude larger than the in-plane shift invariance [49]. Therefore, the concentration has been only on the improvement of the in-plane shift invariance.

One can observe that because of the in-plane linear shift selectivity, the volume holographic correlators are also selective to the rotation about the axis of the signal beam (*z*-axis in Figure 14 for the LHC). The reason is this rotation involves the in-plane linear shift of the 2D pattern for a significant portion of the pattern area around the axis perpendicular to the in-plane shift direction (*y*-axis in Figure 14 for the LHC). Figure 24 shows where on the 2D pattern the in-plane linear shift component is dominated when the examined 2D pattern is rotated about the *z*-axis. For a specific rotation angle, the linear shift is larger for the points on the 2D pattern with larger rotation radius, resulting in a more severe Bragg mismatch. Therefore, larger patterns are generally expected to show smaller rotation invariance. Hereinafter in this chapter, the term "shift" will imply the in-plane linear shift unless otherwise specified. Also, "rotation" will imply the rotation about the z-axis.

The idea is to multiplex several holograms within the volume of the corresponding slice from one pattern, which is shifted along the *x*-axis for each recording.

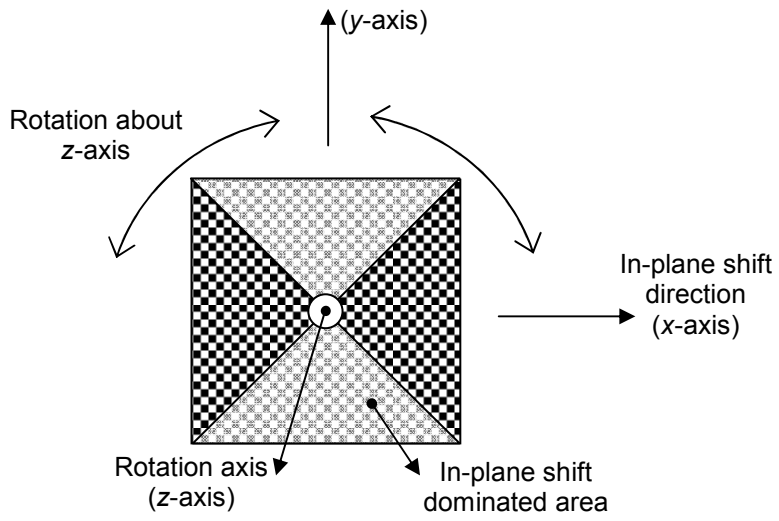

Figure 24. Rotation of the 2D pattern about the *z*-axis in Figure 14. The regions of the 2D pattern within which the in-plane linear shift component (i.e., shift in the *x* direction in Figure 14) are indicated as brighter regions.

For all the multiplexed holograms, the reference and UV beams remain intact, illuminating the same slice with the same angle, 90 degrees with respect to the signal beam, throughout each recording. During the correlation, the signal beam from the same pattern as that used during the recording reads all the multiplexed holograms. If the reading pattern is positioned within the shift invariance range due to any of the shifted versions of the recorded pattern, the correlation output signal is diffracted from the corresponding multiplexed holograms. The reason is those holograms have the closest Bragg matching condition with the reading beam. The more the multiplexed holograms, the larger the possibility of Bragg matching will be, hence larger shift invariance. By the same method, several holograms due to the rotated versions of the same pattern are multiplexed within once slice of the recording medium, whereby the rotation invariance of the LHC is enhanced.

In volume multiplexing of the holograms, the diffraction efficiencies of the multiplexed holograms are degraded rapidly by increasing the number of the multiplexed holograms at the same material volume. In Section 2.4.3 in Chapter 2, it was quantitatively discussed that the diffraction efficiency varies inversely proportional to the square of the number of holograms multiplexed within the volume of a slice of a photorefractive crystal [13]. Therefore, the number of multiplexed holograms cannot be increased arbitrarily and there is a trade-off between the shift/rotation invariance improvement and the final diffraction efficiency of the holograms.

To achieve a relatively uniform shift/rotation invariance curve for the shift/rotation invariance improved LHC, it is required to follow and accurate recording time schedule for the multiplexing. The recording times are derived from the recording and erasure dynamics of the holograms to obtain reasonably identical strengths for the multiplexed holograms [46].

4.3 Theoretical Study

The diffracted beams from the multiplexed holograms will propagate at the same direction because the holograms are all recorded with the exact same reference beam, as mentioned in Section 4.2. Thus, the correlation output signal at the detector is the superposition of the diffracted beams. Because the diffracted beams are produced by the same signal beam at the same time, they are coherent. As a result, the phases of the diffraction beams at the detector are involved in determining the resultant output signal. Therefore, it becomes necessary to study the behavior of the phase of the diffracted beam versus the linear shift of the pattern.

4.3.1 Phase Variation in Shifted Configuration

For one recorded hologram in a slice of the recording medium, the variations of the amplitude and phase of the diffracted beam versus the shift of the pattern have been simulated using Equation (12) and the results are shown in Figure 25. In all the simulations in this chapter the focal length of the Fourier transform lens F is 10 cm, the wavelength λ is 532 nm, the crystal height L_X is 1.6 mm, the ordinary refractive index n is2.3, and the selected slice of the recoding medium is at the focus of the lens ($Z_C = 0$, Figure 7). The shifted configuration is used for the position of the crystal entrance facet versus the Fourier transform pattern (Section 2.3.1 in Chapter 2), by which, one half of the Fourier transform of the 2D pattern, taken by the Fourier transform lens, enters the crystal. Thereby, with the limited height of the crystal (L_X in Figure 7) the largest spatial frequency bandwidth for the LHC is achieved. The half width of the main lobe of the sinc function at the first nulls is 34 μm, which is by definition the shift invariance of the correlation system.

As shown in Figure 25(b), the phase of the diffracted beam varies quite rapidly with respect to the in-plane pattern shift. The discontinuities on the phase curve occur because the phase values are bounded between -90º and +90º. The rapid variations come from the first exp(.) multiplier in Equation (8) that appears because of the shifted configuration. By eliminating this exp(.) multiplier using the symmetric configuration (Section 2.3.1 in Chapter 2), the phase variations is be greatly reduced.

The main effect of such phase variation is that the diffracted signals corresponding to two or more multiplexed holograms will add up constrictively or destructively because they are coherent. This effect can be easily observed in Figure 26,

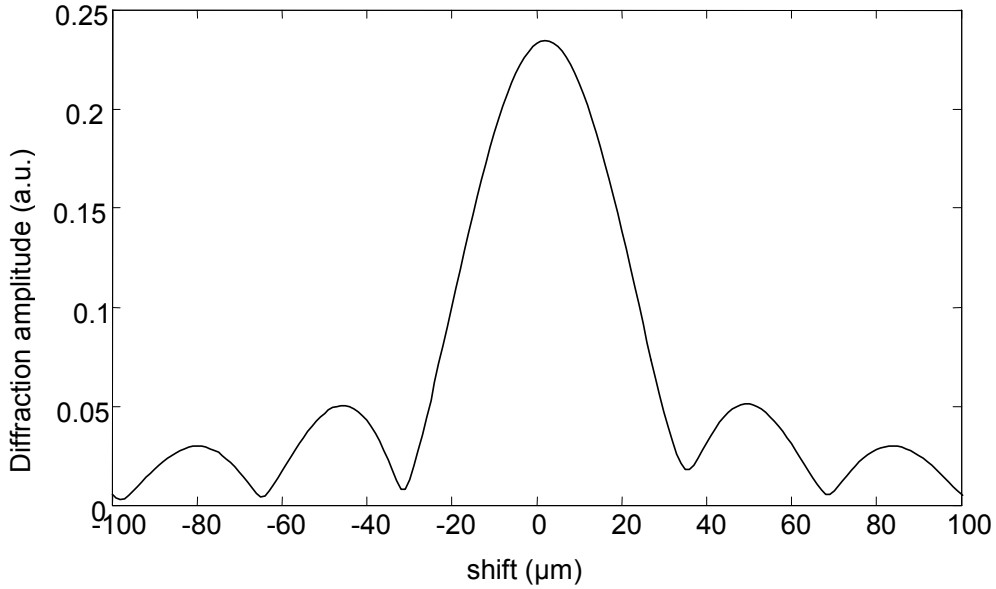

(a)

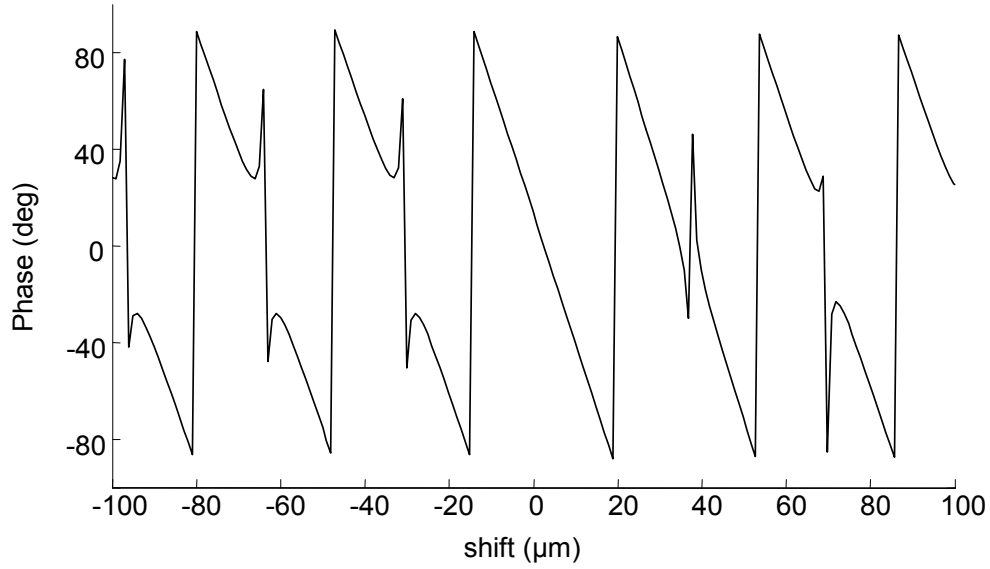

(b)

Figure 25. (a) Simulation of the amplitude variation of the diffraction field versus in-plane pattern shift. The amplitude curve resembles the amplitude of a sinc function. The half width of the main lobe of the sinc function at the first nulls is 34 μm. (b) Simulation of the phase variation of the diffraction field versus in-plane pattern shift. The discontinuities on the phase curve occur because the phase values are bounded between -90º and +90º. The simulation parameters as indicated in Figure 7 are F = 10 cm, λ = 532 nm, L_X is 1.6 mm, n = 2.3, and Z_C = 0. The shifted configuration is used for the position of the crystal entrance facet versus the Fourier transform pattern (Section 2.3.1 in Chapter 2).

where two simulated curves for two holograms are depicted for the diffraction power variation versus the in-plane shift of the reading pattern. The two holograms are recorded by the same pattern shifted by the value of the shift selectivity, 34 μm, between the two recordings. This means recording one pattern at the null of the shift selectivity curve of the other pattern. Although it might be expected that the superposition of the two curves makes a rather uniform curve, it has a deep valley at the center of the two peaks (shown by dashed-dotted curve). The reason is the diffraction fields from the two holograms have close to 180º phase difference when the reading pattern is shifted halfway between its original positions during the recording the two holograms, thus, they are destructively superimposed. This can be further verified from Figure 25(b), considering that the

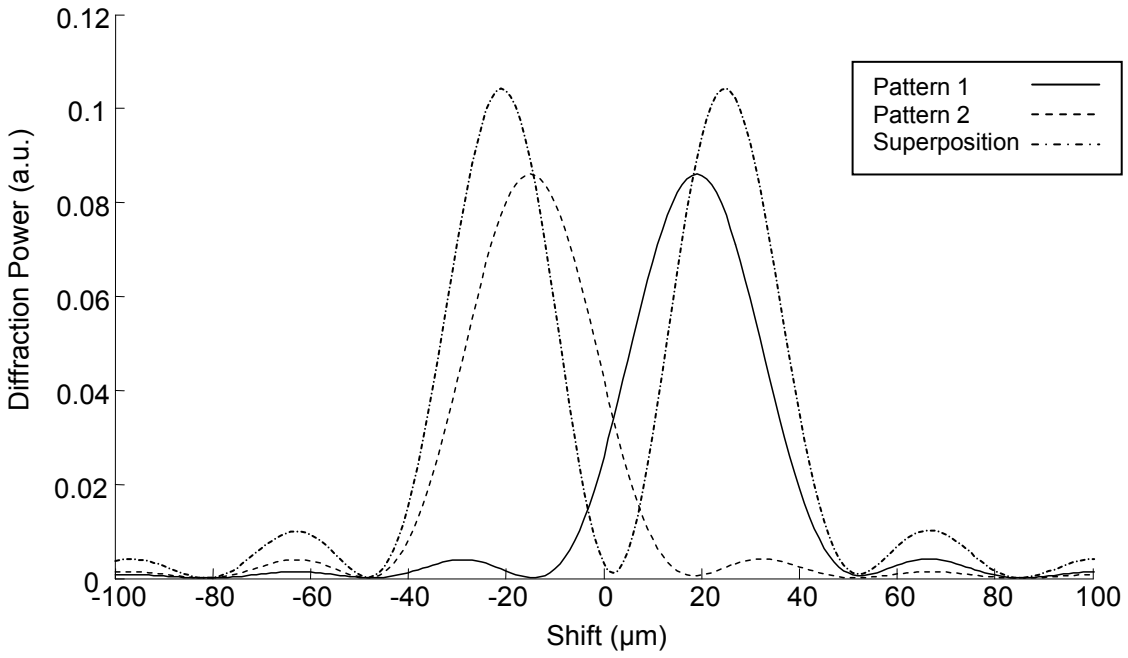

Figure 26. Simulation of the superposition of the diffraction from two multiplexed holograms in shifted configuration. The diffraction power curves from two individual holograms originated from two shifted versions of the same 2D pattern are sketched. The pattern is shifted by 34 μm between the two recordings. The diffraction power curve for the coherent superposition of the two diffracted beams is depicted. The conditions of the simulation are the same used for Figure 25.

halfway pattern shifts with respect to the two holograms have opposite signs (i.e., shift to the left for one hologram and to the right for the other). It is implied that to obtain a uniform superposition for the shifted configuration, the patterns have to be shifted for less than the shift invariance value.

4.3.2 Flat Enhanced Shift Invariance Profile in Shifted Configuration

Because the shifted configuration results in larger spatial frequency bandwidth of the LHC, the possibility of obtaining a flat shift invariance curve for the shift invariance enhancement in this configuration is studied. To generate a superposition curve for the shift invariance that is wide, uniform, and strong at the same time, the values for the relative shift of the multiplexed patterns and the relative strengths of the corresponding holograms have been selected through a trial and error process. The simulation has been run for multiplexing 10 holograms and the results are shown in Figure 27. The pattern shift has been selected to be 22 μm. This is considerably smaller than the shift invariance for individual patterns (i.e., 34 μm). Nonetheless, multiplexing of the holograms results in a significantly wider shift invariance curve than the curve for an individual hologram. Also, the curve is relatively uniform in the middle and has enough strength for the detection. As shown with different dotted curves in Figure 27, it is necessary to modify the strengths of the multiplexed holograms to obtain a uniform curve.

In Figure 27, it is observed that the two holograms at the two ends of the shift range have the least strengths versus the ones in the middle. The reason is the overlapping curves are added destructively and reduce the superposition power. The two holograms at the ends of the range would generate two large peaks on the superposition curve if they

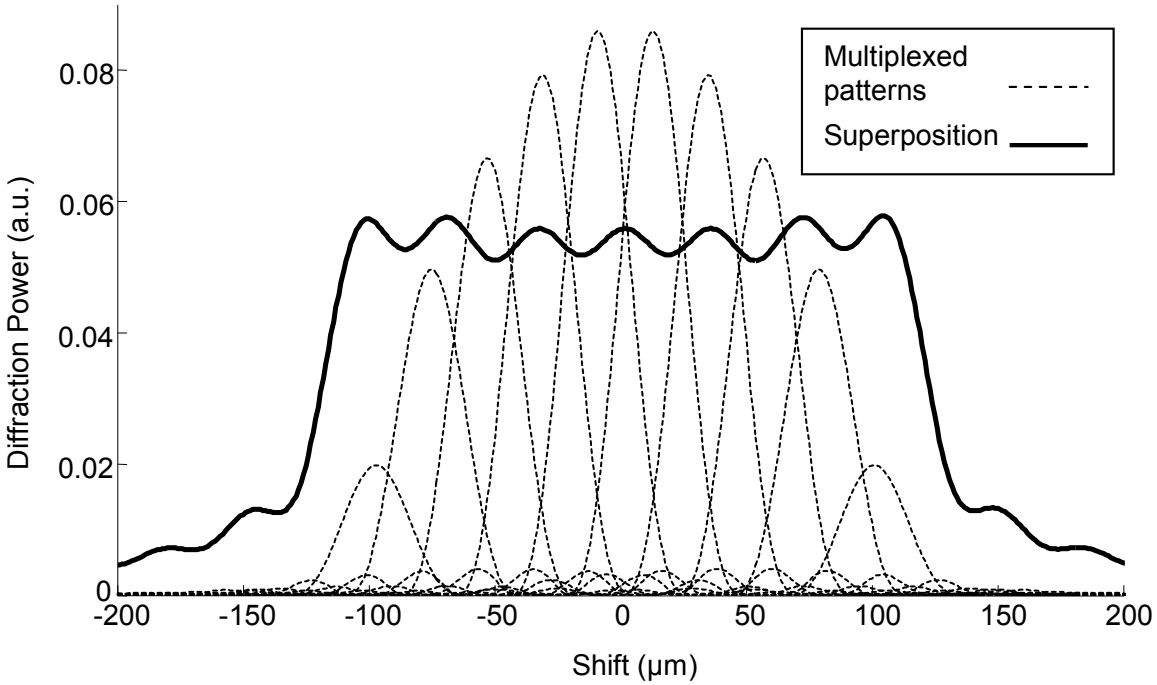

Figure 27. Simulated diffraction power versus in-plane pattern shift from 10 holograms originated from 10 shifted versions of the same 2D pattern (solid). The shift invariance curves due to each pattern shift are depicted as the dashed curves. The pattern has been shifted by 22 μm between consequent re recordings. The holograms have different strengths. The diffraction power of the superposition of the beams is depicted as well (solid curve). The relative strengths (i.e., the square root of the diffraction efficiency for small diffraction efficiencies) of the holograms from left to right have been 0.6, 0.95, 1.1, 1.2, 1.25, 1.25, 1.2, 1.1, 0.95, and 0.6.

had the same strengths as the middle holograms, because their diffractions suffer much less from destructive overlap from surrounding holograms.

4.4 Experimental Setup

Figure 28 is a schematic illustration of the LHC experimental setup with the added capability of the in-plane linear pattern shift and rotation about the *z*-axis. A mask, which has the 2D pattern on it, is placed on a rotation stage and a shift stage. The pattern on the mask is a 450 × 450 array of black and white (fully opaque or transparent) square pixels

randomly distributed. The pixel size is 28 μm × 28 μm. The same mask is used for the recoding and reading. Both the rotation and shift stages are computer controlled by closed loop DC servo actuators. The recording medium is the same as the one used in the setup in Chapter 3, a 45-degree-cut congruently grown $LiNbO_3$:Fe:Mn crystal doped with 0.15 wt% $Fe2O_3$ and 0.02 wt% MnO. The crystal width L_X is 1.6 mm. The focal lengths of the lenses are mentioned in the caption of Figure 28. The entrance facet of the crystal is placed at the Fourier plane of lens F3. In all of the presented experiments in this section, the intensities of the recording reference and signal beams and that of the UV beam are 150 mW/cm^2, 150 mW/cm^2, and 80 mW/cm^2, respectively. The rest of the components in the system and their functions are the same as explained in Section 3.2 in Chapter 3.

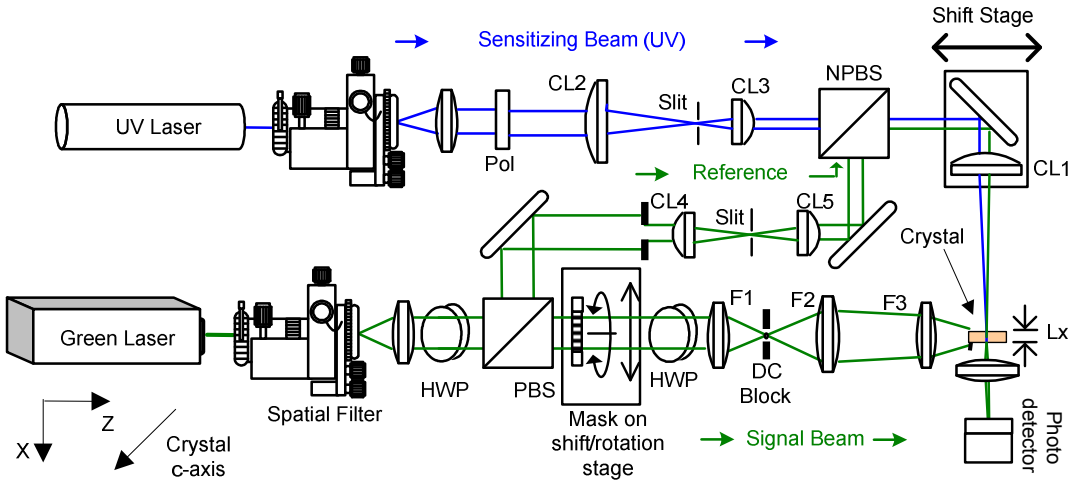

Figure 28. LHC experimental setup with the recorded pattern (mask) on a shift and rotation stage. The recording medium is a 45-degree-cut congruently grown $LiNbO_3$:Fe:Mn crystal doped with 0.15 wt% Fe_2O_3 and 0.02 wt% MnO. The thickness L_X is 1.6 mm. HWP: half-wave plate, PBS: polarizing beamsplitter, NPBS: non-polarizing beamsplitter, F1, F2, and F3: Fourier transform lens, CL: cylindrical lens, Pol: polarizer. Lens focal lengths: f_1 = 20 cm, f_2 = 25 cm, f_3 = 10 cm, f_{CL1} = 5 cm.

4.5 Calculation of Recoding Time Schedule for Multiplexing

Before the multiplexing, it is required to measure the recording and erasure time constants of the LHC, based on which, the recording times for each hologram in the multiplexing sequence is calculated. This requirement is because the multiplexed holograms overlap in the slice volume of the crystal, therefore, recording each hologram results in the erasure of the previously recorded holograms [46]. Whereas in localized holography for recording one hologram per slice, there is no need for a recording time schedule since the holograms are not affected by each other [34].

4.5.1 Derivation of Equation for Recording Time Calculation

The hologram strength (the refractive index modulation) is proportional to the square root of the diffraction efficiency for small hologram strengths. In two-center recording in doubly doped $LiNbO_3$:Fe:Mn, the hologram strength is approximated by exponential functions of time for the recording and erasure [46]. For the recording phase, the increase of the hologram strength is approximated by a monoexponential function of time:

$$\sqrt{\eta} = A_0\left[1 - \exp\left(-t/\tau_r\right)\right], \tag{14}$$

where A_0 is the saturation hologram strength and τ_r is the recording time constant. The proportionality constant of the hologram strength is omitted for simplicity.

In the monoexponential approximation for the recording phase, it is assumed that the space charge pattern in both the Fe and Mn centers are built up with the same time constant τ_r. This assumption is valid when only the electrons in the Fe centers contribute to the recording, which is true for longer recording wavelengths (e.g., 633 nm from a He-Ne laser) with smaller photon energy. For shorter recording wavelengths (e.g., 532 nm

from a diode-pumped solid state laser), the recording is partially contributed by the electrons in the Mn centers as well, therefore, the governing equation for the hologram strength can be more complicated. Taking that fact into account, the monoexponential approximation is used for the recording time calculations and the results are used as the initial speculation for the recording times in the experiments. The fine tuning of the time schedule is obtained by trial and error using the experimental data.

For the erasure phase, the decrease of the hologram strength is approximated by a biexponential function of time [46]:

$$\sqrt{\eta} = A\exp\left(-t/\tau_{e1}\right) + B\exp\left(-t/\tau_{e2}\right), \tag{15}$$

where τ_{e1} and τ_{e2} are the short and long erasure time constants, respectively, and $A + B$ is the hologram strength before the erasure starts. If the hologram has been recorded to the saturation, then $A + B = A_0$. The biexponential fashion of the erasure comes from the fact that in two-center recording the space charge pattern is imprinted in two sets of Fe and Mn centers. The erasure is performed by illuminating both the recording beams and the sensitizing beam. Therefore, the electron population in the Fe centers is reduced faster than that in the Mn centers because of the different absorption cross sections of the Fe and Mn centers at different wavelengths [29,30]. In fact, the absorption cross section of the Mn centers at the recording beam wavelength is very small compared to that at the sensitizing beam (e.g., it is zero at 633 nm [29]). It is inferred that the long time constant τ_{e2} is solely due to the erasure of the space charge pattern in the Mn centers.

It should be noted that the space charge pattern in the Fe centers is eventually erased and transferred to the Mn centers after the readout of the multiplexed holograms for a time period a few times larger than τ_{e1}. Hence, for the calculation of the recording

time schedule it is possible to simply consider the portion of the space charge pattern in the Mn centers that grows during the recording and decays during the erasure [46]. Thereby, Equations (14) and (15) are modified, so only the fraction of the hologram strength due to the space charge pattern in the Mn centers is taken into account in those equations. Applying the modification to Equation (14) yields

$$\beta\sqrt{\eta} = \beta A_0 \{1 - \exp[-(t - T)/\tau_r]\}, \tag{16}$$

where β is the ratio of the hologram strength due to the space charge pattern in the Mn centers to the entire hologram strength. The constant T is added as for the recording start point of the consecutively recorded holograms during the multiplexing.

Modifying Equation (15) results in omitting its first term corresponding to the erasure of the Fe space charge pattern. The second term with the long erasure time constant τ_{e2} is retained, which corresponds to the erasure of the Mn space charge pattern:

$$\beta\sqrt{\eta} = B\exp(-t/\tau_{e2}), \tag{17}$$

where β is the same as that used in Equation (16) and has the exact same definition. The constant B is the hologram strength due to the Mn space charge pattern immediately after the recording. The monoexponential Equation (17) accurately governs the slow erasure of all of the multiplexed holograms regardless of their recording start times [13,46].

For the recording time schedule calculation, Equations (16) and (17) are simultaneously solved for each of the multiplexed holograms with different recording start points during the multiplexing [13]. The resulting transcendent Equation (18) is incrementally solved for t to find the recording times t_n ($n = 2, 3, \ldots, N$; for N multiplexed holograms):

$$1-\exp\left[-\left(t-T_{n-1}\right)/\tau_r\right]=C_n\exp\left(-t/\tau_{e2}\right), \tag{18}$$

$$T_1=0,\ T_{n>1}=\sum_{i=2}^{n}t_i\ , \tag{19}$$

$$t_n=t-T_{n-1}\,. \tag{20}$$

It is assumed that the first hologram, recorded for $t_1 >> \tau_r$ reaches the saturation strength. The constant C_n is added to arbitrarily determine the relative final strength of the nth multiplexed hologram with respect to the strength of the first hologram. By manipulating the constant C_n it is possible to generate every profile shape for the improved shift invariance curve. It is notable that to obtain the desired strengths for the multiplexed holograms, they need to be read or erased for a period a few times larger than τ_{e1} to have the space charge pattern in the Fe centers completely erased.

4.5.2 Experimental Procedure and Results

The experiment for recording and erasure time constant measurements has been conducted as follows:

1- Pre-sensitizing - A hologram was recorded with the pattern shifted far from the initial pattern location for 5 minutes (Bragg mismatch recording). This was for bringing the recording initial condition to equilibrium, in terms of the electron populations in Fe and Mn centers.

2- Recording – The pattern was shifted back to its initial location. The principal hologram was recorded for 20 minutes and its diffraction power was measured every two minutes.

3- Erasure - The hologram was erased for 40 minutes by recording two holograms in the same slice by shifting the pattern back and forth from its initial location by ±30 μm (Bragg mismatch erasure). Every two minutes, the diffraction power of the principal hologram was measured with the pattern at its initial location and then the pattern was shifted and the mismatch hologram was recorded for two minutes. This way the same condition as in real multiplexing experiment was imitated.

The results of the measurements are shown in Figure 29. The small fluctuations of the curve during the erasure are because of the Bragg mismatch erasure that requires the 2D pattern on the shift stage to move back and forth. This way, the backlash of the shift stage motion results in a limited deviation when the 2D pattern is shifted back to its initial position for the Bragg matched monitoring of the diffraction power.

A monoexponential curve and a biexponential curve have been fitted to the data for the recording and erasure phases, respectively. The time constant of the fitted curve for the recording phase is $\tau_r = 6.78$ min. The short and long time constants of the fitted curve for the erasure phase are $\tau_{e1} = 3.38$ min and $\tau_{e2} = 25.34$ min, respectively.

Plugging the time constants of the fitted curves into Equation (18), the equation is solved incrementally for the consequent recording times. For multiplexing 20 holograms with the first hologram recorded to saturation, the calculated recording times for the 2nd hologram to the 20th hologram ranges from 8.5 minutes to 1.1 minutes. In these calculations, the same strength for all the multiplexed holograms is considered (i.e., $C_n = 1$ for every n).

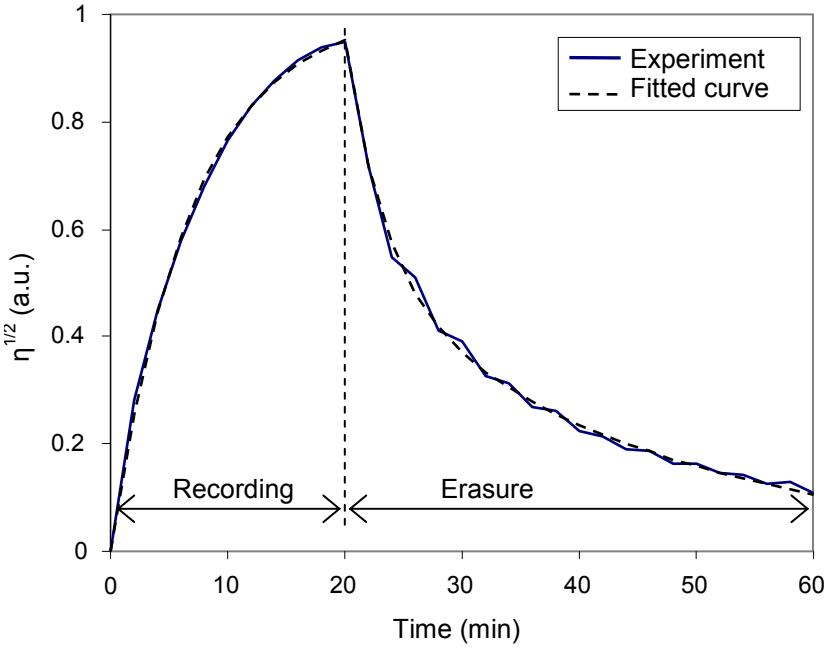

Figure 29. Recording and erasure of a localized hologram. The erasure has been performed by recording Bragg mismatch holograms in the same slice. The recorded pattern for the Bragg mismatch holograms has been shifted by 30 μm. The recording time constant of the fitted curve is τ_r = 6.78 min. The short and long erasure time constants are τ_{e1} = 3.38 min and τ_{e2} = 25.34 min, respectively. The diffraction power has been measured every two minutes. The intensities of the recording reference and signal beams and that of the UV beam are 150 mW/cm^2, 150 mW/cm^2, and 80 mW/cm^2, respectively.

4.6 Preliminary Experimental Results of Multiplexing

Before the multiplexing of the holograms, the actual shift invariance of an individual hologram recorded in one slice of the recording medium has been measured. This initial measurement provides a basis for the determination of the shift of the pattern during the multiplexing. The measurement results are shown in Figure 30. The shift invariance from the peak to the first minimum of the curve is ±35 μm to the both sides of the peak. This definition of the shift invariance resembles the definition given in Section 2.4.2 in

Chapter 2 for the shift invariance except that the diffraction power does not reach exact zero in practice.

The out-of-plane and longitudinal shift invariance values in the *y* and *z* directions in Figure 28, respectively, are measured as well for an individual localized hologram recorded in one slice. Figure 31 illustrates the diffraction power variation versus the out-of-plane shift of the reading 2D pattern. The out-of-plane shift invariance is about ±800 μm at -11 dB signal attenuation, which is more than an order of magnitude larger than the in-plane shift invariance. In Figure 32, the longitudinal shift selectivity is shown. The longitudinal shift invariance is about ±5 mm at -7.5 dB signal attenuation, which is more than two orders of magnitude larger than the in-plane shift invariance. Because the out-

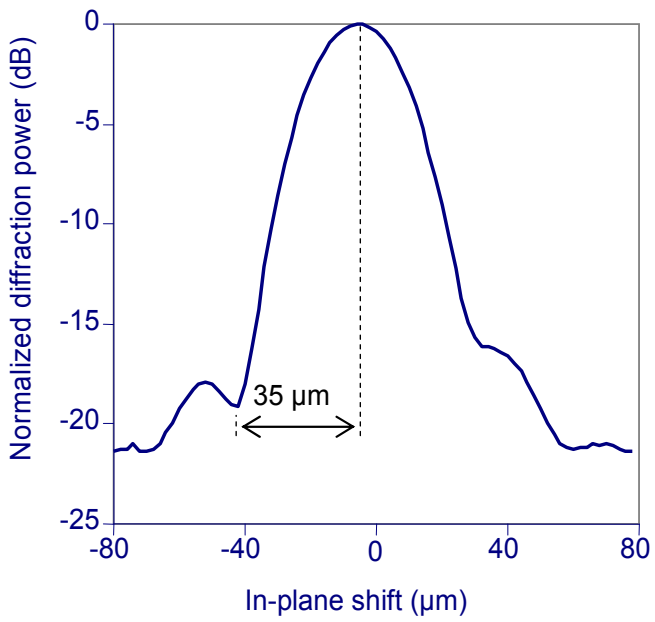

Figure 30. Shift selectivity of one localized hologram recorded in one slice. The horizontal axis represents the actual in-plane shift of the 2D pattern during the diffraction power measurement. The diffraction power values are normalized to the peak value. The shift invariance from the peak to the first minimum of the curve is 35 μm.

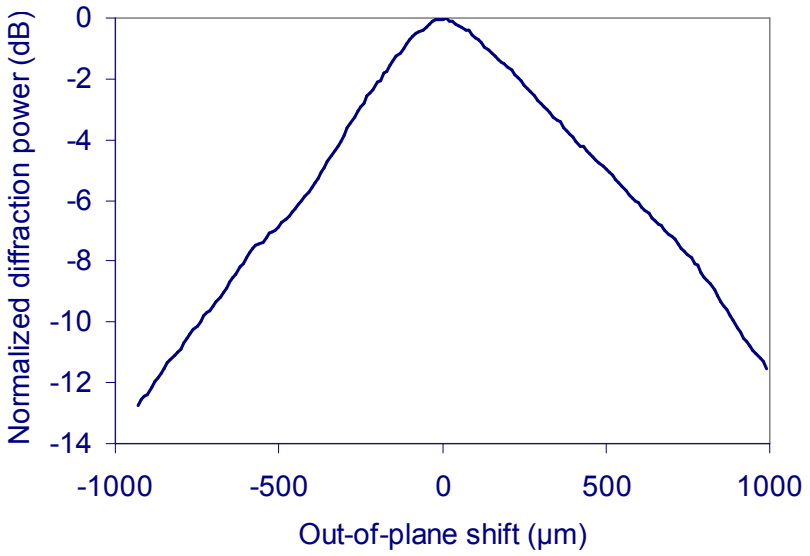

Figure 31. Out-of-plane (in the *y*-direction in Figure 28) shift selectivity of one localized hologram recorded in one slice. The recording and reading patterns are the same. The power values are normalized to the power value at the peak. The out-of-plane shift invariance is about ±800 μm at -11 dB signal attenuation.

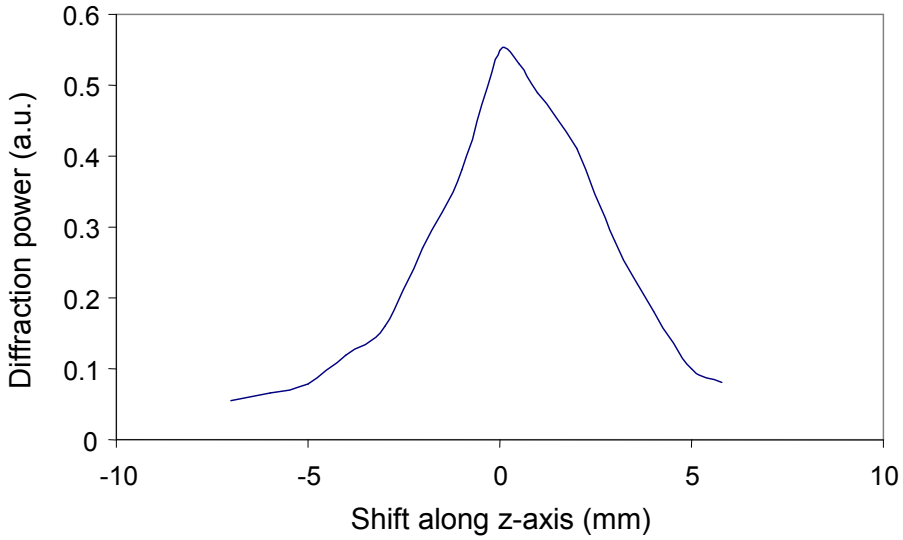

Figure 32. Longitudinal (in the *z*-direction in Figure 28) shift selectivity of one localized hologram recorded in one slice. The recording and reading patterns are the same. The longitudinal shift invariance is about ±5 mm at -7.5 dB signal attenuation.

of-plane and longitudinal shift invariance values are much larger than the in-plane shift invariance, the focus has been on the improvement of the in-plane shift invariance.

4.6.1 Multiplexing Using Initial Schedule Calculation

Using the recording times calculated in Section 4.5.2, 20 holograms have been multiplexed in one slice of the recording medium. For the multiplexing, the 2D pattern has been shifted by 32 μm between each two recordings. The shifted configuration has been used during the recordings.[1] During the readout, the reading pattern (same as the recording pattern) has been shifted and the diffraction power has been measured for each location of the pattern. The results are shown in Figure 33(a). The holograms have then been erased by recording a Bragg mismatch hologram in the same slice for 30 minutes, with the 2D pattern shifted far from the pattern shift range during the multiplexing. As mentioned in Section 4.5.1, the erasure after the multiplexing is performed to reach the final strengths of the holograms after the erasure of the space charge pattern in the Fe centers. The readout results after the erasure are shown in Figure 33(b).

In Figure 33(b), it is noted that the diffraction power values from the holograms excluding from the ones with the corresponding pattern location on the two ends of the shift range, are considerably below expectation. As mentioned in Section 4.3.1, in recording using the shifted configuration the diffraction fields from the multiplexed holograms can destructively add up because of the phase variation of the diffracted field with the reading pattern shift. This effect is expected to be significant when the pattern

[1] Refer to Section 2.3.1 in Chapter 2 for the shifted and symmetric configurations.

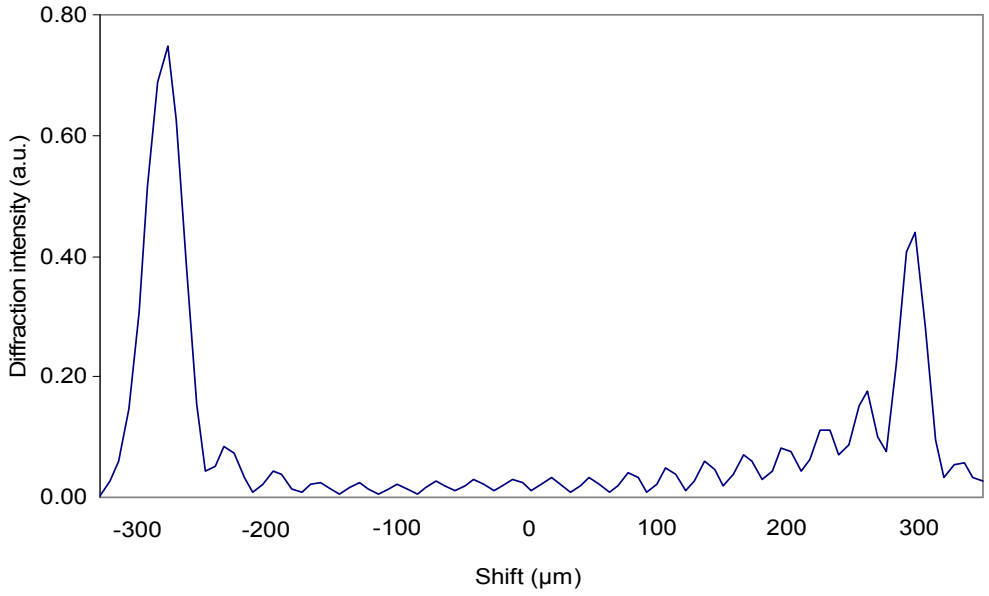

(a)

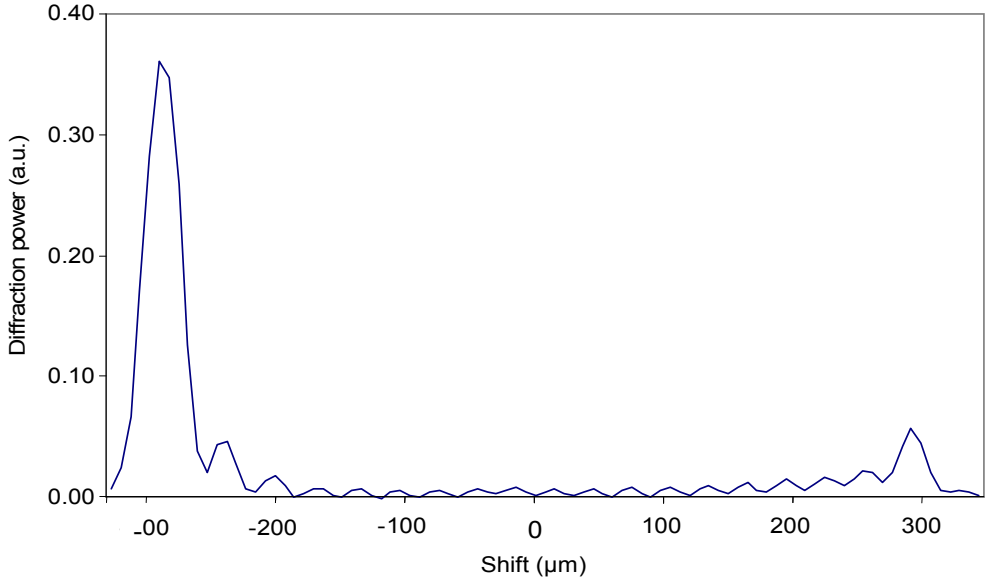

(b)

Figure 33. Diffraction power from 20 multiplexed holograms in one slice. The shifted configuration has been used during the recordings.[1] For the multiplexing, the pattern has been shifted by 32 µm between each two recordings. The reading pattern (same as the recording pattern) has been shifted and the diffraction power has been measured for each location of the pattern. The first peak on the left corresponds to the first recorded hologram. (a) Reading before erasure. (b) Reading after 30 minutes of Bragg mismatch erasure.

[1] Refer to Section 2.3.1 in Chapter 2 for the shifted and symmetric configurations.

shift between each two recordings is comparable to the shift invariance of a single hologram.

Moreover, the diffraction power at the leftmost peak corresponding to the first recorded hologram is larger than the diffraction power at the rightmost peak corresponding to the last recorded hologram. C. Moser *et al.* demonstrated the relationship between the persistence (β^2) of the localized holograms recorded in a doubly doped $LiNbO_3$:Fe:Mn crystal with their recording times [48]. The persistence is defined as the ratio between the diffraction efficiency of the hologram when adequately readout to the highest diffraction efficiency at the end of the recording. They showed that the persistence is increased when the hologram is recorded for a longer time using a green laser (λ = 532 nm) for the recording with a UV laser beam (λ = 401 nm) present. This complies with the expectation for a more complicated model for the recording at λ = 532 nm versus recording at λ = 633 nm as mentioned in Section 4.5.1. Considering the simple monoexponential model, the larger persistence for longer recording time implies a larger effective recording time constant for the portion of the space charge pattern that is erased with longer time constant. This larger effective recording time constant, rather than the recording time constant extracted from the recording curve in Figure 29, should be used to calculate the recording times of the multiplexed holograms.

4.6.2 Verification of Shifted Configuration Effect

The destructive superposition effect of the diffraction fields in shifted configuration has been further verified in this section. In two separate multiplexing experiments, 20 holograms have been multiplexed in one slice of the recording medium with the pattern

shift of 32 μm and 120 μm between each two recordings. The recording time schedules for the two experiments have been exactly the same.

To reach a more uniform diffraction efficiency distribution for the multiplexed holograms compared to the multiplexing results presented in Section 0, Equation (18) has been solved with the recording time constant τ_r twice the value found in Section 4.5.2 ($\tau_r = 2 \times 6.78 = 13.56$ min). The long erasure time has been unchanged ($\tau_{e2} = 25.34$ min). The same strength for all the multiplexed holograms is considered (i.e., $C_n = 1$ for every n). For multiplexing 20 holograms with the first hologram recorded to saturation, the calculated recording times for the 2nd hologram to the 20th hologram ranges from 12.6 minutes to 1.2 minutes. The holograms have then been erased by recording a Bragg mismatch hologram in the same slice for 30 minutes, with the 2D pattern shifted far from the pattern shift range during the multiplexing.

The readout results after the erasure are shown in Figure 34. The 32 μm shift is comparable to the shift invariance of one hologram (35 μm as seen in Figure 30) while the 120 μm shift is much larger than the shift invariance. Comparing the charts (a) and (b) in Figure 34 for the 32 μm and the 120 μm pattern shifts, respectively, it is clear that when the pattern shift is comparable to the shift invariance, the destructive superposition effect is much stronger. In Figure 34(a), one can observe that the peaks in the middle of the pattern shift range are much weaker than those on the two ends of the pattern shift range. Whereas when the pattern shift is much larger than the shift invariance, the diffraction fields from the consecutively recorded holograms have almost no effect on each other. As seen in Figure 34(b), the middle peaks are comparable with the two end peaks and have suffered much less destructive superposition. The difference is because

when each hologram is read at its Bragg matched condition (i.e., the reading pattern being at the exact position where it was during the recording of that hologram), the total Bragg mismatch condition occurs for all the other multiplexed holograms. Therefore, the destructive contribution due to the diffraction from the other holograms is very small.

As a short conclusion, using the shifted configuration versus the symmetric configuration[1] can be beneficial in saving the shift invariance and doubling the spatial bandwidth when working with one localized hologram. However, for the multiplexing case the shift of the Fourier pattern causes a large degradation of the diffraction efficiency of the multiplexed holograms. Therefore, it is better to use the symmetric configuration for the multiplexing and bear with lower spatial bandwidth by cutting the outer regions of the Fourier pattern, considerably larger shift invariance is achieved.

4.6.3 Effectiveness of Schedule Modification

The modification of the recording rise time in the recording time calculations has resulted in a more uniform strength distribution for the multiplexed holograms. Comparing the peaks on the two ends of the shift range in Figure 34(b), it is observed that the first and last recorded holograms have about the same strength. Also, the peaks in the middle of the shift range have comparable strengths to those on the two ends. The effectiveness of the modification of the schedule can be further validated. Comparing Figure 33(b) for the multiplexing with the initial calculated schedule in Section 4.5.2 with Figure 34(a) for the multiplexing with the modified schedule is clear that the ratios of the middle peaks to the average of the two end peaks are larger in Figure 34(a) than in Figure 33(b). It is inferred

[1] Refer to Section 2.3.1 in Chapter 2 for the shifted and symmetric configurations.

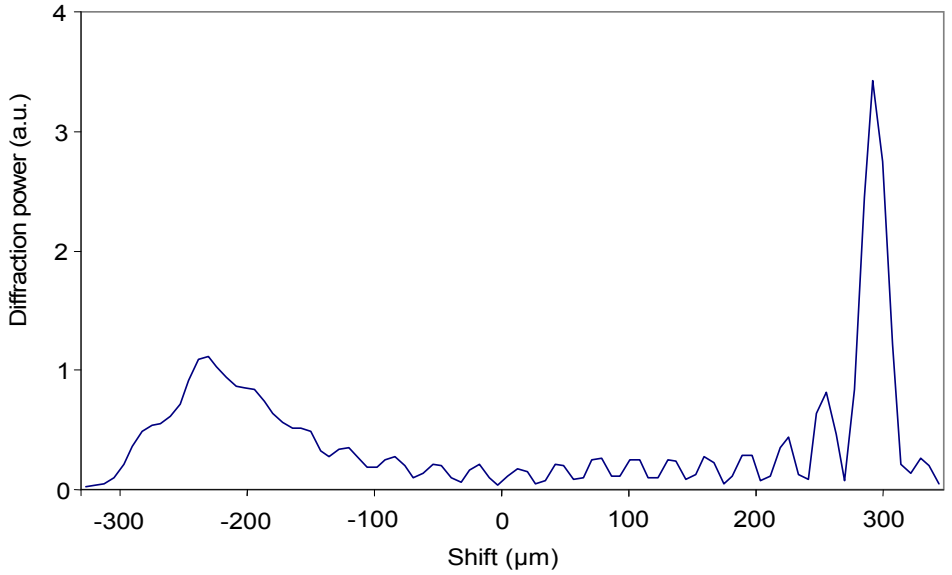

(a)

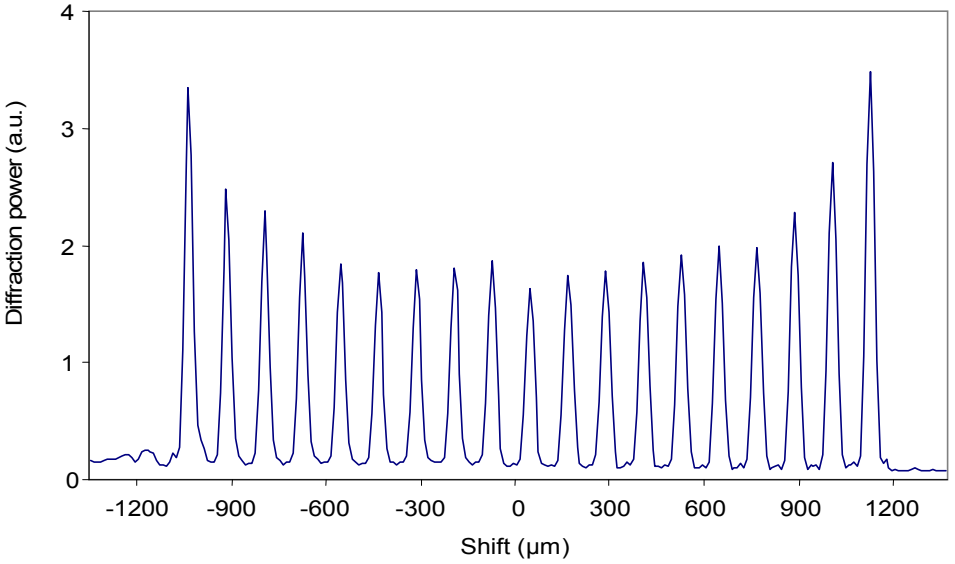

(b)

Figure 34. Shifted configuration effect and the effectiveness of schedule modification. In two separate multiplexing experiments, 20 holograms have been multiplexed in one slice with the pattern shift of 32 μm in (a) and 120 μm in (b) between each two recordings. The recording time schedules for the two experiments have been exactly the same and were modified versus the schedule used in Figure 33. The shifted configuration has been used.[1] The reading pattern (same as the recording pattern) has been shifted and the diffraction power has been measured for each location of the pattern. The first peak on the left corresponds to the first recorded hologram.

[1] Refer to Section 2.3.1 in Chapter 2 for the shifted and symmetric configurations.

that as expected, the actual recording time constant for the persistent part of the recorded holograms is larger that what is measured by the curve fitting as performed in Section 4.5.2.

4.7 Shift Invariance Enhancement Results

Following the initial experimental results for the multiplexing, the shift invariance of this system has been enhanced by multiplexing 20 holograms of the same pattern in one slice of the recording medium using the setup illustrated in Figure 28 [49]. The results are shown in Figure 35. The pattern has been shifted by 30 μm between each two recordings. The shift invariance is increased to ±325 μm, which is more than 9 times larger than the shift invariance of an individual hologram (±35 μm as illustrated in Figure 30). The pattern shift between each two recordings for the multiplexing has been smaller than the shift invariance of individual holograms, which has helped obtaining a more uniform curve.

Considering the initial experimental results for the multiplexing, the experiment parameters have been modified to achieve a relatively smooth shift invariance curve for the enhanced LHC. Based on the results in Sections 0 and 4.6.3, the shifted configuration has been replaced with the symmetric configuration to maintain the uniform diffraction efficiency distribution for the multiplexed holograms. The disadvantage of the symmetric configuration versus the shifted configuration is the limitation of the spatial bandwidth of the patterns that can be correlated with the LHC. Therefore, there is a trade-off between the shift invariance enhancement and the spatial bandwidth of the correlated patterns in the LHC.

In Figure 35, it is notable that the diffraction power is about 11 dB larger at the curve top with respect to the power value where it reached its lowest amount on the sides of the curve. Although as expected this ratio is smaller that that in the curve for one recorded hologram (Figure 30), which is about 20 dB, it is more than enough for the recognition of the examined pattern with a low false classification rate. Moreover, the variation of the diffraction power at the curve top (for the shift range from -265 μm to 265 μm) is less than 2 dB.

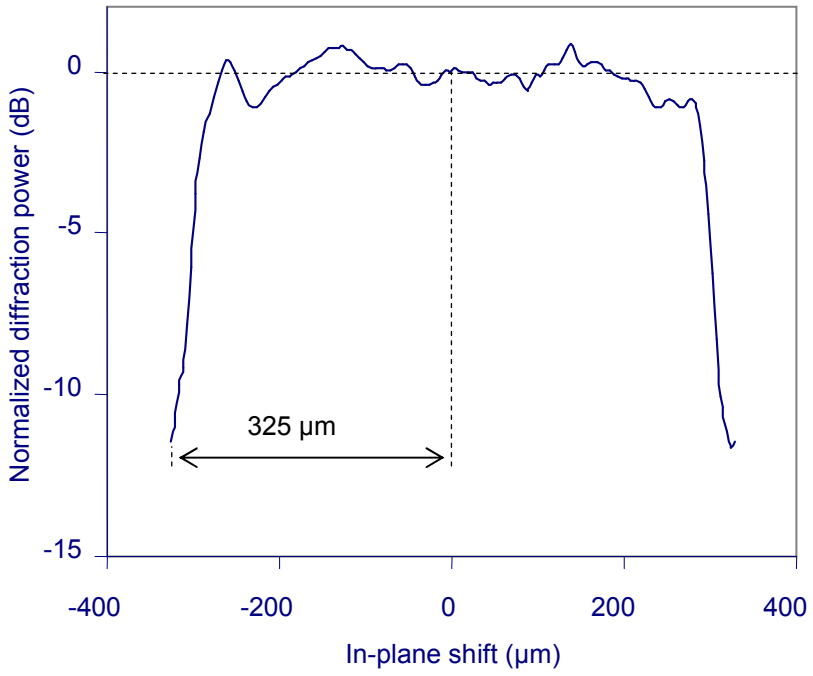

Figure 35. Shift invariance enhancement in LHC. 20 holograms from the shifted versions of the same pattern are multiplexed in one slice. The pattern has been shifted each time by 30 μm. The shift invariance is increased to ±325 μm. The diffraction power values are normalized to the average power value of the curve top (for the shift range from -265 μm to 265 μm). The symmetric configuration has been used.[1]

[1] Refer to Section 2.3.1 in Chapter 2 for the shifted and symmetric configurations.

In addition, the calculation of the recording time schedule has been modified by assuming a larger recording time constant (τ_r = 16 min) and a smaller long erasure time constant (τ_{e2} = 20 min) than the assumed values in Section 0, which has led to the best result obtained for the multiplexing. These values are obtained by analyzing the multiplexing results and fine tuning the experimental time schedules. It can be inferred that the actual values for the recording time constant and the long erasure time constant are close to τ_r = 16 min and τ_{e2} = 20 min, respectively. The reason is the calculated recording time schedule based on these values results in the most uniform hologram strength distribution for the multiplexed holograms.

To achieve the shift invariance curve presented in Figure 35, it has been required to assign smaller relative hologram strengths for the holograms closer to the two ends of the shift range. The reason is even with the symmetric configuration there is a small amount of phase variation for the diffraction signal from each multiplexed hologram when the reading pattern is shifted, since the symmetry cannot be perfectly applied and the two sides of the Fourier transform pattern at the entrance facet of the crystal are not evenly cut off (refer to Figure 8). Therefore, the holograms recorded with the pattern in the middle of the shift range still experience a slight destructive superposition from their overlapping neighbor holograms. This effect is weaker for the holograms closer to each end of the shift range. Therefore, the stronger diffraction efficiency for these holograms needs to be offset by the smaller hologram strengths assigned to them. This assignment is performed using the coefficient C_n in Equation (18). The C_n values are depicted in Table 2. For multiplexing 20 holograms with the first hologram recorded to saturation, the calculated recording times for the 2nd hologram to the 20th hologram ranges from 14.6

minutes to 0.5 minutes. The holograms have then been erased by recording a Bragg mismatch hologram in the same slice for 20 minutes, with the 2D pattern shifted far from the pattern shift range during the multiplexing.

Table 2. Relative hologram strengths assigned for shift invariance enhancement

Hologram # (n)	1	2	3	4	5	6 - 15	16	17	18	19	20
C_n	1	1.2	1.45	1.75	2.1	2.5	2.1	1.75	1.45	1.2	1

In another multiplexing experiment, 20 holograms have been multiplexed in one slice of the recording medium. The same recording time schedule used for the shift invariance enhancement presented in Figure 35 has been applied with the variations of the assigned hologram strength as depicted in Table 2. The results are shown in Figure 36. The 2D pattern has been shifted by 120 μm between each two recordings, which is much larger than the shift invariance of individual holograms (35 μm). Therefore, the diffraction signal from any of the multiplexed holograms has not been destructively affected by the diffraction signals from the other multiplexed holograms. The effect of the variation of the assigned hologram strengths is clearly visible for the holograms close to two ends of the shift range, whereas in Figure 35 this effect is not noticeable. This comparison verifies the slight destructive superposition of the diffraction signals from neighboring holograms even though the symmetric configuration is applied. The reason as mentioned before is the imperfect symmetry at the entrance facet of the recording medium that causes small phase variations of the diffraction signal when the reading 2D pattern is shifted.

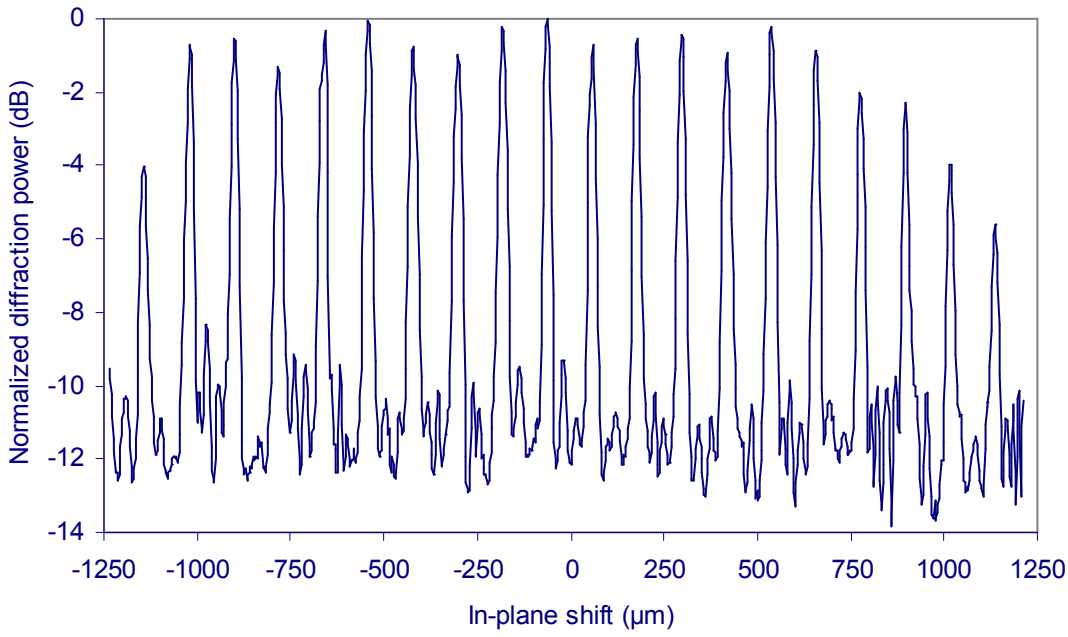

Figure 36. Diffraction power from 20 multiplexed holograms in one slice with modified recording time schedule. The same recording time schedule used in Figure 35 has been applied. For the multiplexing, the pattern has been shifted by 120 µm between each two recordings. The reading pattern (same as the recording pattern) has been shifted and the diffraction power has been measured for each location of the pattern. The first peak on the left corresponds to the first recorded hologram. The Readout has been done after 30 minutes of Bragg mismatch erasure. The diffraction power values are normalized to the maximum peak value.

4.8 Rotation Invariance Enhancement Results

As mentioned in Section 4.2, the rotation invariance is limited in all optical correlators for the rotation of the 2D pattern about the axis of the signal beam (i.e., *z*-axis in Figure 28). As seen in Figure 24, the reason is this rotation contains in-plane shift of the pattern in the areas of the 2D pattern where the rotation radius is parallel to or makes a small angle with the *y*-axis as in Figure 28. Using the multiplexing method it is possible to

improve it considerably in LHCs. By means of the same method for improving the shift invariance, the rotation invariance of the LHC is enhanced as well.

Before the multiplexing of the holograms, the actual rotation invariance of an individual hologram recorded in one slice of the recording medium has been measured. Based on the rotation invariance value for one hologram, the rotation angle of the 2D pattern between each two recordings during the multiplexing is determined. The measurement results are shown in Figure 37(a). The shift selectivity curve for an optical correlator is usually expected to resemble a sinc^2 function and the shift invariance is defined as the distance between the locations of the maximum and the first null of that sinc^2 function. To stick with this definition for the rotation invariance, a sinc^2 function has been fitted to the curve obtained for the rotation selectivity. From the fitted sinc^2 curve, the rotation invariance of one hologram is ±0.29º from the peak to the nearest nulls on each side of the peak.

For the rotation invariance enhancement, 12 holograms have been multiplexed in one slice with 0.34º rotation of the 2D pattern between each two recordings to improve the rotation invariance. Figure 37(b) shows the result of the multiplexing. The rotation invariance has been increased to 2.4º, which is a factor of 8 improvement. To calculate the recording time schedule, Equation (18) has been solved with the recording time constant τ_r = 16 min and the long erasure time has been τ_{e2} = 20 min, the same values used for the shift invariance enhancement. The same strength for all the multiplexed holograms is considered (i.e., C_n = 1 for every n). For multiplexing 12 holograms with the first hologram recorded to saturation, the calculated recording times for the 2nd hologram to the 20th hologram ranges from 12.4 minutes to 1.7 minutes. All of the

holograms have been erased for 20 minutes after the multiplexing process with the 2D pattern rotated by 5º to ensure a completely Bragg mismatch erasure.

Because the pattern rotation step has been larger than the rotation invariance of individual holograms, the curve top for the shift invariance of the multiplexed holograms is not as uniform as in Figure 35(b). Nonetheless, the diffraction power is large enough for the pattern recognition with a low false classification rate over the rotation invariance range.

For this experiment the shifted configuration has been used.[1] Nonetheless, the destructive superposition present in shift multiplexing does not seem to destructively affect the diffraction signal from the holograms in the middle of the rotation range. It should be noted that the rotation about the *z*-axis as mentioned before, consists of multiple linear shifts along the rotation radii. The linear shift value increases with the distance from the rotation axis, which results in the increase of the phase variation associated with the shifted configuration. The superposition of all these different phase variations has a small range of variation compared to the phase variations due to a simple in-plane shift of the pattern. Therefore, the superposition of the diffraction signals from the multiplexed holograms overlapping over the rotation range does not decrease the overall diffraction signal. Hence, it is possible to maintain the large spatial bandwidth of the examined 2D patterns by using the shifted configuration without sacrificing the rotation enhancement capability.

[1] Refer to Section 2.3.1 in Chapter 2 for the shifted and symmetric configurations.

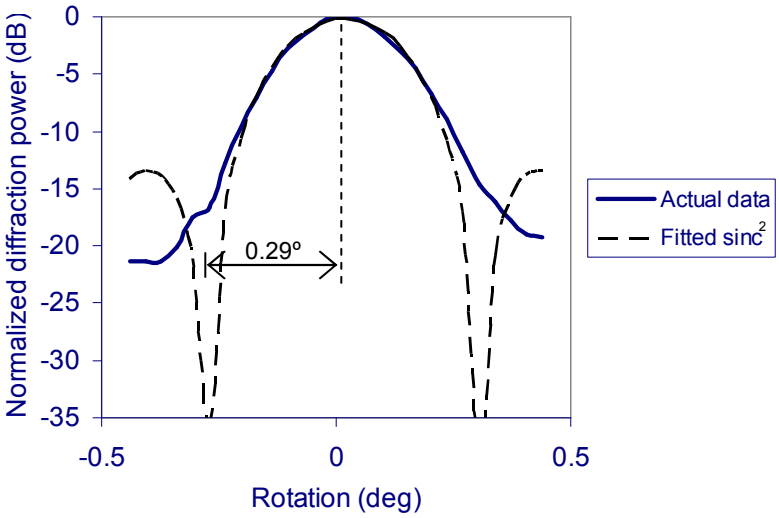

(a)

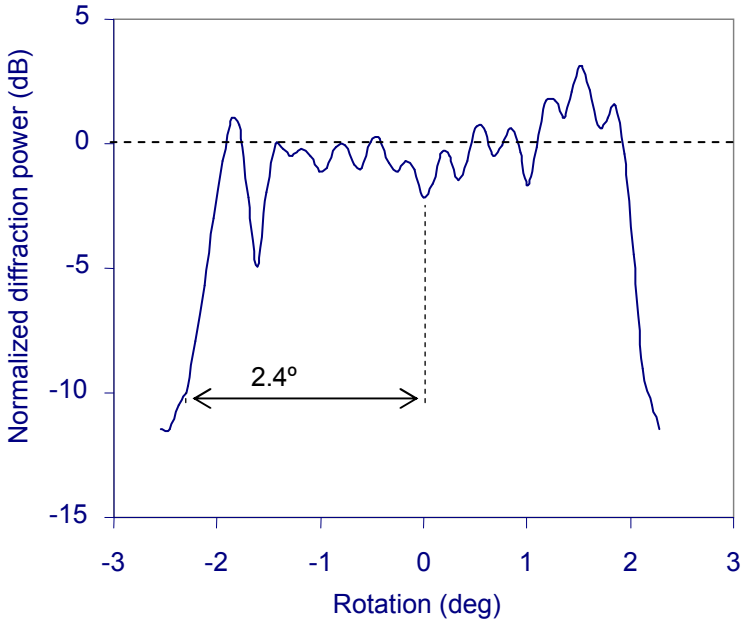

(b)

Figure 37. Normalized diffraction power versus the rotation of the reading pattern about the *z*-axis (see Figure 28). (a) One hologram is recorded. The rotation invariance of one hologram is ±0.29º based on the fitted sinc^2 function. The diffraction power values are normalized to the power value at the peak. (b) 12 holograms from the rotated versions of the same pattern are multiplexed in one slice. The pattern has been rotated each time by 0.34º. The shift invariance is increased to ±2.4º. The diffraction power values are normalized to the average power value of the curve top (for the rotation range from -1.9º to 1.9º). The shifted configuration has been used (refer to Section 2.3.1 in Chapter 2).

4.9 Three Dimensional Object Recognition Using LHC

Because of the intrinsic 3D nature of the holographic information storage [1], researchers have been attracted to using it for 3D object recognition. A hologram is capable of storing the amplitude and phase of the wavefront emitted from the surface of a 3D object and correlate it with the wavefronts received from the examined 3D objects. The parallelism capability and high capacity of the volume holograms make them better candidates for developing 3D object recognition systems [12]. Other 3D recognition techniques such as 3D joint transform correlation [50] and digital holography [51] rely on 2D multiple scans of the examined object, which significantly delays the recognition process.

By use of the established LHC for 2D patterns, it has been intended to improve the capabilities of the holographic 3D object recognition systems to make them dynamic, compact, and more robust. As calculated in Section 2.4.3, a hologram can be recorded in each slice of the recording medium in LHCs with much larger diffraction efficiency than that of the conventional (e.g., angle-multiplexed) volume holograms. Therefore, it is possible to multiplex several aspects of the same object along with the shifted and rotated versions of it in the same slice resulting in more robust 3D object recognition.

To investigate the potential capabilities of the LHC for 3D object recognition, the LHC system used for the correlation of the 2D patterns has been transformed to a 3D object recognition system with some modifications. Figure 38 illustrates the experimental setup for 3D object recognition using LH recording. The 3D object under examination is a toy car with the dimensions of 70 mm × 29 mm × 18 mm. The object is placed on a horizontal rotation stage, driven by a servo-controlled actuator with its rotation axis passing through the center of the object. This rotation corresponds to the horizontal angle

of view of the 3D object by the crystal. The signal beam is passed through a hole in a concave mirror and is expanded to illuminate the entire object. The concave mirror has a diameter of 15 cm and a focal length of 6 cm. The center of the object is placed close to the focal point of the concave mirror. The light reflected from the object is collected by the concave mirror and then focused to the crystal. The light beam illuminating the 3D object propagates obliquely downward, therefore it does not directly enter the crystal. The concave mirror is positioned at an angle as well. The crystal is the same used in the 2D LHC. The reference and UV beams are shaped and delivered exactly as in the 2D LHC except for the cylindrical lens CL1 whose focal length is changed to 7.5 cm.

The reason for placing a relatively large concave mirror for the collection of the light is it collects the light reflected from most of the object surfaces. Also, for the recording of holograms in the photorefractive crystal, the recording beam intensity levels are required to be large enough to maintain a minimum recording speed. Otherwise, the recording times will be so large (e.g., hours) and it becomes difficult to retain the stability of the interference pattern during the recording. Having a short focal length also helps increasing the light intensity at the entrance facet of the crystal. With all these consideration, the signal beam intensity provided for the recording at the entrance facet of the crystal is estimated to be about 50 mW/cm^2 when using the maximum power of the green laser; 5.5 W.

Using the rotation stage in the setup, the rotation invariance of the 3D recognition system is measured. Figure 39 shows the diffraction efficiency versus the rotation angle. The rotation invariance is at most ±0.004º. It means that the LHC is extremely selective to the horizontal rotation of the 3D object. The measurement has been performed by

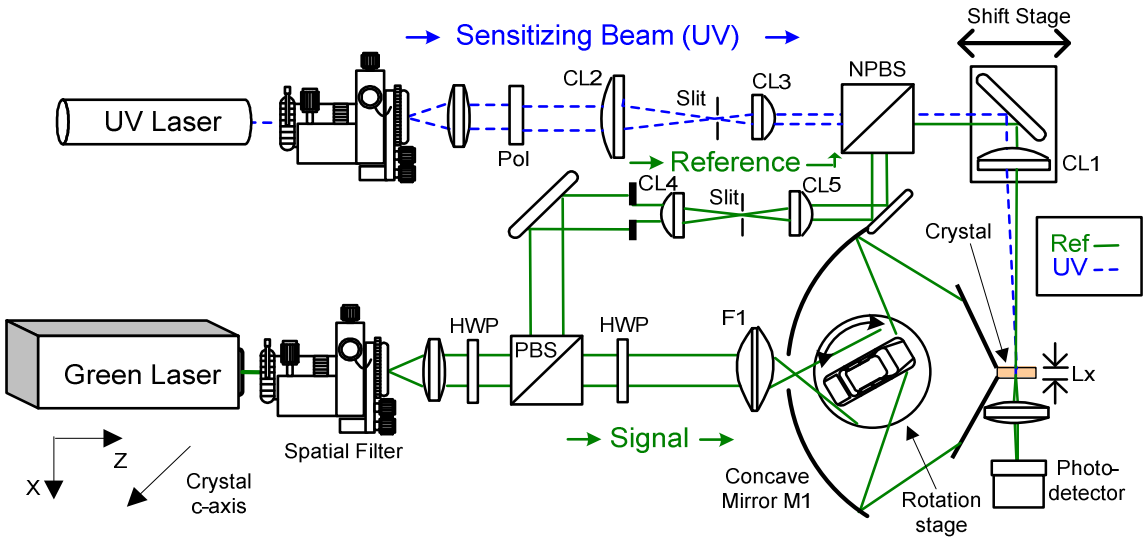

Figure 38. Experimental LHC setup for 3D object recognition. The object under recognition is a toy car, sitting on a rotation stage. The center of the car is close to the focus of the concave mirror. The recording medium is a 45-degree-cut congruently grown $LiNbO_3$:Fe:Mn crystal doped with 0.15 wt% Fe_2O_3 and 0.02 wt% MnO. HWP: half-wave plate, PBS: polarizing beamsplitter, NPBS: non-polarizing beamsplitter, CL: cylindrical lens, Pol: polarizer. Object size = 2.9 mm × 70 mm × 1.8 mm, lens focal lengths: f_l = 1.5 cm, f_{CL1} = 7.5 cm, concave mirror diameter = 150 mm, f_{M1} = 6 cm, distance of the object to the crystal = 2.5 cm.

rotating the stage from its initial position to one direction. Therefore, half of the selectivity curve is obtained. For a complete rotation selectivity measurement, it is required to rotate the stage to one direction far enough from its initial angle, then rotate it back towards the initial angle, and continue rotating until the diffraction power reaches its minimum. Because the system is very sensitive to the variations, the diffraction signal cannot be retrieved as the stage is rotated back to its initial angle during the recording. In other words, the required repeatability for the selectivity measurement or in principal performing the 3D recognition is beyond the practical limitations of the current LHC system.

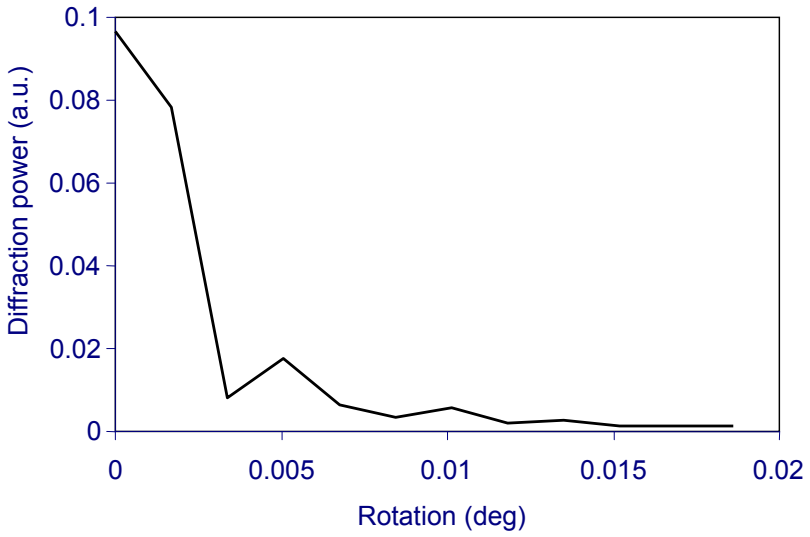

Figure 39. Rotation selectivity of the LHC for 3D object recognition. The rotation selectivity is about ±0.004º.

The large rotation sensitivity of the LHC can be explained by an analogy with the 2D LHC. As discussed in Section 2.4.2 in Chapter 2 for 2D LHC, the larger the spatial bandwidth of the system, the more limited is the in-plane shift invariance. In the implemented 3D LHC, the spatial bandwidth is larger than that in the 2D LHC studied in Chapter 3, as the focusing element (i.e., the concave mirror in the 3D LHC and the Fourier transform lens F3 in the 2D LHC) has a smaller focal length (f_{M1} = 6 cm in Figure 38 compared to f_3 = 12.5 in Figure 14). By reducing the width of the crystal (L_X in Figure 38) or limiting the width of the light pattern entering the crystal it is possible to further reduce the spatial bandwidth. However, this will limit the diffraction efficiency of the recorded holograms as well either by reducing the $M/\#$[1] by reducing the crystal width, or by reducing the recording speed by limiting the light admitted to the crystal. Furthermore,

[1] Refer to Section 2.4.3 in Chapter 2 for the definition of $M/\#$.

the smaller spatial bandwidth of the 3D LHC results in sacrificing the capability of recognition of the finer features of the 3D objects.

In addition, the 3D object as seen in Figure 38 is illuminated by a diverging spherical beam, which results in less rotation invariance. This effect can be explained by an analogy with the 2D LHC as well. Illuminating the 2D pattern with a diverging spherical beam is translated as a quadratic phase term multiplied by the 2D pattern f(ξ,η) using the paraxial approximation. The extra phase term appends an exp(.) term to Equation (8) from Chapter 2:

$$\mathrm{A_d}(\mathbf{k_d}) \propto L_X L_Z \iint_{\mathrm{SLM}} \mathrm{f_1^*}(\xi_1, \eta_1)\mathrm{d}\xi_1\,\mathrm{d}\eta_1 \int_{\mathrm{SLM}-\xi} \mathrm{f_2}(\xi_2, \eta_1 + \Delta\eta)\mathrm{d}\xi_2$$

$$\times \mathrm{sinc}\left(\frac{L_X}{2\pi}\beta\right)\mathrm{sinc}\left(\frac{L_Z}{2\pi}\alpha\right)\exp\left(-\frac{L_X}{2}\beta\right)\exp\left[j\left(Z_C + \frac{L_Z}{2}\right)\alpha\right]\exp\left[\frac{\pi}{\lambda d}\left(\xi_1^2 - \xi_2^2 - 2\eta_1\Delta\eta - \Delta\eta^2\right)\right], \quad (21)$$

where d is the distance between the illuminating point source in front of the 2D pattern and the 2D pattern. The other symbols are introduced in Section 2.3 in Chapter 2. This extra exp(.) further limits the shift invariance of the 2D LHC when the integrals in Equation (21) are performed over the SLM area. Similar effect is expected to reduce the shift invariance or rotation invariance of the 3D LHC as mentioned above.

4.10 Discussion

Based on the existing trade-offs of the LHC, the LHC parameters can be optimized for specific applications. The number of the slices within which the holograms can be multiplexed is limited to the length of the recording medium and the minimum thickness of the slices (L_Z in Figure 7). Therefore, the number of the independent patterns that can be recorded and later recognized by the LHC is limited. As mentioned in the beginning of

this chapter, the diffraction efficiency of the holograms is not a limiting factor provided only one hologram per slice is recorded.

In Section 2.4.3 in Chapter 2, it was quantitatively discussed how the diffraction efficiency of the multiplexed holograms varies inversely proportional to the square of the number of holograms multiplexed within the volume of one slice [13]. Therefore, there is the trade-off between the diffraction efficiency and the number of multiplexed holograms. The multiplexing is performed to record multiple variations of the patterns within the corresponding slices and enhance the robustness of the LHC versus the variations of the reading patterns. It is inferred that the enhancement range is limited by the desired diffraction efficiency of the holograms. As a design parameter, it is possible to increase the thickness of the slices, which increases the dynamic range of the slices. This way the number of multiplexed holograms can be increased, but on the other hand, reduces the number of slices for a fixed crystal length. Therefore, it is possible to increase the robustness of the LHC at the cost of reducing the number of recorded patterns.

For the 3D LHC, it seems that using a much smaller 3D object may result in better rotation invariance. First, the rotation of a smaller object will result in smaller linear shift that includes the in-plane shift, which the LHC is most sensitive to. Second, illuminating a small object is less complicated. The illuminating beam will not be required to be large. Therefore, making the light beam diverging for the expansion will not be necessary, which alleviates the extreme sensitivity of the LHC due to the illumination with a diverging spherical beam. After solving the sensitivity problem of the 3D LHC, it becomes possible to compare its performance with the existing optical 3D object recognition systems and enhance it using multiplexing.

CHAPTER 5

HOLOGRAPHIC DATA STORAGE WITH TWO-CENTER RECORDING

5.1 Introduction

Holographic data storage systems are promising solutions for next generation massive data warehousing systems and storage devices with very high rate of data transfer, very high capacity, and high data longevity [3]. In a binary holographic data storage system, the data bits are formed as 2D pages of dark and bright pixels on an SLM, corresponding to ones and zeros as the bit values. The SLM can be a transmissive miniature liquid crystal display (LCD) or a reflective micromirror array chip. For each data page, a signal beam is produced by the SLM illuminated by an expanded laser beam. The interference of the signal beam and the corresponding reference beam is recorded as a hologram in a holographic recording medium. The data pages are retrieved by reading their corresponding holograms. Each hologram is read with one short exposure of the reference beam. The retrieved 2D data page is imaged onto a camera and the digital data is extracted from the bit pattern image captured by the camera.

Each data page may contain over a million bits of data depending on the resolution of the SLM, camera, and the imaging system. Therefore, over a million bits are retrieved with a short pulse of light, whereby, very high data transfer rates are achieved in holographic data storage systems. Furthermore, by introducing the concept of multiplexing of the holograms in thick recording media [2], the capacity of the holographic memories has been significantly increased. Several types of materials,

organic and inorganic, have been developed that offer very high dynamic ranges for multiplexing thousands of holograms in the volumes of about a cubic centimeter. These materials allow for recording long life holograms. This property of the holographic materials makes them the best candidate media for long term data archiving applications.

From a communications perspective, the entire process of applying the data bit patterns to the SLM, recording the corresponding holograms and reading them, and receiving the reconstructed image of the bit patterns on the camera is another example of multiple communications channels [52]. Each channel, called a holographic channel, transmits data from each pixel on the SLM to its corresponding pixel on the camera. In the case of data oversampling, each holographic channel is attributed to a group of pixels (also called pixel blocks or super pixels).

The data received by each camera pixel, which is the light power collected by the corresponding detector cell, is of analog nature and has to be transformed to digital data. The captured image is further processed to extract the digital data with the minimum bit error rate (BER). In the binary case, the digital data extraction can be as simple as to decide whether the received intensity is low enough to be interpreted as zero or high enough to be interpreted as one. If the image contrast ratio is large enough and the received pixel intensities are not spread much form their original values on the SLM, then the pixel intensities corresponding to ones and zeros are well separated and the bit value assignment becomes less complicated. A histogram of the pixel intensity values of such image will demonstrate two well separated peaks associated with dark and bright pixels. The peaks will be rather narrow and their tails do not overlap much. The overlaps of the tails of the histogram peaks are a measure for noise. It is implied that the larger the

separation of the peaks in the histogram and the narrower the peaks, the less is the probability of false pixel bit value assignment (i.e., smaller raw BER) and the overlap of the tails (larger SNR). In general, a data storage system with larger SNR is expected to yield smaller raw BER and vice versa. The final BER of a data storage system, determined by the employed data detection and data coding schemes, is also smaller for larger SNR.

During this research, a holographic system with angle multiplexing capability in 90-degree geometry has been developed. The two-center recording in doubly doped refractive crystals has been utilized for recording persistent holograms.[1] The recording medium is placed near the focal plane of a 4-f imaging system. The bit patterns used in this system have the finest pixel size (28 μm) and the largest resolution (512 × 384) among the developed holographic memories based on two-center recording, to the best of the author's knowledge. The results of the coherent imaging of the SLM onto the camera through a 4-f imaging system with the holographic crystal and the pixel matching of the SLM and the camera are presented. A novel normalization technique has been developed with which the coherent images of the bit patterns are significantly enhanced and the undesired fringes and speckles due to the coherent imaging are efficiently removed. Using a simple data detection method, the imperfections of the imaging system have been handled for accurate pixel matching of the SLM and camera.

The histogram of the final detected intensities received through the holographic data channels shows a large separation between the dark and bright intensity distributions. From the histogram, the estimated SNR is 7.4 for the entire image, which is

[1] Refer to Section 1.4.2 in Chapter 1 for two-center recording.

the largest reported for a holographic data storage system based on two-center recording. The theoretically estimated raw BER based on the achieved SNR of the pixel matching is 10^{-7}, which is also achievable when only one hologram is recorded in the holographic recording medium.

The problems involved with two-center recording of holograms of high resolution patterns have been addressed. The refractive index fluctuations within the crystal volume produced by the nonuniformities of the UV (sensitizing) beam profile and tight focusing of the signal beam have been significantly reduced by spatial filtering of the UV beam and defocused recording. It has been possible to multiplex 10 holograms within the crystal. The reconstructed bit pattern images from the multiplexed holograms show good contrast. With the stability improvement of the recording system, multiplexing of about 100 holograms with good SNR of the reconstructed bit pattern images is achievable.

The holographic data storage system developed in this research is based on volume multiplexing of the holograms, in which all the multiplexed holograms overlap in the same volume of the recording medium. Therefore, selective recording and erasure of individual holograms is not possible as all the recorded holograms are affected during the recording and erasure. As mentioned in the previous chapters, the selective recording and erasure is an exclusive feature of the localized recording.[1] Furthermore, the excessive diffraction efficiency of the localized holograms[2] leads to larger SNR of the holographic channels that can be used for capacity improvement through multilevel (M-ary) data coding versus the conventional binary data coding. The adoption of the localized

[1] Refer to Section 1.5 in Chapter 1 for localized recording.
[2] Refer to Section 2.4.3 in Chapter 2 for the large diffraction efficiency of the localized holograms.

recording technique for advancing the holographic data storage systems to dynamic read/write/erase devices with high capacity has been discussed.

5.2 Coherent Imaging

The imaging of the SLM bit pattern onto the camera in the holographic data storage systems is performed in coherent regime. The reason is both the signal and reference beams have to be coherent, therefore, they can produce stationary interference patterns that can be recorded as holograms. In an imaging system with an amplitude transfer function (ATF) wide enough for imaging a pattern with a certain spatial bandwidth, the contrast of the image is usually better when the pattern illumination is coherent than when it is incoherent [59]. Therefore, the coherent imaging of a reconstructed signal beam by reading the corresponding hologram can potentially result in better contrast of the image, hence larger SNR of the system. On the other hand, there are undesired effects involved with the coherent imaging such as the speckling and the diffraction and interference fringes that add extra noise to the image [53]. These effects are much less bothersome in incoherent imaging. In the following, these effects and the available solutions are discussed.

5.2.1 Speckling Effect

If a smooth pattern with relatively large features is illuminated by a coherent beam through an immobile diffuser that applies a random phase distribution to the pattern, then there will be a random speckle pattern added to the image of the pattern. If the illumination is incoherent, however, then adding a diffuser in principle does not affect the image. The creation of the speckles is because of the steady interference of the coherent

lights scattered from the closely spaced scattering centers on the diffuser with random phases with respect to each other. If the random phase pattern of the illumination is changed (e.g., by using a different region of the diffuser), the speckle pattern at the image plane is changed as well and the new speckle pattern is uncorrelated with the old one. The rough fluctuations of the illuminating beam profile along with the large roughnesses on the optical surfaces and random scatterings within the volume of the optical components of the imaging system can also produce speckles at the image.

The size of the speckles is approximately the size of the amplitude point spread function (APSF) of the imaging system [59], which is the diffraction limit in an aberration-free imaging system. In such condition, it becomes very difficult to attain the best resolution of the imaging system for imaging high resolution bit patterns because the size of the pixels is about the same as the size of the random speckles that are accounted for noise. Therefore, the SNR of the system is significantly reduced. It may seem possible to average out the speckles on the image by using larger camera pixels or by simply low-pass filtering the image using a smoothing filter in the computer. However, the resolution of the images is reduced by the low-pass filter as well, which results in lowering the system capacity in terms of data density per page and nothing is gained.

5.2.2 Diffraction and Interference Fringes

Another problem of the coherent imaging is the undesired diffraction and interference fringes appearing in the image. Every tiny dust particle or crack on the optical surfaces in the path of the signal beam can produce very obvious diffraction fringes in the final image. Also, the interferences of the reflected lights the optical surfaces generate fringe patterns that are quite visible in the bit pattern image. Because of the coherence

illumination, the unwanted diffraction and interference fringes, even with small amplitudes, are amplified by their interference with the main signal beam, since all the lights are in phase. This amplification does not occur in the incoherent imaging as the fringes and the main light beam have a randomly time varying phase with respect to each other, therefore, their interferences are time averaged to zero.

All the mentioned effects for the coherent imaging can add significant amount of noise and greatly limit the effective contrast of the bit pattern image. It is implied that the implementation of a coherent imaging system, which is an obligation of the holographic data storage systems, requires much more subtlety and accuracy. The spatial filtering of the beam illuminating the SLM needs to be performed in a way that removes as much fluctuations as possible from the beam profile. The optical surfaces of the optics and devices in the path of the signal beam have to be carefully cleaned, maintained and prevented from cracks, dust particles, and dirt. Therefore, the experimental setup should be implemented in a clean and dust proof area and/or under a protection cover. The optical surfaces are preferred to be anti-reflection (AR) coated to reduce the interference of the reflected lights as much as possible. However, the AR coating may not be applied to the photorefractive crystal, because the coating will be damaged through the oxidation / reduction process. The normalization techniques can also reduce the diffraction and interference fringes [43]. A new normalization method has been developed in this research, with which the fringes are more efficiently removed and a major portion of the speckles are eliminated as well. In Section 5.6.15.6, the conventional blank normalization and the new normalization methods are described and quantitatively compared.

5.3 Pixel matching

As mentioned earlier in Section 5.1, the pixels in a holographic data storage system represent data channels for transmitting digital data from SLM pixels to the camera pixels. As it is always intended to achieve the minimal BER for the data transmittance over the holographic channels, the data detection error is required to be minimized. An important source of the detection error is the inter-pixel crosstalk [54], which is defined physically as the received power in a pixel originated from its surrounding pixels. For the best performance of the system with minimum BER, all the pixels of the reconstructed image from the hologram are required to be imaged at the center of their corresponding camera pixels as accurately as possible. In other words, the SLM image and the camera detector array need to be pixel matched. Furthermore, it is necessary that the image of each SLM pixel is confined within the area of the related camera pixel. The variation of the magnification ratio of the imaging system, the lateral shift of the image versus the camera detector array, and the imaging distortion result in the deviation of the image pixels from the camera pixels. Moreover, the limitation of the ATF bandwidth of the imaging system, the optical aberrations, and the defocus of the camera can enlarge the images of the SLM pixels leading to more inter-pixel crosstalk.

To achieve the best pixel matching, the imaging system and its components are required to be carefully designed, fabricated, and aligned. In a 4-f imaging system, the Fourier transform lenses have to be designed and fabricated to provide the exact required magnification ratio with the desired contrast for the maximum spatial frequency of the SLM bit patterns. The minimum numerical aperture of the lenses has to be large enough for the smallest APSF needed for the coherent imaging of the bit patterns. The lenses

have to be made as aberration free as possible to reach as close as possible to the diffraction limit of the imaging system. The lateral shift of the SLM image versus the camera has to be constantly monitored, or actively controlled, for more efficient pixel misregistration compensation. Finally, the alignment of the imaging system components together with the SLM and the camera must be performed precisely.

It should be noted, however, that for the imaging of high resolution bit patterns, it becomes quite challenging to fulfill all the mentioned requirements for the imaging system to their perfection. Depending on how accurately the imaging system is designed and implemented, there will remain some imaging imperfections and distortions. By further processing of the captured image with the residual inter-pixel crosstalk, it is possible to retrieve the data with less detection error and further decrease the BER of the data storage system [54,55].

5.4 Holographic Data Storage Setup

Figure 40 is a schematic illustration of the holographic memory system built with the angular multiplexing capability and 90-degree geometry [37,43]. A polarizing beamsplitter divides the spatially filtered and expanded laser beam into signal arm (TM polarization; electric field vector parallel to the plane of Figure 40) and reference arm (TE polarization; electric field vector normal to the plane of Figure 40). The light source for the recording is a diode-pumped solid state CW laser (Verdi V5 from Coherent) with wavelength of 532 nm. As mentioned in Section 3.3 in Chapter 3, the selection of the green light over the red light results in much larger recording sensitivity and eventual diffraction efficiency of the holograms with the cost of less persistence of the holograms [45]. However, depending on the erasure time constant during the reading, the holograms

can be read for over 100,000 times before they are required to be refreshed (300,000 times for the case explained in Ref. [45]). Furthermore, the green lasers are available at much larger output powers (e.g., the exploited solid state laser) than the He-Ne red lasers. The sensitizing light source is a CW diode laser (from Power Technology) with wavelength of 404 nm.

5.4.1 Spatial Light Modulator and Camera

An SLM (XGA4 from CRL Opto [56]), which is an LCD panel with 1024 × 768 resolution and 14 µm × 14 µm pixel pitch, modulates the signal beam with 2D data

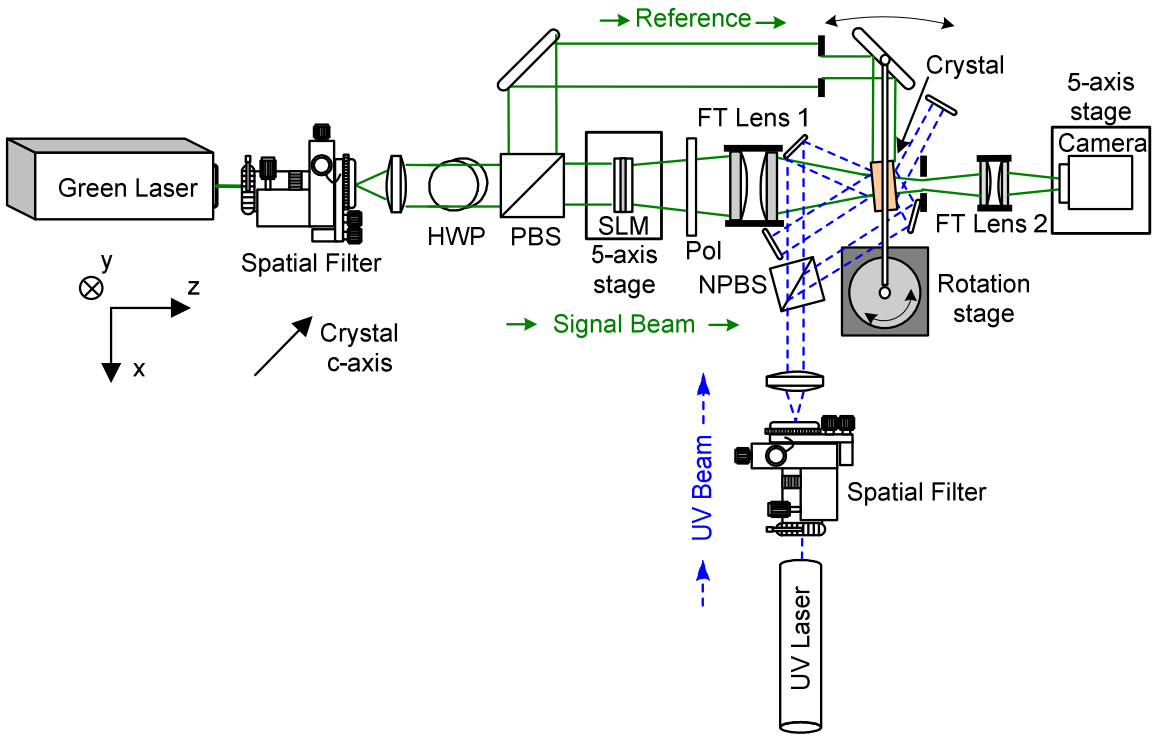

Figure 40. Holographic memory setup with two-center recording. Angular multiplexing is used. The recording medium is a 45-degree-cut congruently grown $LiNbO_3$:Fe:Mn crystal doped with 0.075 wt% Fe_2O_3 and 0.01 wt% MnO. HWP: half-wave plate, PBS: polarizing beamsplitter, NPBS: non-polarizing beamsplitter, FT: Fourier transform, Pol: polarizer. Lens focal lengths: f_{FT1} = 12 cm, f_{FT2} = 5.7429 cm. SLM pixel pitch = 14 µm, camera pixel pitch = 6.7 µm.

pages. The attached sheet polarizers of the SLM are removed and a polarizer with better quality is placed behind the SLM. The front polarizer is not necessary because the light entering the SLM is TM polarized by the polarizing beamsplitter. The polarizer behind the SLM transmits the TE polarized components of the light beams passed through the SLM liquid crystal cells and blocks the TM polarized components. The camera (CV1280 from Prosilica) has a CMOS sensor array with 1280 × 1024 resolution and 6.7 μm × 6.7 μm pixel pitch. Both the SLM and the camera are placed on 5-axis precision stages.

5.4.2 4-F Imaging System

The pattern on the SLM is imaged onto a camera using a 4-f imaging system. Two Fourier transform lens assemblies of the 4-f system are designed and fabricated so the pixels of the SLM are imaged one by one onto the pixels of the camera in a 1024 × 768 block of pixels according to the SLM pixel array size. Both the Fourier transform lens assemblies are placed on 5-axis precision stages. Each lens assembly comprises two identical plano-convex lenses with a spacing ring between them, all secured in a lens tube. The thickness of the spacing ring has been fine tuned to approach the exact target magnification ratio; 6.7 μm / 14 μm = 0.47857. The two Fourier transform lens assemblies have been aligned with respect to the axis of the imaging system (z-axis in Figure 40) using an autocollimator. The resulting demagnification ratio is deviated by about 0.05% from its desired value of 0.47857.

By experiment it has been verified that the 4-f imaging system comprised of the two fabricated lens assemblies can produce an image with good contrast from a pattern with dark and bright 2 × 2 superpixels (i.e., 2 × 2 pixel blocks) at the SLM. Therefore, the pixel pitch of the bit patterns applied to the SLM is twice the SLM pixel pitch (i.e., $\delta = 28$

μm). In other words, the holographic channels transmitting the zeros and ones are comprised of 2 × 2 superpixels Therefore, the data pages are oversampled by allocating 4 pixels per each channel, resulting in 512 × 384 = 196608 data channels per page. Using the individual pixels as the holographic channels did not yield enough contrast for an acceptable BER as experimented.

The SLM produces multiple diffraction orders as it resembles a 2D grating because of the liquid crystal cells periodically placed in a 2D matrix. The fill factor of the SLM pixels is much less than 100% (40% as mentioned in the SLM specifications, less than 20% as observed on a highly magnified projection). The two Fourier transform lens assemblies in the 4-f imaging system are optimized for imaging the central order (zeroth order). Therefore, a square window has been placed at the Fourier plane of the 4-f system that blocks all the SLM diffraction orders except the central order. Because of the small fill factor, the higher diffraction orders carry significant amounts of energy. Because only the central order is imaged onto the camera the power efficiency of the system is limited.

5.4.3 Doubly Doped Photorefractive Crystal

A 45-degree-cut congruently grown doubly doped $LiNbO_3$:Fe:Mn crystal with the doping concentrations of 0.075 wt% Fe_2O_3 and 0.01 wt% MnO and the size of 10 mm × 10 mm × 4 mm (width × height × thickness) is used as the recording medium. The crystal has been oxidized at 1000ºC for 24 hours under oxygen flow then reduced at 700ºC for 3 hours under argon flow. The direction of the crystal *c*-axis is shown in Figure 40, which is almost parallel to the grating vector direction. The signal and reference beams are both TE polarized and are ordinary waves for the crystal.

The crystal is placed at a distance from the common Fourier plane of the two Fourier transform lenses with its front facet at about 2 cm in front of the focal point. The explanation for positioning the crystal out of focus is similar to the explanation given in Section 3.5.1 in Chapter 3 for the broadening effect occurred in re-recording the localized holograms. A high flow of photons with enough energy to excite electrons from the Mn traps within the energy bandgap of the doubly doped $LiNbO_3$:Fe:Mn crystal through an area with very small dimensions results in refractive index nonuniformity. In general, every nonuniform light pattern with high intensity and high photon energy that has sharp fluctuations can produce index nonuniformity in doubly doped $LiNbO_3$:Fe:Mn crystal. At the Fourier plane of the 4-f system, the DC part of the signal beam is highly focused. Therefore, the consequent index nonuniformity would undesirably deteriorate the Fourier transform of the bit pattern, if the crystal was placed at the focal point. In reality, this effect has been observed in the experiment by putting the crystal, initially with no index nonuniformity, at the Fourier plane and watching the captured image of the SLM pattern on the camera. The deterioration of the image over time was quite visible. By shifting the crystal off the Fourier plane, the area illuminated by the DC component of the signal beam is enlarged resulting in much less index nonuniformity. Furthermore, the $M/\#$ is increased for the defocused position of the crystal because of the larger area of the DC component of the signal beam [43].

The crystal is not anti-reflection coated. Because of the relatively high refractive index of the $LiNbO_3$ ($n_o = 2.3$ at $\lambda = 532$ nm and $T = 20$ºC) the Fresnel reflections from the surfaces of the crystal inside and outside of the crystal are significant. The reflections inside the crystal can interfere with each other and their interference adds noise to the

final image of the bit pattern at the camera. To alleviate this effect, the crystal has been rotated about the *y*-axis in Figure 40 whereby the normal axis to the entrance facet of the crystal makes an angle of about 5º with respect to the *z*-axis. Therefore, the reflections inside the crystal have less overlap and make less interference.

5.4.4 Sensitizing Configuration

The UV illumination configuration is shown in a larger sketch in Figure 41. The configuration is designed to have the crystal sensitized by the UV beam as symmetrically as possible. The doubly doped $LiNbO_3$:Fe:Mn crystal is quite absorptive at UV wavelength range and the sensitizing beam does not penetrate much into the crystal [29, 30]. With this configuration, the crystal received UV illumination at the front and rear facets with respect to the signal beam direction to increase the effective thickness of the sensitized region and increase the *M*/# accordingly.

The symmetry of the sensitizing illumination helps recording holograms with high fidelity that more accurately resemble the interference fringes associated with the bit patterns. The Fresnel reflections from the crystal facets are significant as the refractive index of $LiNbO_3$ is relatively large and the UV beams are illuminated obliquely. Using mirrors the reflected UV beams from the crystal are reflected back to the crystal almost at the same angle as reflected to the mirrors. The back reflections increase the efficiency of the sensitizing as well by utilizing the reflected power. The reflected beams, as expected, are not as intense as the incident beams. Nonetheless, considering the space limitations in the setup, the symmetry of the UV illumination is reasonable.

As shown in Figure 40, the UV beam emitted from the UV laser is spatial filtered and expanded by a spatial filter. As mentioned in Section 5.4.3, a sharply nonuniform

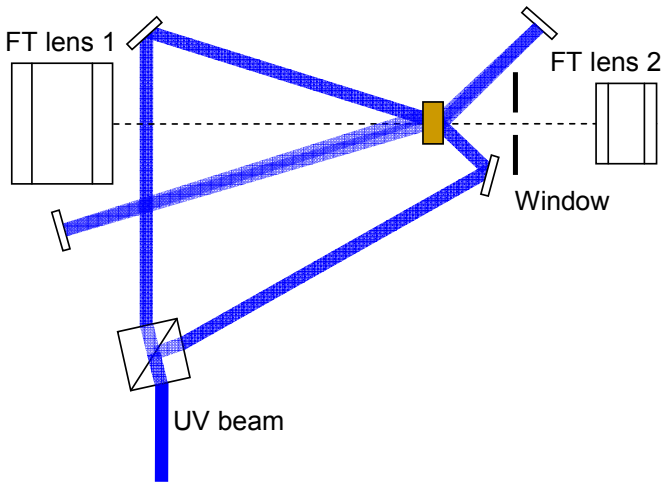

Figure 41. UV illumination configuration.

illumination with high photon energy to excite electrons from Mn centers can produce refractive index nonuniformity within the illuminated volume of the crystal. This effect occurs during sensitizing by sharp UV illumination as well. In a doubly doped $LiNbO_3$:Fe:Mn crystal illuminated by a sharp UV beam for a few minutes, the refractive index nonuniformity is quite visible in the form of wrinkles at the illumination spot by naked eye. The build up of index nonuniformity severely distorts the bit pattern image and degrades the SNR of the imaging. This effect becomes more substantial when the bit patterns are of high resolution with fine pixel size. By spatial filtering of the UV beam and expanding it, the fluctuations of the UV beam profile are minimized, resulting in rather uniform refractive index throughout the sensitized volume of the crystal.

5.4.5 Reference Beam Steering Mechanism

A 4-f system is usually used for rotating a plane wave reference beam in angular multiplexing [37]. The reference beam is focused by the first lens of the 4-f system and is again collimated by the second lens. The two lenses in the 4-f system are required to be

carefully designed to maintain the reference beam as a plane wave, since the lens aberrations can distort the reference beam specifically in the regions farther from the lens center. Moreover, the angular range of a 4-f system is limited by the NA of its lenses.

For the implemented holographic memory system, a beam steering configuration has been designed that does not have any lens. Figure 42 shows how the configuration is implemented. The reference beam is cropped with an iris with 3.5 mm of diameter. A rotation stage is placed on the other side of the crystal versus the reference beam side and is connected by a post to a flat mirror (M1), which steers the reference beam toward the crystal. The use of flat mirrors instead of lenses intrinsically maintains the plane wave form of the reference beam. The connecting steel is relatively long and might cause instability in recording due to undamped vibration. Therefore, the post is held by a long post holder that damps the vibrations of the rod. In a more practical design, a sliding

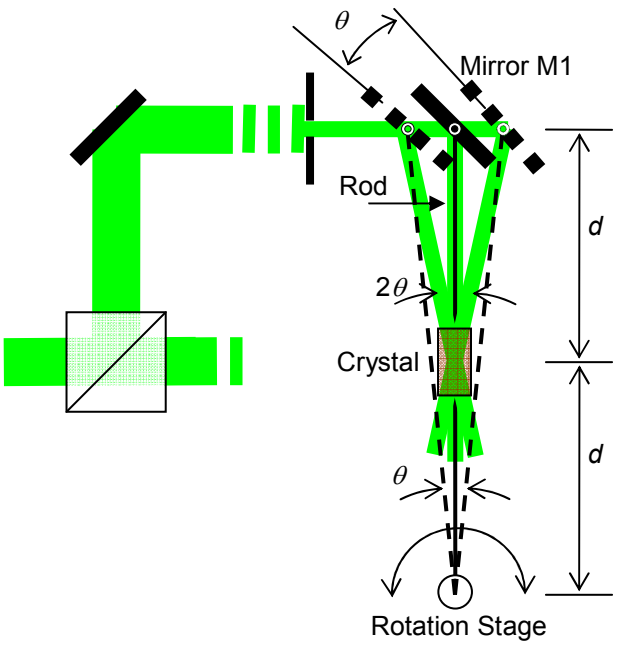

Figure 42. Beam steering configuration for the reference beam

mechanism beneath the mirror can be devised, on which the mirror lays and its vibration is rapidly damped.

The distance between the mirror M1 and the rotation axis, is twice the distance between the mirror and the center of the crystal. As a result, for small rotation angles, the rotation axis of the reference beam passes through the center of the crystal and its rotation angle is twice the rotation angle of the stage, which is the rotation angle of the mirror too. As experimented, the position of the 3.5 mm diameter reference beam completely remains on the side facet of the crystal, where the reference beam enters the crystal, as the beam angle varies within ±5º of angular range (i.e., the rotation stage rotates in a ±2.5º of angular range). The width of the side facet (i.e., the crystal thickness) is 4 mm.

5.4.6 Protection Cover

The use of a cover prevents the air flow around the setup as well as keeping the setup free of dust. Having no air flow greatly stabilizes the air temperature and refractive index as well as the temperature of the system components. This is an essential requirement for fixing the recorded interference pattern within the recording medium for long time hologram recordings. Some equipment can be added to the cover such as a high efficiency particulate air (HEPA) filtration system that can maintain the air inside the cover dust free. The air filtration systems involve vacuum pumping of the air, therefore, they have to be switched off before the recording and reading processes start with enough time allowance.

5.5 Capacity Estimation

To determine how many holograms can potentially be multiplexed using the acquired reference angular range (i.e., 10º as explained in Section 5.4.5) the angular selectivity of the system is calculated [43,57]:

$$\Delta\theta = \frac{\lambda}{L} = \frac{0.532\ \mu\text{m}}{4000\ \mu\text{m}} = 1.33\times10^{-4}\,\text{Rad} = 0.00762^\circ, \tag{22}$$

where $\Delta\theta$ is the reference angle with respect to the normal axis of the crystal side facet, and L is the crystal thickness. Therefore, if the reference beam is rotated by the angular selectivity for multiplexing each hologram (i.e., recording each hologram at the first null of the angular selectivity sinc curve of the previously recorded hologram [58]), then the possible number of multiplexed holograms is:

$$N = \frac{10^\circ}{0.00762^\circ} = 1312. \tag{23}$$

To examine whether the predicted capacity in Equation (23) is realizable, the dynamic range model [41] is used to evaluate the capacity of the system. According to Ref. [45], the dynamic range (M/#) of a doubly doped $LiNbO_3$:Fe:Mn crystal with the same dopant concentrations as used in this research and similar oxidation / reduction status is about 0.3 for 0.85 mm thickness. In Ref. [45], the transmission geometry is used and similar to the LHC, the recording beams wavelength is 532 nm and the recording beams are ordinary polarized. Based on the dynamic range finding in Ref. [45], the dynamic range for recoding in a 4 mm thick crystal in 90-degree geometry is calculated as follows: The M/# is given by

$$M/\# = \beta A_0(\tau_{e2}/\tau_r), \tag{24}$$

where β^2, the persistence, is defined as the ratio between the diffraction efficiency after sufficient readout and the maximum diffraction efficiency immediately after recording [46,48], $(A_0)^2$ is the maximum diffraction efficiency immediately after recording, and τ_{e2} and τ_r are the long erasure and recording time constants, respectively, as defined in Section 4.5.1 in Chapter 4. In transmission geometry, A_0 is proportional to the hologram thickness L_T [5]. Whereas in 90-degree geometry, A_0 is proportional to $(W.L_{90})^{1/2}$, where W is the width of the hologram is the direction of the reference beam [43]. The subscripts T and 90 represent the transmission and 90-degree geometries, respectively. The two proportionality constants for the transmission and 90-degree geometries are approximated the same. The width of the hologram can be estimated by the width of the Fourier transform pattern at the Fourier plane [59] assuming that it does not change much at the defocused position of the crystal:

$$W = 2 \times \frac{\lambda f_{\mathrm{FT1}}}{\delta} = 2 \times \frac{0.532 \ \mu\mathrm{m} \times 120 \ \mathrm{mm}}{28 \ \mu\mathrm{m}} = 4.56 \ \mathrm{mm}, \tag{35}$$

where δ is the pattern pixel pitch as explained in Section 5.4.2.

Assuming the parameters β, τ_{e2}, and τ_r the same for the transmission and 90-degree geometries, the dynamic range of the 4 mm thick crystal in 90-degree geometry is calculated based on the dynamic range of the 0.85 mm thick crystal in transmission geometry:

$$M/\#_{90} = M/\#_{\mathrm{T}} \frac{\sqrt{W.L_{90}}}{L_T} = 0.3 \times \frac{\sqrt{4.56 \times 4}}{0.85} = 1.5 \tag{26}$$

In both Equations (22) and (26) it is assumed that the multiplexed holograms in the 4 mm thick crystal use the entire thickness of the recording medium with uniform

hologram strength. It should be noted, however, that because of the rapid absorption of the sensitizing beam in the doubly doped photorefractive crystal, the effective thickness of the holograms is less than the physical thickness of the crystal [29,30]. Also, where the sensitizing light is present, the recording beams are subject to absorption as well. This effect reduces the effective thickness too. It is implied that the effective $\Delta\theta$ is larger than 0.00762º as calculated in Equation (22), leading to less angular selectivity. Also, the effective dynamic range is less than the value calculated in Equation (26). In fact, the absorption issue is more significant in two-center recording because of the absorption of the sensitizing and the recording beams together [29,30], resulting in smaller effective thickness of the two-center recorded holograms.

The final diffraction efficiency of the multiplexed holograms using angular multiplexing is calculated as $\eta = (M/\# / M)^2$ [13,46]. Considering a final diffraction efficiency of $\eta = 10^{-4}$ for each of the multiplexed holograms, the number of the multiplexed holograms in 90-degree geometry becomes:

$$M = \frac{M/\#_{90}}{\sqrt{\eta}} = \frac{1.5}{\sqrt{10^{-4}}} = 150\,. \tag{27}$$

Comparing Equations (22) and (27), it is observed that the angular range of the implemented beam steering allows for about 9 times more multiplexed holograms than the multiplexing limit applied by the dynamic range of the crystal. Moreover, as mentioned above, the effective dynamic range value for the 4 mm thick crystal is even less than the calculated value in Equation (26). Therefore, the possible number of multiplexed holograms is less than 150. It is inferred that the capacity is limited by the dynamic range of the recording medium rather than by the geometrical parameters of the

system such as angular selectivity. This implication is generally correct for the holographic multiplexing methods such as angular multiplexing in the photorefractive crystals, which involve sharing the entire volume of the recording medium among the multiplexed holograms.

5.6 Pixel Matching Experiments

In this section, the experimental results of the pixel matching of the SLM bit pattern with the camera using the implemented 4-f imaging system are presented. In all these experiments, the signal beam has been traveled through the holographic crystal. A conventional normalization technique for reducing the diffraction and interference fringes is explained. A new method for the image normalization is introduced that offers complete elimination of the diffraction and interference fringes from high resolution bit pattern images and significantly reduces the random speckles. The conventional and new normalization methods are compared. After the normalization, the data per each holographic channel is extracted from the oversampled bit pattern image.[1] The imperfections of the high resolution imaging, such as demagnification error and optical distortion, are handled using a simple method for data detection, resulting in accurate pixel matching of the SLM and camera.

5.6.1 Blank Image Normalization

The fringes and intensity nonuniformities of the coherent images can be alleviated by normalization techniques. One straightforward method to obtain a normalization base is to have an all-bright pattern on the SLM (i.e., all the SLM pixels transmitting with largest

[1] Refer to Section 5.4.2 for oversampling definition.

brightness), which is called the blank pattern, and capture its image on the camera thorough the holographic imaging system [43]. Hereinafter, the normalization with the blank pattern is referred to as the blank normalization. The acquired image has most of the intensity nonuniformities such as the curvature of the Gaussian intensity profile of the illuminating beam and the fringes that are commonly present in the bit pattern images. By dividing the pixel intensity values of the bit pattern images to the pixel intensity values of the normalization base image, most of the mentioned irregularities are removed from the bit pattern images, leaving an image with the pixel intensity values in the same range as the pixel intensity values of the bit pattern at the SLM. In other words, the normalization process yields narrower peaks in the histogram of the bit pattern image, which results is the improvement of the SNR of the system, as explained in Section 5.1.

For high resolution bit pattern images, however, not all the common intensity nonuniformities are eliminated by the blank normalization. As experimented, after applying the blank normalization a trace of the fringes still can be easily seen in high resolution random bit pattern images. A quantitative explanation is given for this effect in Appendix B.

5.6.2 New Image Normalization Method

The new normalization method is based on creating a specific normalization base for every bit pattern to be recorded. The following steps are performed to produce a new type of normalization base:

1. Figure 43(a) shows the image of the bit pattern. The interference and diffraction fringes and the illumination intensity nonuniformities are apparent. The concentric circular fringes are due to the interference of the reflections inside the

photorefractive crystal. That the center of the circles is on the right edge of the image is because of the deliberate rotation of the crystal from its perfectly aligned orientation, as discussed in Section 5.4.3. It has been observed that when the crystal is perfectly aligned, pixels in the center of the image are quite blurred.

2. The bit pattern on the SLM is inverted, swapping the bright pixels with the dark pixels and vice versa. The new image is the complement of the original bit pattern to be recorded. With the exact same illumination power, the image of the complement pattern is captured by the camera, referred to as the complement image. The complement image is shown in Figure 43(b). The same fringes and illumination nonuniformities as in Figure 43(a) are observed in the complement image as well.

3. The pixel intensity values of the original and complement images are added together pixel by pixel. The resultant image shown in Figure 43(c) is the desired normalization base.

The dark and bright pixels of the original bit pattern image shown in Figure 43(a) are removed from the normalization base. All the interference and diffraction fringes and the illumination nonuniformities are quite visible in Figure 43(c). A few circular diffraction patterns due to dust particles and the defects of the optical surfaces are observed, which are much better revealed in the normalization base than in the bit pattern images.

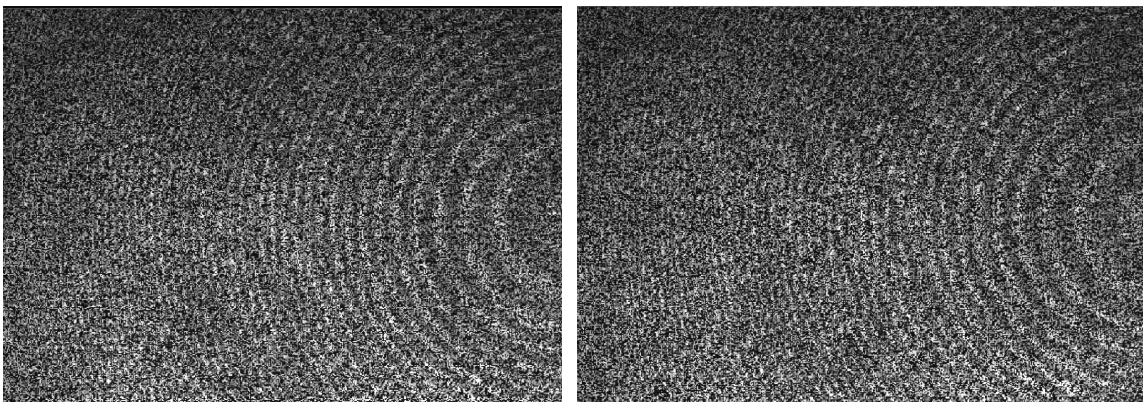

(a) (b)

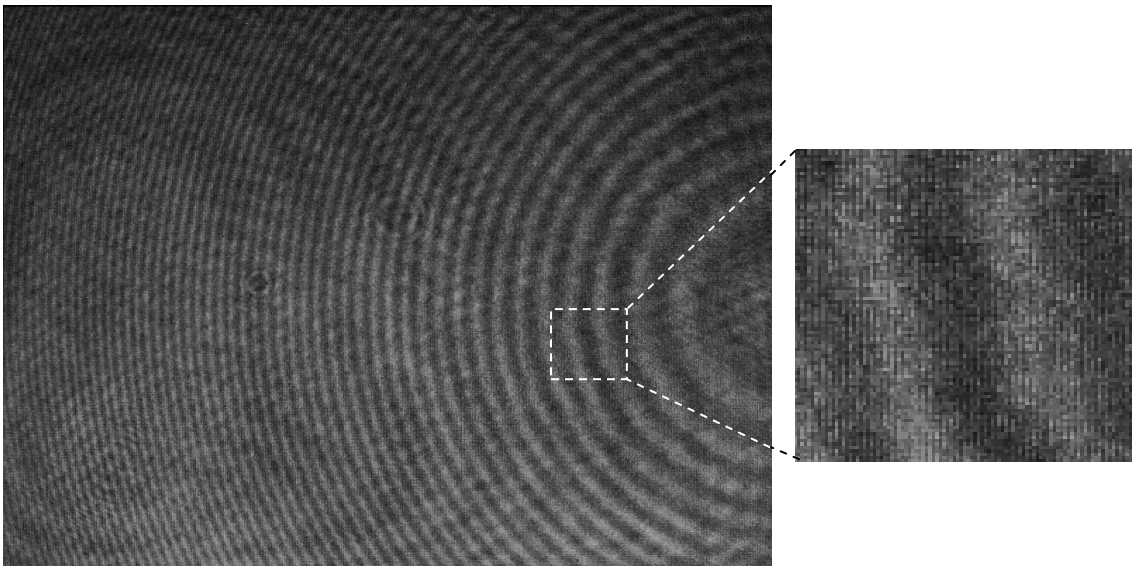

(c)

Figure 43. Steps to produce the normalization base for coherent image normalization. The resolution in all the images is 1024 × 768. The bit pattern on the SLM is oversampled by 2 × 2 superpixels. (a) Image of the original bit pattern is captured. (b) Image of the inverted bit pattern is captured. (c) The images of the original and inverted patterns are added together pixel by pixel. The resultant is the new type normalization base. The texture of the resultant normalization base is visible in the magnified figure.

A small portion of the normalization base image is magnified, in which the texture of the normalization base is visible. This texture is the unique feature of the new normalization base and is specific for every bit pattern originating the normalization base. As experimented, this texture is stationary and is not visible in the image of the blank pattern. As it will be discussed in Appendix B, the texture appeared in the new normalization base is primarily attributed to the speckle pattern due to the scattering noise produced specifically by each bit pattern on the SLM.

For the normalization, the pixel intensity values of the bit pattern image in Figure 43(a) are divided by those of the normalization base in Figure 43(c) pixel by pixel. The normalized image is shown in Figure 44. As observed, the diffraction and interference fringes are totally eliminated with no visible trace and the average intensity all over the image is uniform. Furthermore, a major portion of the speckles are removed by the introduced normalization. The speckle reduction property of the introduced normalization method will be experimentally and quantitatively demonstrated in Section 5.6.4 and Appendix B, respectively.

As explained above, it is required to have the images of the original and the complement bit patterns to create the specific normalization base for each bit pattern. Therefore, during the holographic reconstruction of the bit pattern images, it becomes necessary to have the original and the complement images for the normalization. Thus, there will be required to record two holograms per each bit pattern, which halves the capacity and the data retrieving speed at the same time. The SNR improvement with the new normalization method is not enough to compensate for the capacity and data rate loss. However, it is possible to perform the normalization during the recording by

precompensation of the fringes and the speckles in the recorded bit pattern and only record the precompensated bit pattern once [60]. For the precompensation, the images of the original and complement bit patterns are captured before the recording, then the normalization base is created through the steps mentioned above, and then the original pattern is normalized to the normalization base. The normalized bit pattern is put on the SLM for the recording.

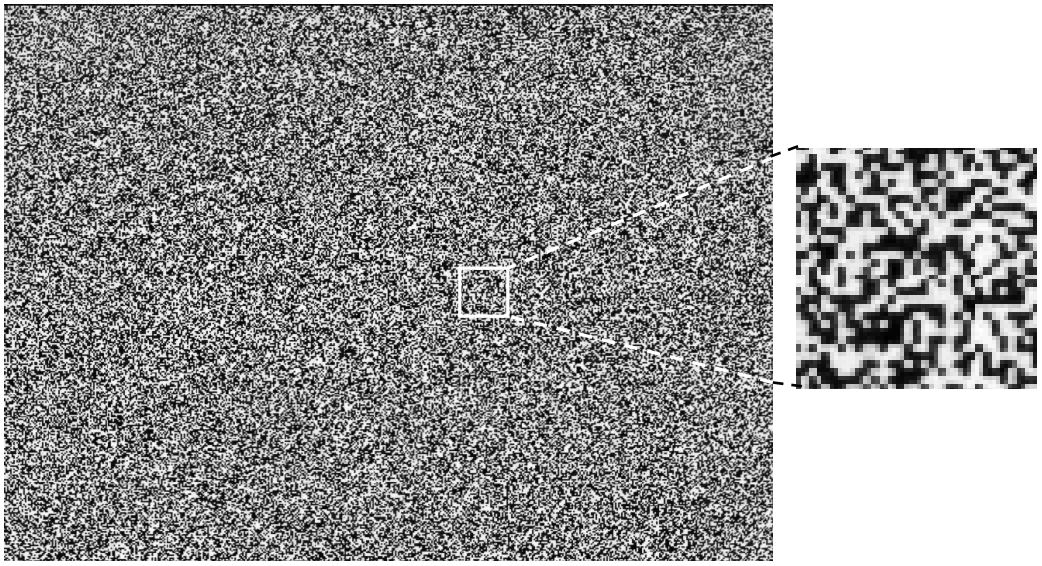

Figure 44. Normalized image of the bit pattern. The image resolution is 1024 × 768. The bit pattern on the SLM is oversampled by 2 × 2 superpixels. The diffraction and interference fringes are completely eliminated. The average intensity all over the image is uniform.

5.6.3 Pixel Matching Results

For the pixel matching of the SLM and the camera, the 2D bit pattern on the SLM has been imaged onto the camera by means of a 4-f imaging system with a demagnification error of 0.05%, as explained in Section 5.4.2. Figure 45(a) schematically shows the effect

of the demagnification error on the pixel matching. Over each pixel row of a bit pattern image with 1024 pixels, if at one end the image and camera pixels are perfectly matched then at the other end the pixels are mismatched by half a pixel because of the demagnification error. The deviation along the columns is less than half a pixel as the height of the bit patterns is 768 pixels, which is 25% less than the width of the bit patterns.

The alignments of the lens pairs for each of the Fourier transform lens assemblies have been examined by the autocollimator as well. The measurements confirm 5 arc minutes and 1 arc minutes of misalignment of the lenses for the front (FT lens 1) and rear (FT lens 2) Fourier transform lens assemblies, respectively. The effect of the lens misalignment can appear as the tilt of the rows and/or columns of the bit pattern image with respect to the rows and columns of the camera detector array. As observed in the implemented system, there is a small tilt of the image columns versus the columns of the camera 2D pixel arrays by which the image pixels are gradually shifted to the right by about half a pixel. The tilt effect is schematically shown in Figure 45(b).

The combination of the demagnification deviation and the tilt effects is schematically shown in Figure 45(c). The pixels at the center of the SLM image and the camera sensor are perfectly matched by lateral shift of the camera. It is observed that no significant pixel mismatch occurs in the vertical direction. However, the horizontal pixel mismatch becomes significant in some sections of the image because of the tilt of the image columns.

Because the bit patterns are oversampled with 2×2 pixel blocks as explained in Section 5.4.2, the normalized bit pattern images are first downsampled to extract the

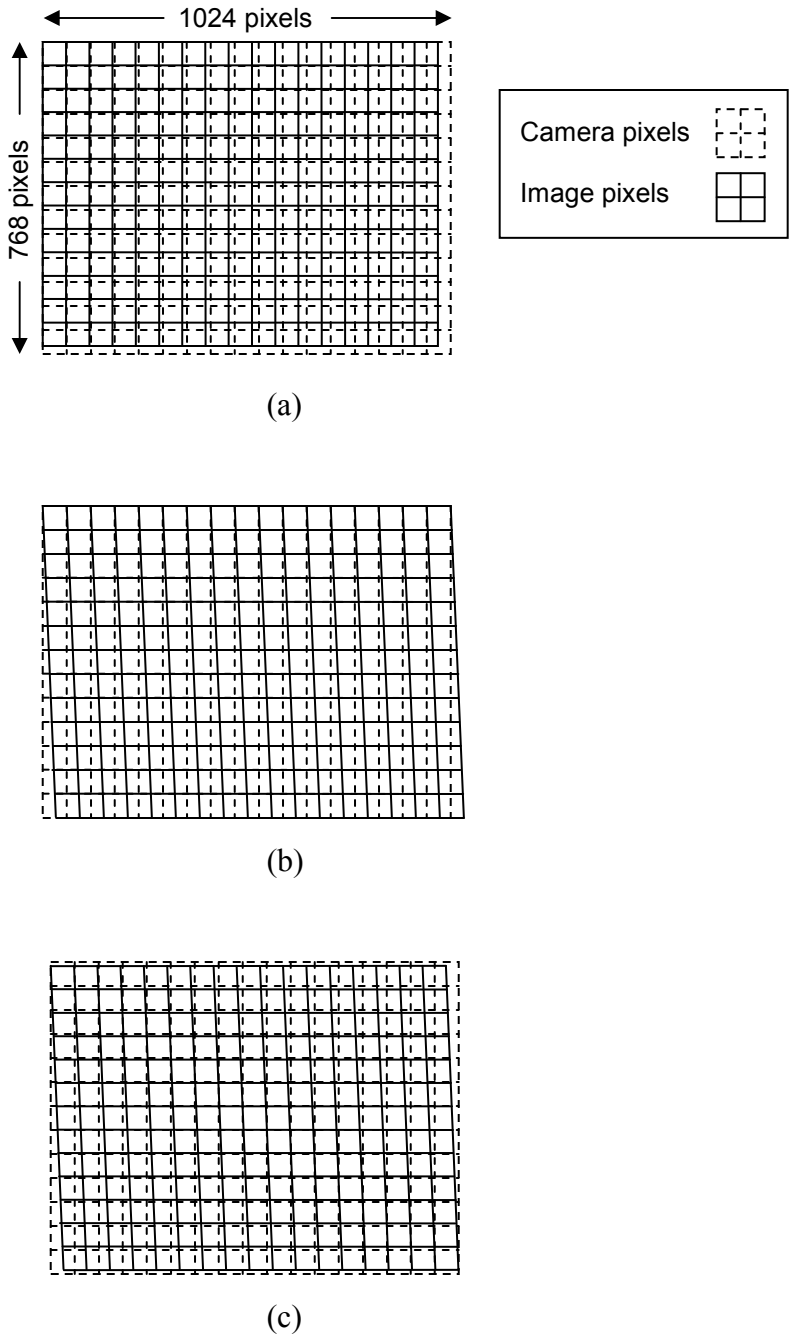

Figure 45. Pixel mismatch due to demagnification error and optical distortion. (a) The demagnification ratio is deviated by 0.05% resulting in varying pixel misregistration over the area of the image. (b) Because of optical distortion the image pixel columns are tilted versus the camera pixel columns. When the pixels at the top of the columns are perfectly matched, the pixels at the bottom of the columns are shifted by about half a pixel away from each other. (c) The demagnification deviation and the column tilt effects are combined. The pixels are perfectly matched at the center of the image, bit mismatched over the rest of the pattern.

intensity values received through each holographic channel. A simple downsampling method has been employed, with which the imaging imperfections as observed in Figure 45(c) are handled. Figure 46 shows how the downsampling is performed. The downsampling is carried out by averaging over one column of each 2×2 pixel block and the other column, which is the affected column due to pixel misregistration, is discarded. Whether the left column or right column of each pixel block is considered depends on the pixel misregistration direction at the coordinates of that pixel block. Figure 47 shows the areas in the bit pattern image where the left or right columns of the pixel blocks are chosen. The designation of the areas in Figure 47 follows the directions of the pixel misregistration at different areas of the bit pattern image, as observed in Figure 45(c).

The downsampled bit pattern image is shown in Figure 48. The good contrast of the normalized bit pattern image in Figure 44 has been preserved over the entire image area. In Figure 49, a few sections of Figure 48 have been zoomed in to better observe the contrast of the dark and bright pixels. In all the areas, the dark and bright pixels can be

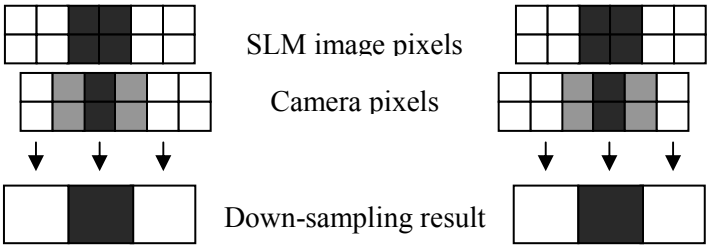

Figure 46. Downsampling method in the pixel misregistration condition (a) Right-shifted camera pixels versus the SLM image pixels. The left columns of the camera pixel blocks are kept. The right columns are affected by the neighbor pixels on the right side, hence discarded. (b) Left-shifted camera pixels versus the SLM image pixels. The right columns of the camera pixel blocks are kept. The left columns are affected by the neighbor pixels on the left side, hence discarded.

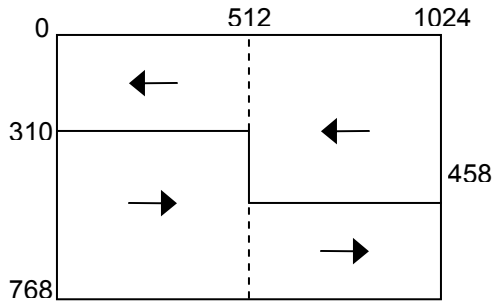

Figure 47. Downsampling of the bit pattern image by choosing left or right column of each 2 × 2 pixel block (see Figure 46). The bit pattern image is divided into two upper and lower areas. The arrows show whether the left or right columns of the pixel blocks are considered in the designated areas.

easily distinguished. Less contrast is observed in the upper zoomed sections. The reason is that the SLM illumination brightness has been smaller in the upper section of the SLM, which can be seen in Figure 43(a), resulting in less signal power in the darker areas. Therefore, the SNR has been poorer in the less illuminated areas of the SLM. It is implied that a more uniform illumination can improve the overall SNR of the data channels. Using beam shaping optics to convert the Gaussian beam to a beam with flat top intensity profile will result in uniform illumination of the SLM and larger data detection SNR.

5.6.4 Bit Pattern Image Histogram

The individual pixels in the downsampled bit pattern image (Figure 48) are associated with a holographic channel. The analog data received through each channel (i.e., the pixel intensity) has to be converted to digital data through a digital value assignment scheme, which is designed based on the raw SNR of the holographic channels. The histogram of the downsampled bit pattern image reveals the overall contributed noise to the received pixel intensities.

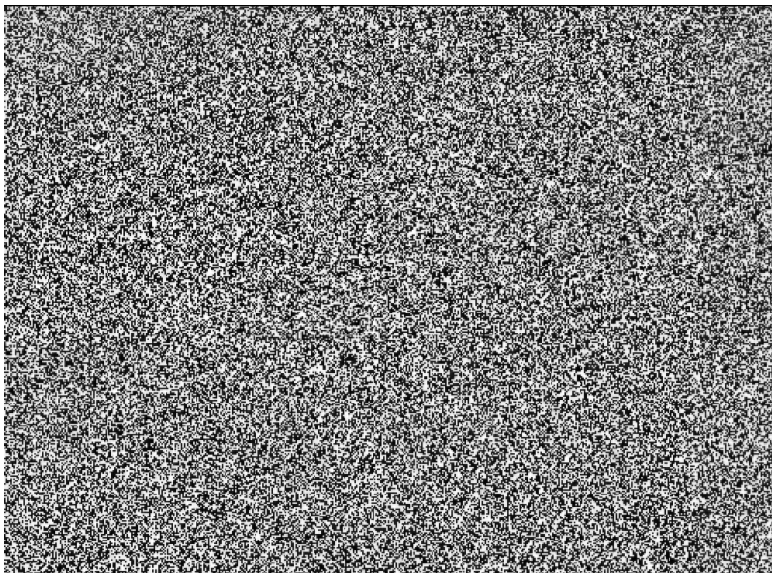

Figure 48. Downsampled image using the method explained in Figure 46. The image resolution is 512 × 384. The individual pixels represent the data channels.

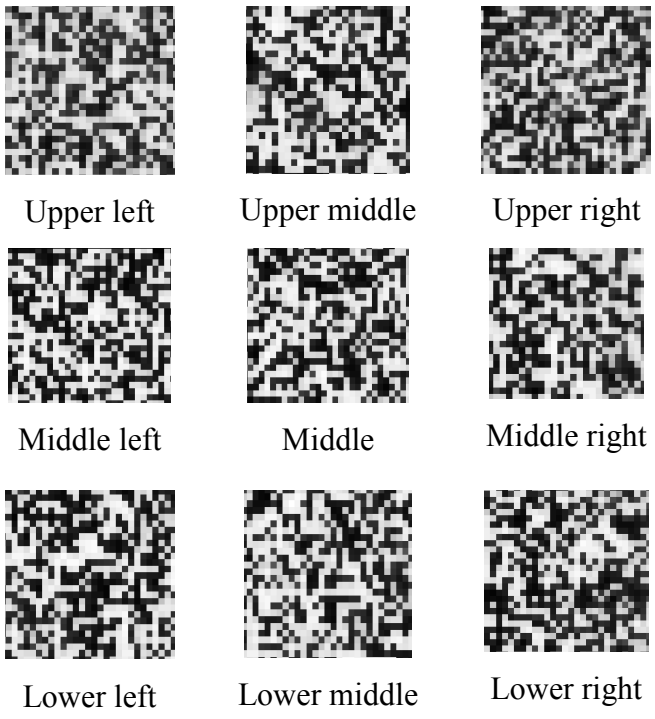

Figure 49. Zoomed parts of the downsampled image in Figure 48.

Figure 50 is the histogram of the entire bit pattern image in Figure 48. In the histogram, the two distributions corresponding to the dark and bright pixels are very well separated on the intensity scale with minimal overlap. It is observed that the dark and bright distributions are almost identical and resemble two identical Gaussian distributions. In the conventional holographic data storage systems, the intensity distribution of the holographic channels is Rician [61] rather than Gaussian. With Rician distribution, the variance of the intensity distributions of the bright pixels is larger than that of the dark pixels, which is due to the random phasor noise corresponding to the image speckles that is added to the complex field value at each pixel in the coherent imaging [61]. The larger intensity variance of the bright pixels increases the overlap of the dark and bright intensity distributions, leading to a larger BER. It is implied that a

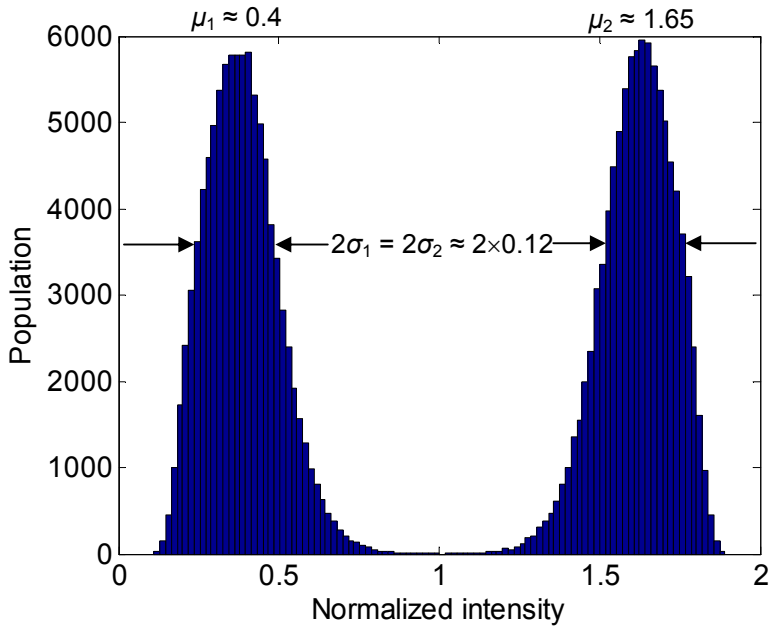

Figure 50. Histogram of the entire bit pattern in Figure 48. The pixel intensity values are normalized to the average pixel intensity. The estimated SNR is $|\mu_1 - \mu_2| / \sqrt{\sigma_1^2 + \sigma_2^2} = 7.4$.

major portion of the speckle noise is removed by the new normalization method explained in Section 5.6.2, resulting in a symmetric histogram with narrower intensity distribution for the bright pixels and less BER.

The estimated SNR measured as $|\mu_1 - \mu_2| / \sqrt{\sigma_1^2 + \sigma_2^2}$ is 7.4 for the entire image, where μ_i and σ_i are the mean and the standard deviation of the intensity distributions of the dark and bright pixels, respectively. This SNR is the largest reported for a holographic data storage system based on two-center recording along with the smallest image pixel size.[1] If the two intensity distributions are approximated with identical Gaussian distributions, then the raw BER estimated as the overlap of the areas under the two Gaussian curves is about 10^{-7} [43] for about 200,000 data channels per page. Typically, a raw BER of 10^{-5} to 10^{-4} is desired [62]. Even though the SNR is decreased by multiplexing more holograms, the initial achieved BER is small enough for the final BER levels of the multiplexed holograms being in the acceptable range.

Two experiments have been conducted to further explore the effectiveness of the new normalization method. In one experiment, a bit pattern image has been normalized by the new normalization base originated from another bit pattern. The two bit patterns have been fully uncorrelated. The resulting histogram of the downsampled bit pattern image shows a larger variance for the bright pixel intensities, which is similar to the Rician distribution. This confirms that the new normalization method is only efficient when the normalization base is specifically created for each bit pattern.

In another experiment, a bit pattern image has been normalized by the new normalization base originated from the same pattern, but the normalization base was low

[1] For comparison, refer to [48].

pass filtered by applying a 2 × 2 moving average block. The moving average filtering removes the texture of the normalization base[1] leaving an image that is very similar to the blank normalization base.[2] The resulting histogram of the downsampled bit pattern is similar to that from the previous experiment with larger variance of the bright pixel intensities. It is inferred that the new normalization base without its specific texture is not able to reduce the speckle noise of its associated bit pattern image. A quantitative explanation regarding the effect of the normalization base texture in the speckle reduction is given in Appendix B.

5.7 Hologram Multiplexing

The problems involved with two-center recording of holograms of high resolution patterns have been addressed. The refractive index fluctuations within the crystal volume produced by the nonuniformities of the UV (sensitizing) beam profile and tight focusing of the signal beam have been significantly reduced by spatial filtering of the UV beam and defocused recording, as explained in Sections 5.4.4 and 5.4.3, respectively. With the implemented holographic data storage system, it has been possible to multiplex 10 holograms. The reference beam has been rotated by 0.05º between each two recordings, which is 6.5 times the predicted angular selectivity of the system as calculated in Equation (22) to ensure minimal crosstalk in reading the multiplexed holograms. The intensities of the signal, reference, and sensitizing beams have been 20 mW/cm^2, 20 mW/cm^2, and 30 mW/cm^2, respectively. All the holograms have been recorded for 10 minutes and read for 15 minutes once all the holograms have been recorded.

[1] Refer to Figure 43(c) for the texture of the normalization base.
[2] Refer to Section 5.6.1 for the blank normalization.

5.7.1 Instability Problem

The reconstructed bit pattern images from most of the multiplexed holograms show promising contrast as the initial multiplexing results. However, they are not as high contrast as the bit pattern image as shown in Figure 43(a), though for a small number of multiplexed holograms, the same quality of the reconstructed images as that of the direct image is expected [43. 48]. This has been attributed to the slow recording and instability of the recording system, as the noise gratings continue to randomly build up despite the desired hologram failing to strengthen monotonically. As explained in Section 5.4.2, among many diffraction orders of the SLM, only the zeroth order is recorded and the others are blocked, resulting in low power efficiency of the recording system. Therefore, despite of using the maximum power of the green laser (5 Watts) the recording beam intensities are small, compared with the intensity levels acquired when a simple pixelated mask was used in the demonstration of the LHC.[1] The low recording beam intensities lead to slow hologram recording. Therefore, for a hologram to be recorded to its saturation strength the recording time can be as long as two hours. Similar to the multiplexing procedure for the localized holograms presented in Section 4.5 in Chapter 4, it has been intended to calculate a recording time schedule for the multiplexing with recording one strong hologram to its saturation strength and erasing it.

For long recording times, maintaining the stability of the system and fixing the recorded interference fringes becomes quite challenging. As mentioned in Section 5.4.6, by use of a protection cover it has been attempted to block the air flow that might have caused refractive index variations. Also, the temperature inside the lab and under the

[1] Refer to Section 3.2 in Chapter 3 and Section 4.4 in Chapter 4.

protection cover has been stabilized by turning on the laser several hours before the recording. The final instability source has been the green laser itself. The variation of the emitted wavelength of the laser has been confirmed using a Mickelson interferometer and observing the movement of the produced fringes. In the following, two modifications to address the instability issue are proposed. With the stability improvement of the recording system, multiplexing of about 100 holograms with acceptable raw BER of the retrieved bit patterns is envisioned, based on the *M*/# estimation given in Section 5.5.

5.7.2 Reflection Micromirror SLM

The transmissive SLMs, specifically the ones with higher resolutions and smaller pixel sizes, have much less pixel fill factor and transmission efficiency, which greatly decrease the effective power of the signal beam. For example, DLP micromirror SLM from Texas Instruments provides about 90% pixel fill factor and 68% reflection efficiency [63]. The transmissive SLM used in this research has a pixel fill factor of 40% and its transmission efficiency is 20% [56]. By using larger fill factor, the number of the diffraction orders emitted from the SLM is greatly reduced, leading to larger power efficiency. The large reflection efficiency of the SLM further increases the intensity of the signal power.

5.7.3 Fringe Locking Mechanism

With a fringe locker, the system becomes much more stabilized versus variations such as the laser instability, temperature change, air flow, and mechanical vibrations [31]. Most of the fringe lockers work based on the parallel interference of collimated beams. Therefore, a portion of the signal beam has to be diverted to the fringe locker before the beam strikes the SLM. Also, it is difficult to use the rotating part of the reference beam in

the fringe locker. Therefore, the required reference beam for the fringe locker should be sampled from the fixed part of the reference beam. Sampling from the signal and reference may exclude some components of the recording system from the stabilization. Nonetheless, it will be still very useful as some of the variations such as laser instability and temperature change will be greatly compensated.

5.8 Discussion

The holographic data storage system developed in this research offers multiplexing persistent holograms with erasure capability. In this system, all the multiplexed holograms overlap in the same volume of the recording medium. As such, it is not possible to erase and re-record individual holograms without affecting the other multiplexed hologram, unless the entire database is refreshed afterwards. Moreover, as predicted in Section 5.5, the storage density of a holographic data storage system with volume multiplexing is limited because of the diffraction efficiency degrading inversely proportional to square of the number of the multiplexed holograms ($1/M^2$; M: number of multiplexed holograms) [13]. The $1/M^2$ behavior of the diffraction efficiency is because of the erasure of the previously multiplexed holograms when a new hologram is recorded as all the holograms share the same medium volume. Finally, the large absorption of the sensitizing beam and the recording beams reduces the practical thickness of the recorded holograms, leading to storage density limitation.

All the above shortcomings can be addressed by adopting the localized recording technique[1] for developing holographic data storage systems, making them competitive read/write storage modules. The selective recording/erasure is the exclusive advantage of

[1] Refer to the previous chapters for localized recording.

localized recording, where the holograms are localized in separate thin slices of the recording medium. Hence, the erasure/re-recording of each hologram is dynamically performed without affecting the recorded holograms. Consequently, the mentioned $1/M^2$ behavior of the diffraction efficiency in volume multiplexing turns into a $1/M$ behavior in localized recording [35], leading to very large diffraction efficiency of the localized holograms. [1] Moreover, as the signal beam is only absorbed within the thin sensitized slice prepared for the recording, it can travel throughout the length of the recording medium without much absorption; hence, the crystal can be technically as lengthy as needed.

The existing data storage system with angular multiplexing can be transformed to employ the localized recording technique. Figure 51 shows the proposed configuration for the localized holographic memory (LHM). The optimized 4-f imaging system of the current system can remain intact with only changing the crystal with one suitable for the localized recording. A longer crystal for the LHM can be used to increase the system capacity. In that case, the Fourier plane of FT lens 1 is shifted farther from it. Therefore, FT lens 2 and the camera are accordingly shifted back farther from the crystal so the camera sensor is placed at the new image plane of the 4-f imaging system. The current reference and UV arms are removed. The new reference and UV arms are implemented in the exact same way as in the LHC.

In general, the number of localized holograms that can be recorded in a crystal is less than the number of holograms that can be volume multiplexed in the same crystal. This is because the localized slices cannot be thinner than a certain limit imposed by the

[1] Refer to Section 2.4.3 in Chapter 2 for the large diffraction efficiency of the localized holograms.

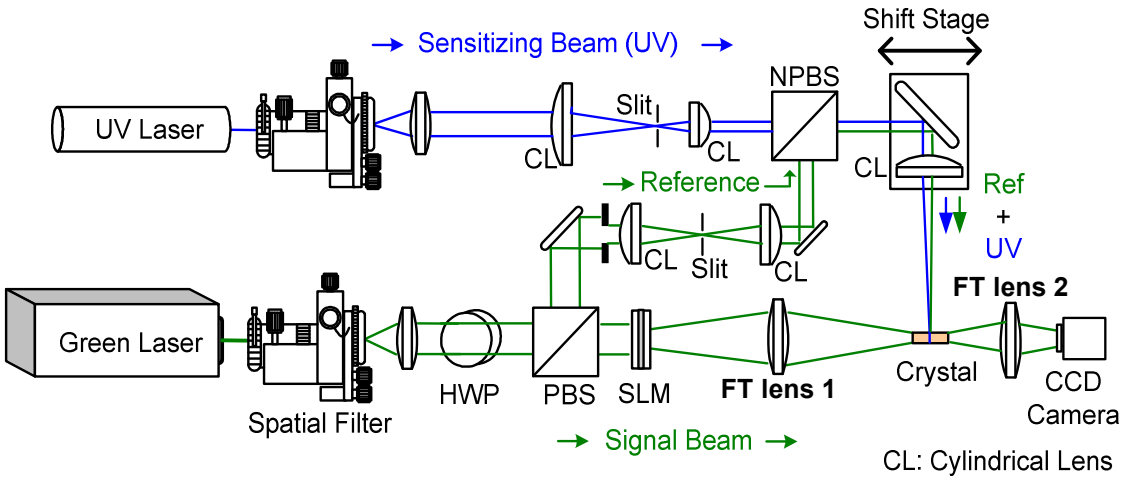

Figure 51. Holographic data storage with localized recording. HWP: half-wave plate, PBS: polarizing beamsplitter, NPBS: non-polarizing beamsplitter, FT: Fourier transform, CL: cylindrical lens, Pol: polarizer.

diffraction of the sensitizing and reference beams shaped as thin films that define the localized slices. As such, the number of localized slices per unit length of the recording medium is limited, which is potentially a major limit to the storage density of an LHM. In the work presented in Chapter 3 for the LHC, localized holograms as close as 33 μm to each other were demonstrated, resulting in 303 localized holograms per one centimeter of the recording medium. For comparison with the predicted capacity of 150 holograms for the angular multiplexing in a 4 mm thick crystal calculated in Equation (27), the possible number of localized holograms in 4 mm length of the crystal is 303 × 4 mm / 10 mm = 121.

On the other hand, the diffraction efficiency of the localized holograms is excessively large, leading to large SNR of the holographic data channels. This extra SNR can be employed to increase the storage density of the LHM through multilevel (M-ary)

data coding versus the conventional binary data coding. Thereby, the number of information bits per data channel can be increased. From the optics standpoint, the multilevel data coding is translated to gray level SLM pixels instead of only dark and bright pixels.

For large SNR of the holographic data channels, the storage density advantage of using M-ary data coding in LHM over the conventional binary data coding in the volume multiplexing systems has been theoretically demonstrated [52]. Therefore, it becomes necessary to improve the SNR of the data channels to take advantage of the M-ary data coding. As mentioned in Section 5.6.4, the histogram of the pixel matched image is 7.4, which is the best achieved among the holographic memories based on two-center recording. However, according to Ref. [52], to start benefiting from M-ary data coding, the SNR is required to be above 17 dB with the SNR definition in Ref. [52], which is equivalent to 16 with the SNR definition given in Section 5.6.4, assuming infinite contrast of the SLM. For the contrast of the SLM used in this research, which is about 4, the equivalent SNR is about 30. It seems that with the simple pixel matching procedure used in this research, these SNR levels are beyond reach.

More sophisticated data detection scheme, such as sequential [54] or parallel [64] algorithms can be employed for the data detection from the bit pattern images with pixel misregistration and inter-pixel crosstalk due to limited spatial bandwidth of the system. These algorithms significantly improve the SNR of the data channels, whereby the M-ary data coding becomes a practical way of improving the storage density of the LHM. In the cases of magnification ratio deviation and optical distortion, the misregistration is a

function of the pixel coordinates over the image area. The existing sequential and parallel algorithms can be adopted to compensate the variable misregistration.

The phase conjugate configuration is another way of improving the SNR of the data channels for the M-ary data coding, which is simply implemented in the LHM [48]. With the phase conjugate configuration, the aberrations of the imaging system and the distortions imposed by the crystal are eliminated and there is no need for sophisticated Fourier transform lenses. Moser, *et al.* showed the SNR improvement of using the phase conjugate method for binary data coding [48]. However, it should be noted that the reconstructed image produced by the phase conjugate method has the exact same size and pixel pitch as the bit pattern on the SLM. Thus, a demagnification imaging will be necessary to capture the image with a camera with smaller pixel pitch. Nonetheless, that the recording crystal is not in this imaging system is a notable advantage.

CHAPTER 6
CONCLUSION AND FUTURE WORK

6.1 Work Summary and Contributions

In this section, a summary of the achievements of this research is presented and the main contributions for the optical correlator and holographic data storage projects are reviewed.

6.1.1 Optical Correlation with Localized Holography

The capabilities of optical correlators are significantly extended using the localized recording technique in doubly doped photorefractive crystals. The localized recording is an example of the 90-degree geometry for the recording beams incident on two normal faces of the recording medium [37]. With this technique, the holograms are recorded within separate slices along the recording medium. The slices are defined with the reference and sensitizing beams shaped as thin films of light crossing the width of the recording medium where the signal and reference beams interfere and record a thin localized hologram.

The recording slices are physically separate along the recording medium, which enables the unique feature of selective recording/erasure of individual holograms in localized holography. Thereby, the patterns stored in the optical correlation system can be dynamically modified without affecting the entire stored pattern database. Moreover, using longer crystals it is possible to extend the capacity of the localized holographic correlators (LHCs). This is possible because the signal beam traveling along the crystal is

not absorbed except in the thin sensitized slices, as opposed to the major absorption of the beam in the conventional volume multiplexing methods. The physical separation of the holograms allows for placing a detector array right next to the recording medium for the detection of the diffraction signals. This way, the collecting lens and the required space for the diffracted signals to focus on the detector cells are eliminated and the optical correlator becomes more compact.

The performance of the LHC has been simulated for the crosstalk, shift invariance, and capacity. A theoretical comparison between the conventional angle-multiplexed optical correlator and the LHC shows that the LHC has higher capacity while the crosstalk in both methods is comparable and the shift invariance is the same. The trade-off between the LHC spatial bandwidth determined by the recording medium width, and the shift invariance has been identified and explained in detail.[1] By using the crystal width to record half of the pattern Fourier transform (i.e., shifted configuration versus symmetric configuration[2]) the spatial bandwidth of the LHC has been doubled without sacrificing the shift invariance.

The LHC has been experimentally demonstrated in the laboratory. Several persistent holograms have been recorded within separate slices as close as 33 μm apart along the crystal. To the best of the author's knowledge, the recorded localized holograms are the thinnest reported for localized holography. This has been made possible by 1D spatial filtering of the sensitizing and reference beams. The correlation capability, crosstalk, and shift invariance of the LHC have been measured and the results

[1] Refer to Section 2.4.2 in Chapter 2 for the detailed discussion.
[2] Refer to Section 2.3.1 in Chapter 2 for the shifted and symmetric configurations.

have been promising. The capability of dynamic content modification of the LHC has been experimentally verified.

6.1.2 Performance Enhancement of LHC

The physical separation of the localized holograms within the recording medium allows for much larger diffraction efficiency versus the volume multiplexed holograms recorded with conventional multiplexing methods. The excess of the diffraction efficiency allows for volume multiplexing of several holograms within each slice with sufficient diffraction efficiency. This multiplexing capacity has been utilized to enhance the performance of the LHC. The in-plane shift invariance and the rotation invariance of the LHC are improved by multiplexing several holograms from shifted and rotated versions of a 2D pattern within a slice of the recording medium. The reference beam has been intact during the multiplexing providing one specific diffracted signal per all different versions of each stored pattern.

Theoretical study of the multiplexing procedure for the in-plane shifted pattern is presented and the trade-off between the enhanced shift invariance and the spatial frequency bandwidth of the correlated 2D patterns is discussed. This trade-off exists because of the phase variation associated with the shifted configuration used to double the correlation spatial bandwidth. The associated phase variation leads to the phase mismatch among the diffraction signals from the multiplexed holograms within one slice that are recorded with the same reference beam.

The experimental results of the shift and rotation invariance enhancement are demonstrated. With an optimized recording schedule, the in-plane shift invariance of the LHC is improved by a factor of 9 by multiplexing 20 holograms originated from 20

shifted versions of the 2D pattern under correlation in one slice of the recording medium. By the same method, the rotation invariance of the LHC is enhanced by a factor of 8 by multiplexing 12 holograms from 12 rotated versions of the same pattern. There is a trade-off between the final diffraction efficiency and the invariance enhancement, which is due to the diffraction efficiency being inversely proportional to the square of the number of multiplexed holograms in volume multiplexing. Therefore, the desired level of diffraction efficiency determines the number of multiplexed hologram and the enhancement factor resulting from the multiplexing.

In an effort to extend the capabilities of the LHC for 3D object recognition, the 2D LHC experimental setup is transformed to a 3D object recognition system. With a localized hologram of a 3D object recorded, the rotation invariance of the 3D LHC has been measured, which shows a very narrow selectivity to the rotation of the object during the readout. The limitations of the LHC for 3D object recognition are investigated and the existing trade-off between the rotation invariance of the system and the spatial bandwidth is studied, which is similar to the existing trade-off between the shift invariance and the spatial bandwidth in the 2D LHC.

6.1.3 Holographic Data Storage with Two-Center Recording

A holographic data storage system based on two-center recording in a doubly doped $LiNbO_3$:Fe:Mn crystal with angular multiplexing capability is developed. The bit patterns used in this system have larger resolution (512 × 384) with finer pixel pitch (p = 28 μm × 28 μm using 2 × 2 SLM superpixels) compared to those used in the holographic memory

with two-center, localized recording demonstrated by C. Moser, *et al.*[1] Two Fourier transform lenses have been designed and fabricated that are used in a 4-f imaging system for imaging the SLM pattern onto the camera sensor array.

A simple beam steering mechanism for the reference beam rotation has been devised, whereby the lenses in a conventional 4-f system for the beam rotation are eliminated. The sensitizing UV beam in a two-center recording system can impose refractive index nonuniformities within the recording crystal volume when its intensity profile has sharp roughnesses. By performing spatial filtering to the UV beam and expanding it, this effect has been greatly alleviated leading to good fidelity of the recorded holograms. The spatial filtering of the UV beam becomes important when high resolution bit patterns are recorded and retrieved.

The effects involved with the coherent imaging of the bit pattern from the SLM to the camera, such as the speckling and the diffraction/interference fringes have been investigated. The presence of these effects adds a significant amount of noise to the image and complicates the data detection from the bit pattern images. With the conventional blank normalization of the images, the fringes are reduced and the SLM illumination nonuniformities are compensated. A novel normalization technique has been developed that completely eliminates the fringes and illumination irregularities and efficiently reduces the speckles as well, leading to larger SNR of the images. The normalization bases in the newly developed method are specific for every bit pattern and contain the particular speckle pattern produced by their associated bit pattern through the coherent imaging.

[1] Refer to Ref. [48].

Pixel matching has been performed between the bit pattern image pixels and the camera pixels for the entire area of the SLM image. Because of the imperfections in the imaging system components, there is a very small deviation in the demagnification ratio. Also, there is a slight optical distortion, because of which the SLM image is a little deviated from a perfect square grid. By taking advantage of the oversampling of the bit patterns (i.e., using 2×2 superpixels on the SLM and camera), a simple method has been developed, by which the oversampled bit pattern images are downsampled and the bit pattern data is efficiently detected.

The intensity histogram of the downsampled image shows a large separation between the dark and bright pixels on the intensity scale. The reduction of the speckle noise is evident in the histogram being symmetric, as opposed to the well known Rician distribution observed in the coherent image histograms in the conventional holographic data storage systems. The SNR of the entire image calculated as $|\mu_1 - \mu_2| / \sqrt{\sigma_1^2 + \sigma_2^2}$ is 7.4,[1] which is the largest reported for a holographic data storage system based on two-center recording with the smallest pixel size. The theoretically estimated raw BER based on the achieved SNR is about 10^{-7} [43] for about 200,000 data channels per page, which is much better than the typical raw BER ranging from 10^{-5} to 10^{-4} [62]. The estimated raw BER is small enough for the final BER levels being in the acceptable range for a large number of multiplexed holograms.

The optimized imaging system with the demonstrated pixel matching capability can be used to develop holographic data storage systems with other multiplexing schemes, such as localized holographic recording.

[1] Refer to Section 5.6.4 and Figure 50 for the histogram.

6.2 Future Directions

In this section, the envisioned tasks to improve the achievements of this research, the suggested approaches to realize practical devices based on this research, and the recommended solutions to some of the complications are outlined. The suggestions are presented separately for the optical correlator and holographic data storage projects.

6.2.1 Localized Holographic Correlator

- Using longer crystals to increase the capacity of the LHC. Because there is no major absorption for the signal beam propagating along the crystal in localized holography, the use of long crystals is possible.

- Using a detector array and placing it in close proximity of the crystal facet where the diffraction signals diffract out. This way the imaging lens in front of the CCD camera in Figure 14 in Chapter 3 is eliminated, which saves a large space and make the LHC much more compact.

- Eliminating the 4-f system for DC blocking. The DC blocking can be performed at the Fourier plane right in front of the crystal by attaching the DC blocking filter to the front facet of the crystal or placing a very small opaque spot on the font facet of the crystal, where the common DC component of the patterns occurs.

- Adding a red laser to address the broadening issue of re-recording. This is for the post treatment of the erased localized slices to avoid the broadening effect of the re-recorded holograms.[1] The red beam can overlap with the sensitizing and reference

[1] Refer to Section 3.5.2 in Chapter 3 for detailed discussion.

beams and can be a little defocused to be broader as needed for more uniform illumination.

- Automating the co-alignment of the reference and sensitizing beams. The reference and sensitizing beams always have to overlap inside the crystal. A feedback based system can be devised to maintain the co-alignment of the two beams by sensing their incidence locations on the detector array and correcting any misalignment by rotating mirrors M2 and M3 in Figure 14 in Chapter 3.

- Optimizing the thickness of the localized slices for specific applications. Larger slice thickness allows for more multiplexed holograms within each slice, leading to larger robustness improvement of the LHC. On the other hand, the number of stored patterns per unit length of the crystal will decrease for thicker slices. By designing the slice thickness the associated trade-off can be optimized for specific applications.

- Preconditioning the recorded and correlated patterns. Because the LHC is sensitive to the scale, shift, and rotation of the correlated patterns, the recorded and correlated images can be preconditioned before putting them on the SLM. Within specific classes of patterns to be recognized by the LHC (e.g., fingerprints), designing the preconditioning algorithms for having the patterns at the desired coordinates, scale, and orientation can be more straightforward. In general, integrating the LHC with an electronic pattern recognition system can greatly improve the performance of the system in terms of speed and capacity.

- Using a smaller object with larger features for the 3D object recognition using the LHC. The system will be less sensitive to the object rotation. Also, the object

illumination as shown in Figure 38 in Chapter 4 can be changed to make the illuminating beam as less diverging as possible, which helps improving the rotation invariance of the system. This is easier to accomplish for illuminating smaller objects.

6.2.2 Holographic Data Storage with Two-Center Recording

- Forming a beam with a flat top intensity profile using beam shaping optics. Using the conventional Gaussian beam for the illumination of the SLM imposes intensity variation over the recorded bit patterns, resulting in diffraction efficiency variation over the area of the bit pattern image. With a flat top beam, the diffraction efficiencies associated with all the bit pattern pixels will be about the same, leading to more uniform SNR over the bit pattern area.

- Design and fabrication of Fourier transform lenses with zooming capability, less aberration, and larger numerical aperture (NA). The zooming capability allows for accurate magnification adjustment, which considerably facilitates the pixel matching. Also, for accurate imaging of high resolution bit patterns with good contrast, it is important to have an imaging system with sufficient NA with as less aberration as possible.

- Using a reflection micromirror SLM instead of a transmissive SLM. A reflection micromirror SLM (e.g., DLP micromirror SLM from Texas Instruments) provides larger pixel fill factor that reduces the number of diffraction orders, and larger reflection efficiency. Therefore, the power efficiency of the holographic recording is greatly improved.

- Precompensation for the interference fringes and speckles in the bit patterns before the recording. Using the new normalization method introduced in Section 5.6.2 in Chapter 5, the bit patterns can be normalized before the recording. Therefore, the fringes and speckles associated with the coherent imaging of the patterns will be greatly reduced in the retrieved bit pattern images and there will be no need to record two holograms per bit pattern for the original and complement patterns.

- Implementing a holographic data storage system with localized recording. The unique feature of selective recording and erasure of the holograms can make the holographic data storage a competitive read/write storage device. Furthermore, the large diffraction efficiency of the localized hologram provides much larger SNR that can be utilized to encode the digital data sent through the holographic channels (i.e., pixels or pixel blocks) with multilevel (M-ary) data coding.

- Compensation for pixel misregistration and inter-pixel crosstalk with more advanced algorithms. Sequential or parallel algorithms can be utilized for the data detection from the bit pattern images with pixel misregistration and inter-pixel crosstalk due to limited spatial bandwidth of the system. Thereby, the SNR of the holographic data channels is significantly increased, and the storage density improvement with M-ary data coding becomes viable.

- Implementing the phase conjugate configuration with localized recording. The phase conjugate configuration eliminates the aberrations of the imaging system, leading to larger SNR of the system and larger capacity per channel.

APPENDIX A

DERIVATION OF FRESNEL DIFFRACTION FORMULA

In this Appendix the Fresnel diffraction formula is derived that relates the EM field within the recording slice volume [i.e., F(u,v,z)] to that at the SLM plane [i.e., f(ξ,η)] in Figure 7. For the simplicity of deriving the diffraction pattern in the recording medium, the front face of the recording medium is assumed to be at the Fourier plane of the lens. Because the height of the recording medium (L_X) in LHCs is relatively small (about 1mm), it is also important to couple most of the signal beam into the recording medium. Therefore, focusing the signal beam at the entrance of the recording medium is useful in that way as well. The EM field at the back focal plane of the lens (z = 0) is

$$\mathrm{H}(x,y) \propto FT\{\mathrm{f}(\xi,\eta)\} = \mathrm{G}\left(\frac{x}{\lambda F}, \frac{y}{\lambda F}\right) \tag{28}$$

where *FT* represents Fourier transformation, and the Fourier transform of the function f is represented by the function G. Afterwards, light propagates through the crystal with average refraction index of n. The Fresnel diffraction approximation is used to evaluate the EM field at any location within the recording medium with longitudinal distance z to the back focal plane of the lens. Moreover, it is assumed that the reflection coefficient at the boundary between air and the recording medium is constant within the whole spatial frequency spectrum of the signal beam. Assuming paraxial approximation and using the kernel of the Fresnel diffraction [59] yields

$$\mathrm{F}(u,v,z) \propto \left\{ H(x,y) \otimes \frac{1}{j\lambda z} \exp\left(j\frac{2\pi n z}{\lambda} \right) \exp\left[j\frac{n\pi}{\lambda z}\left(x^2 + y^2\right) \right] \right\}$$

$$= \left\{ \mathrm{G}\left(\frac{x}{\lambda F}, \frac{y}{\lambda F} \right) \otimes \frac{1}{j\lambda z} \exp\left(j \frac{2\pi n z}{\lambda} \right) \exp\left[j \frac{n\pi}{\lambda z} \left(x^2 + y^2 \right) \right] \right\}$$

$$= FT^{-1} \left\{ \mathrm{f}(-\xi, -\eta) \exp\left[-j \frac{\pi z}{n\lambda F^2} \left(\xi^2 + \eta^2 \right) \right] \right\} \frac{1}{j\lambda} \exp\left(j \frac{2\pi n z}{\lambda} \right), \quad (29)$$

where $\otimes$ stands for 2D convolution and FT^{-1} represents inverse Fourier transformation. Rewriting the FT^{-1} in its integral form and omitting the constant term of $1/j\lambda$ yields

$$\mathrm{F}(u, v, z) \propto \iint_{\mathrm{SLM}} \mathrm{f}(-\xi, -\eta) \exp\left[-j \frac{\pi z}{n\lambda F^2} \left(\xi^2 + \eta^2 \right) \right] \exp\left(j \frac{2\pi n z}{\lambda} \right) \exp\left[j \frac{2\pi}{\lambda F} \left(u\xi + v\eta \right) \right] \mathrm{d}\xi \, \mathrm{d}\eta \,. \quad (30)$$

By negating the variables ξ and η, the final form of the EM field within the recorded slice is obtained

$$\mathrm{F}(u, v, z) \propto \iint_{\mathrm{SLM}} \mathrm{f}(\xi, \eta) \exp\left[-j \frac{\pi z}{n\lambda F^2} \left(\xi^2 + \eta^2 \right) \right] \exp\left(j \frac{2\pi n z}{\lambda} \right) \exp\left[-j \frac{2\pi}{\lambda F} \left(u\xi + v\eta \right) \right] \mathrm{d}\xi \, \mathrm{d}\eta \,. \quad (31)$$

APPENDIX B

QUANTITATIVE COMPARISON OF NORMALIZATION METHODS

In this appendix, a mathematical comparison of the blank normalization and the newly developed normalization is presented. In a pixel matched coherent imaging system, for a specific SLM pixel in a typical bit pattern the received intensity at the associated camera pixel can be depicted as:

$$I_a = \left|a + f + \sigma\right|^2 + \delta^2, \tag{32}$$

where a is the SLM pixel amplitude, f is the added complex field value due to the fringes, σ is the stationary phasor noise, and δ^2 is the overall camera detector noise that is randomly time varying. The phasor noise at the image plane is due to any rough randomness of the phase distribution over the input field pattern [53,59], volume optical scatterings, or sharp roughnesses of the optical surfaces [61]. Therefore, it is a sophisticated, linear function of the input field pattern at the SLM. The image speckles are in fact produced by the phasor noise denoted by σ in Equation (32). The pixel amplitude is either 1 or 0, assuming infinite contrast of the SLM. The quantities $\left|f\right|, \left|\sigma\right|$, and δ^2 are assumed much smaller than unity. The proportionality constant in the relationship between the intensity and the magnitude squared of the field value is dropped. The first order approximation of Equation (32) based on the mentioned assumptions yields

$$I_a \approx \begin{cases} 1 + 2\,\mathrm{Re}\{f\} + 2\,\mathrm{Re}\{\sigma\} + \delta^2 & ; a = 1 \\ \delta^2 & ; a = 0 \end{cases}. \tag{33}$$

For a blank pattern with unity pixel amplitudes on the SLM, the received intensity at the same camera pixel as in Equation (32) is

$$I_b = \left|1 + \alpha f + \sigma_b\right|^2 + \delta_b^2 . \tag{34}$$

The subscript *b* denotes the blank normalization. The fringe pattern due to the diffractions and interferences retains its shape when the SLM pattern is changed from a typical bit pattern to a blank pattern. The reason is with a high resolution pattern on the SLM with small pixels, the dark and bright pixels are closely spaced. Thus, when a fringe pattern with much larger features than the pattern pixels is created, replacing the dark pixels with bright ones can be approximately interpreted as increasing the bright pixel intensities of the bit pattern leading to stronger fringes. The multiplier $\alpha > 1$ in Equation (34) denotes the increase of the fringe amplitude for an SLM blank pattern.

The phasor noise σ_b produced by the blank pattern is different than the phasor noise σ due to the bit pattern in Equation (32), because of the sophisticated dependence of the phasor noise to the SLM input field pattern, as mentioned in the beginning of this appendix. As it will be shown later in this chapter, the texture visible in the new normalization base as illustrated in Figure 43(c) is due to the phasor noise. That the texture is not obviously visible in the image of the blank pattern[1] implies small amplitude of σ_b compared to that of σ. The noise quantity δ_b^2 is uncorrelated with δ^2 in Equation (32) as it is a randomly time varying quantity. All the assumptions in Equation (33) are considered true for the fringe and noise quantities in Equation (34) as well. Therefore, the first order approximation of Equation (34) yields

[1] Refer to Section 5.6.2 in Chapter 5.

$$I_b \approx 1 + 2\alpha\,\mathrm{Re}\{f\} + 2\,\mathrm{Re}\{\sigma_b\} + \delta_b^2 . \tag{35}$$

Performing the blank normalization, Equation (33) is divided by Equation (35) to calculate the normalized pixel intensity:

$$I_n = \frac{I_a}{I_b} \approx \begin{cases} \dfrac{1 + 2\,\mathrm{Re}\{f\} + 2\,\mathrm{Re}\{\sigma\} + \delta^2}{1 + 2\alpha\,\mathrm{Re}\{f\} + 2\,\mathrm{Re}\{\sigma_b\} + \delta_b^2} & ; a = 1 \\ \dfrac{\delta^2}{1 + 2\alpha\,\mathrm{Re}\{f\} + 2\,\mathrm{Re}\{\sigma_b\} + \delta_b^2} & ; a = 0 \end{cases}$$

$$\approx \begin{cases} 1 - 2(\alpha - 1)\,\mathrm{Re}\{f\} + 2\,\mathrm{Re}\{\sigma - \sigma_b\} + \delta^2 - \delta_b^2 & ; a = 1 \\ \delta^2 & ; a = 0 \end{cases} . \tag{36}$$

It is notable in Equation (36) that for $\alpha > 1$, the fringes are still traceable in the normalized pattern. Also, the resultant phasor noise is not changed much because of the small amplitude of σ_b compared to that of σ as explained above. It is implied that the blank normalization may not yield much gain in the overall SNR of the system when high resolution bit patterns are used.

As for the new normalization method, the same assumptions as for the blank normalization are considered for the first order approximation of the pixel intensities received by the camera pixels. The pixel intensity for the original pattern is the same as depicted in Equation (33). For the complement pattern image, the received pixel intensity is

$$I'_a \approx \begin{cases} \delta'^2 & ; a = 1 \\ 1 + 2\,\mathrm{Re}\{f\} + 2\,\mathrm{Re}\{\sigma'\} + \delta'^2 & ; a = 0 \end{cases} . \tag{37}$$

where the SLM pixel field value *a* corresponds to the original pattern as in Equation (33). The prime notation in Equation (37) denotes differentiation with respect to the original

bit pattern. However, the fringe field value is the same as in Equation (33) for the original bit pattern. This is based on the assumption that the probabilities of the occurrences of dark and bright pixels in a typical bit pattern are equal at every location of the bit pattern. Therefore, the number of the bright pixels contributing to the creation of the fringes is the same for the original and complement bit patterns, resulting in the same fringe filed value at the image for both patterns. The summation of Equations (33) and (37) yields

$$I_m = I_a + I'_a \approx \begin{cases} 1 + 2\,\mathrm{Re}\{f\} + 2\,\mathrm{Re}\{\sigma\} + \delta^2 + \delta'^2 & ; a = 1 \\ 1 + 2\,\mathrm{Re}\{f\} + 2\,\mathrm{Re}\{\sigma'\} + \delta^2 + \delta'^2 & ; a = 0 \end{cases}, \tag{38}$$

which is the new normalization base. Comparing Equations (35) and (38) as the blank and new normalization bases, respectively, it is clear that the stationary terms of the two equations are differentiated by the phasor noise contributions and the fringe amplitude. As mentioned above, the stationary texture of the new normalization base in Figure 43(c) is not visible is the blank normalization base. It is deduced that the new normalization texture is produced by the phasor noise from the original and complement bit patterns. Also, the phasor noise from the blank pattern is negligible.

Performing the new normalization, Equation (33) is divided by Equation (38) to calculate the normalized pixel intensity:

$$I_n = \frac{I_a}{I_m} \approx \begin{cases} \dfrac{1 + 2\,\mathrm{Re}\{f\} + 2\,\mathrm{Re}\{\sigma\} + \delta^2}{1 + 2\,\mathrm{Re}\{f\} + 2\,\mathrm{Re}\{\sigma\} + \delta^2 + \delta'^2} & ; a = 1 \\ \dfrac{\delta^2}{1 + 2\,\mathrm{Re}\{f\} + 2\,\mathrm{Re}\{\sigma'\} + \delta^2 + \delta'^2} & ; a = 0 \end{cases}$$

$$\approx \begin{cases} 1 - \delta'^2 & ; a = 1 \\ \delta^2 & ; a = 0 \end{cases} \tag{39}$$

Comparing Equations (36) and (39) for the normalized bit patterns with the blank and new normalization methods, respectively, it is evident that in the new normalization method the fringes and the speckles due to the phasor noise are completely removed. Furthermore, the effect of the overall camera noise is reduced by half at the bright pixels. These equations have been derived based on infinite SLM contrast assumption. Nonetheless, it can be shown that for limited SLM contrast also the new normalization method reduces the fringes and speckles much more efficiently than the blank normalization does.

REFERENCES

[1] D. Gabor, "A new microscopic principle," *Nature*, vol. 161, pp. 777-778, May 1948.

[2] P. J. van Heerden, "Theory of optical information storage in solids," *Appl. Opt.*, vol. 2, pp. 393-400, Apr. 1963.

[3] D. Psaltis and F. Mok, "Holographic memory," *Sci Am*, vol. 273, pp. 70-76, Nov. 1995.

[4] J. Ashley, M.-P. Bernal, G. W. Burr, H. Coufal, H. Guenther, J. A. Hoffnagle, C. M. Jefferson, B. Marcus, R. M. Macfarlane, R. M. Shelby, and G. T. Sincerbox, "Holographic data storage," *IBM J. Res. Dev.*, vol. 44, pp. 341-368, May 2000.

[5] H. J. Coufal, D. Psaltis, and G. T. Sincerbox, Eds., *Holographic Data Storage*. Berlin: Springer-Verlag, 2000.

[6] J. Eickmans, T. Bieringer, S. Kostromine, H. Berneth, and R. Thoma, "Photoaddressable polymers: a new class of materials for optical data storage and holographic memories," *Jpn. J. Appl. Phys.*, vol. 38, pp. 1835-1836, March 1999.

[7] D. A. Waldman, H.-Y. S. Li, and E. A. Cetin, "Holographic recording properties in thick films of ULSH-500 photopolymer," *Proc. SPIE*, vol. 3291, pp. 89-103, June 1998.

[8] http://www.inphase-tech.com (Accessed March 12, 2008).

[9] A. B. VanderLugt, "Signal detection by complex spatial filtering," *IEEE Trans. Inf. Theory*, vol. IT-10, pp. 139-148, Apr. 1964.

[10] C. S. Weaver and J. W. Goodman, "A technique for optically convolving two functions," *Appl. Opt.*, vol. 5, pp. 248-1249, July 1966.

[11] T.-C. Poon and T. Kim, "Optical image recognition of three-dimensional objects," *Appl. Opt.*, vol. 38, pp. 370-381, Jan. 1999.

[12] S.-H. Shin and B. Javidi, "Three-dimensional object recognition by use of a photorefractive volume holographic processor," *Opt. Lett.*, vol. 26, pp. 1161-1163, Aug. 2001.

[13] D. Psaltis, D. Brady, and K. Wagner, "Adaptive optical networks using photorefractive crystals," *Appl. Opt.*, vol. 27, pp. 1752-1759, May 1988.

[14] A. Pu, R. Denkewalter, and D. Psaltis, "Real-time vehicle navigation using a holographic memory," *Opt. Eng.*, vol. 36, pp. 2737-2746, Oct. 1997.

[15] G. W. Burr, S. Kobras, H. Haussen, and H. Coufal, "Content-addressable data storage by use of volume holograms," *Appl. Opt.*, vol. 38, pp. 6779-6784, Nov. 1999.

[16] G. R. Mangasaryan, B. E. Khaikin, and V. S. Khitrova, "Matched filtering on basis of thick holograms for fingerprint identification," *Opt. Comm.*, vol. 22, pp. 169-172 Aug. 1977.

[17] A. M. Glass, D. von der Linde, and T. J. Negran, "High-voltage bulk photovoltaic effect and photorefractive process in $LiNbO_3$," *Appl. Phys. Lett.*, vol. 25, pp. 233-235, Aug. 1974.

[18] A. M. Glass, "The photorefractive effect," *Opt. Eng.*, vol. 17, pp. 470-479, Sep. 1978.

[19] A. Yariv, *Optical Electronics in Modern Communications*. 5th ed., New York: Oxford University Press, 1997.

[20] K. K. Wong, "Photorefractive effects in $LiNbO_3$," in *Properties of Lithium Niobate*, K. K. Wong, Ed., London: INSPEC, 2002, pp. 141-145.

[21] H. Kurz, E. Krätzia, W. Keune, H. Engelmann, U. Gonser, B. Dischler, and A. Räuber, "Photorefractive centers in $LiNbO_3$, studied by optical-, Mössbauer- and EPR-methods," *Appl. Phys. A*, vol. 12, pp. 355-368, Apr. 1977.

[22] F. Jermann and J. Otten, "Light-induced charge transport in $LiNbO_3$:Fe at high light intensities," *J. Opt. Soc. Am. B*, vol. 10, pp. 1085-2092, Nov. 1993.

[23] O. Momtahan, A. Karbaschi, and A. Adibi, "Gated holography: materials, techniques, and applications," *Proc. SPIE*, vol. 4988, pp. 24-39, June. 2003.

[24] D. von der Linde, A. M. Glass, and K. F. Rodgers, "Multiphoton photorefractive process for optical storage in $LiNbO_3$," *Appl. Phys. Lett.*, vol. 25, pp. 155-157, Aug. 1974.

[25] K. Buse, F. Jermann, and E. Kratzig, "Two-step photorefractive hologram recording in $LiNbO_3$:Fe," *Ferroelec.*, vol. 141 pp. 197-205, Apr. 1993.

[26] H. Guenther, R. M. Macfarlane, Y. Furukawa, K. Kitamura, and R. R. Neurgaonkar, "Two-color holography in reduced near-stoichiometric lithium niobate," *Appl. Opt.*, vol. 37, pp. 7611-7623, Nov. 1998.

[27] K. Buse, A. Adibi, and D. Psaltis, "Non-volatile holographic recording in doubly doped lithium niobate crystals," *Nature*, vol. 393, pp. 665-668, June 1998.

[28] A. Adibi, K. Buse, and D. Psaltis, "Effect of annealing in two-center holographic recording," *Appl. Phys. Lett.*, vol. 74, pp. 3767-3769, June 1999.

[29] A. Adibi, K. Buse, and D. Psaltis, "Two-center holographic recording," *J. Opt. Soc. Am. B*, vol. 18, pp. 584-601, May 2001.

[30] O. Momtahan and A. Adibi, "Global optimization of sensitivity and dynamic range for two-center holographic recording," *J. Opt. Soc. Am. B*, vol. 20, pp. 449-461, March 2003.

[31] O. Momtahan, G. H. Cadena, and A. Adibi, "Sensitivity variation in two-center holographic recording," *Opt. Lett.*, vol. 30, pp. 2709-2711, Oct. 2005.

[32] Y. W. Liu, L. R. Liu, C. H. Zhou, and L. Y. Xu, "Nonvolatile photorefractive holograms in $LiNbO_3$:Cu:Ce crystals," *Opt. Lett.*, vol. 25, pp. 908-910, June 2000.

[33] I. G. Kim, M. Lee, S. Takekawa, Y. Furukawa, K. Kitamura, L. Galambos, and L. Hesselink, "Volume holographic storage in near-stoichiometric $LiNbO_3$:Ce:Mn," *Jpn. J. Appl. Phys.*, vol. 39, pp. L1094-L1096, Nov. 2000.

[34] C. Moser, B. Schupp, and D. Psaltis, "Localized holographic recording in doubly doped lithium niobate," *Opt. Lett.*, vol. 25, pp. 162-164, Feb. 2000.

[35] C. Moser, I. Maravic, B. Schupp, A. Adibi, and D. Psaltis, "Diffraction efficiency of localized holograms in doubly doped $LiNbO_3$ crystals," *Opt. Lett.*, vol. 25, pp. 1243-1245, Sep. 2000.

[36] A. Karbaschi, O. Momtahan, A. Adibi, and B. Javidi, "Optical correlation using gated localized holography," *Opt. Eng.*, vol. 44, pp. 085802(1-8), Aug. 2005.

[37] G. W. Burr, F. H. Mok, and D. Psaltis, "Angle and space multiplexed holographic storage using the 90° geometry," *Opt. Comm.*, vol. 117, pp. 49-55, May 1995.

[38] C. Gu, H. Fu, and J. R. Lien, "Correlation patterns and cross-talk noise in volume holographic optical correlators," *J. Opt. Soc. Am. A*, vol. 12, pp. 861-868, May 1995.

[39] C. Gu, J. Hong, and S. Campbell, “2-D shift-invariant volume holographic correlator,” *Opt. Comm.*, vol. 88, pp. 309-314, Apr. 1992.

[40] M. Levene, G. J. Steckman, and D. Psaltis, “Method for controlling the shift invariance of optical correlators,” *Appl. Opt.*, vol. 38, pp. 394-398, Jan. 1999.

[41] F. H. Mok, G. W. Burr, and D. Psaltis, “System metric for holographic memory systems,” *Opt. Lett.*, vol. 21, pp. 896-898, June 1996.

[42] K. Buse and E. Krätzig, “Inorganic photorefractive materials,” in *Holographic Data Storage*, H. J. Coufal, D. Psaltis, and G. T. Sincerbox, Eds., Berlin: Springer-Verlag, 2000, pp. 113-125.

[43] G. W. Burr, “Volume holographic storage using the 90° geometry,” Ph.D. dissertation, California Institute of Technology, CA, USA, 1996.

[44] A. Karbaschi, O. Momtahan, and A. Adibi, “Dynamic optical correlation using localized holography,” *Opt. Lett.*, vol. 32, pp. 597-599, March 2007.

[45] A. Adibi, K. Buse, and D. Psaltis, "Sensitivity improvement in two-center holographic recording," *Opt. Lett.*, vol. 25, pp. 539-541, Apr. 2000.

[46] A. Adibi, K. Buse, and D. Psaltis, "Multiplexing holograms in $LiNbO_3$:Fe:Mn crystals," *Opt. Lett.*, vol. 24, pp. 652-654, May 1999.

[47] Z. Liu, “Optical information storage and processing,” Ph.D. dissertation, California Institute of Technology, CA, USA, 2001.

[48] C. Moser and D. Psaltis, “Holographic memory with localized recording,” *Appl. Opt.*, vol. 40, pp. 3909-3914, Aug. 2001.

[49] A. Karbaschi and A. Adibi, "Enhancement of shift invariance and rotation invariance in localized holographic correlators," *Opt. Lett.*, in preparation.

[50] J. Rosen, “Three-dimensional optical Fourier transform and correlation,” *Opt. Lett.*, vol. 22, pp. 964-966, July 1997.

[51] B. Javidi and E. Tajahuerce, “Three-dimensional object recognition by use of digital holography,” *Opt. Lett.*, vol. 25, pp. 610-612, May 2000.

[52] S. G. Srinivasa, O. Momtahan, A. Karbaschi, S. W. McLaughlin, F. Fekri, and A. Adibi, “Volumetric storage limits and space-volume multiplexing trade-offs for holographic channels,” *J. Opt. Soc. Am. B.*, to be published.

[53] P. S. Considine, “Effects of coherence on imaging systems,” *J. Opt. Soc. Am.*, vol. 56, pp. 1001-1009, Aug. 1966.

[54] G. W. Burr and T. Weiss, “Compensation for pixel misregistration in volume holographic data storage,” *Opt. Lett.*, vol. 26, pp. 542-544, Apr. 2001.

[55] M. Keskinoz and B. V. K. Vijaya Kumar, “Application of linear minimum mean-squared-error equalization for volume holographic data storage,” *Appl. Opt.*, vol. 38, pp. 4387-4393, July 1999.

[56] Document No. 409/0353/01A, XGA4 miniature LCD user guide, CRLO Displays, Ltd. (Now Forth Dimension Displays, Ltd.), Dunfermline, Scotland, 2004.

[57] L. Hesselink, S. S. Orlov, and M. C. Bashaw, “Holographic data storage systems,” *Proc. IEEE*, vol. 92, pp. 1231-1280, Aug. 2004.

[58] C. Gu, J. Hong, I. McMichael, R. Saxena, and F. Mok, “Cross-talk-limited storage capacity of volume holographic memory,” *J. Opt. Soc. Am. A*, vol. 9, pp. 1978-1983, Nov. 1992.

[59] J. W. Goodman, *Introduction to Fourier Optics*. New York: McGraw-Hill, 1996.

[60] G. W. Burr, H. Coufal, R. K. Grygier, J. A. Hoffnagle, and C. M. Jefferson, “Noise reduction of page-oriented data storage by inverse filtering during recording,” *Opt. Lett.*, vol. 23, pp. 289-291, Feb. 1998.

[61] J. F. Heanue, M. C. Bashaw, and L. Hesselink, “Channel codes for digital holographic data storage,” *J. Opt. Soc. Am. A*, vol. 12, pp. 2432–2439, Nov. 1995.

[62] F. Mok, G. Zhou, and D. Psaltis, “Holographic read-only memory,” in *Holographic Data Storage*, H. J. Coufal, D. Psaltis, and G. T. Sincerbox, Eds., Berlin: Springer-Verlag, 2000, pp. 400-407.

[63] Document No. TI DN 2503686, 0.7 XGA 12º DDR DMD Discovery™ product preview data sheet, Texas Instruments, Dallas, TX, 2005.

[64] B. M. King and M. A. Neifeld, “Parallel detection algorithm for page-oriented optical memories,” *Appl. Opt.*, vol. 37, pp. 6275–6298, Sep. 1998.

VITA

Arash Karbaschi was a member of the National Physics Olympiad team of Iran in 1992. He received his BSc in 1996 and MSc in 1998 in Electrical Engineering from Sharif University of Technology, Tehran, Iran. He is a PhD candidate in Electrical Engineering at Georgia Institute of Technology, expecting to graduate in spring 2008. He has performed extensive research in holography both in theoretical and experimental aspects. He has been involved in optical information processing, data storage, and spectroscopy using volume holography. He has strong industrial background including research and development management, quality assurance management, and quality management system project directorship in power electronics and plastics industry.